Study on Observation of Molecularly Thin Lubricant by Vertical-Objective-Based Ellipsometric Microscopy

Qingqing LIU

2012

CONTENTS

CHAPTER 5 IMPROVEMENT OF THICKNESS RESOLUTION 88

LIST OF FIGURES

LIST OF TABLES

ACKNOWLEDGEMENT

I would like to express my gratitude to all those who helped me during the writing of this thesis.

My deepest gratitude goes first and foremost to Prof. Kenji Fukuzawa, my supervisor, for his constant encouragement and guidance during this study, and whose intellectual insights have contributed greatly to the completion of this thesis. He has walked me through all the stages of the writing of this thesis. Without his consistent and illuminating instruction, this thesis could not have reached its present form.

I am deeply grateful to Prof. Hiroshi Tani and Prof. Tomohide Niimi for their careful reading and helpful comments for my Ph.D thesis. I am also indebted to Lectuer Shintaro Itoh not only for his invaluable suggestions on this thesis but also for his help during the whole study.

I would like to offer my thanks to Prof. Hedong Zhang for her kindness and valuable advices in the past years.

I also owe my sincere gratitude to all the members in Fukuzawa’s Lab who gave me their enthusiastic support and help during these years.

I want to say thanks to all my friends who brought me joy in my life, help and encouragement of my study.

At last, my thanks would go to my family for their loving considerations and great confidence in me.

Chapter 1　Introduction

1.1 Background

1.1.1 Hard Disk Drives

The introduction of the concept of storage can be traced back to primitive times. People in the past recorded informations on top of the walls and plants, as the murals, grass knot and so on. With the development of the information technology, especially introduction of a large number of computers, an age of information explosion is coming. Data storage requires greater capacity, faster speed, and higher stability. Hard disk drive (HDD) as the primary storage device statisfies these demand. In 1956, the first HDD which is called RAMAC（Random Access Method of Accounting and Control） with a density of 2000 bit / inch^2 was developed (1). In the 1990s, areal recording density began to improve rapidly. The two technologies have played important roles here: (1) Magnetoresistive (MR) head and (2) Partial-Response Maximum-Likelihood (PRML) technologies. Due to these technologies, areal recording density of HDD rapidly rised at an annual growth rate of 60%(2), which means that every five years can be increased by 10 times. In fact, areal density was only 100 Mb / inch^2 in 1991, and had increased to 1Gb / inch^2 in 1996. Moreover, on May 4, 2011, Seagate announced the world's first 1 TB HDD per platter, which means 5 TB, 10 TB or even greater capacity HDD will be widely used for personal use in the near future.

Figure 1.1 shows the composition of an HDD. An HDD is a sealed, and inside there are magnetic disk, head and other motion mechanisms. The substrate of a magnetic disk is made of glass or aluminum alloy, which has a thickness of about 0.635 ~ 1.7 mm due to the diameter of the disk, and diameter of 1.8 inch, 2.5 inch or 3.5 inch. Magnetic disks are mounted on the shaft of the spindle motor, and rotate at a high speed, 4500 ~ 15000 rpm. A magnetic head on a slider, suspension and voice coil motor are serially connected. The suspension is controlled by a voice coil motor, so that the magnetic head can be precisely positioned in a very short time. The slider is flying above the disk during the operation due to the high speed rotation of disk, and the flying hight is decreased to 2~3 nm in current HDDs. Here, we use the head to media spacing to define the flying height as shown in Fig. 1.2. As the slider flies at high speed and low flying hight, in order to protect the magnetic disk from abrasion, the HDD must be well sealed to prevent dust, as well as solid and liquid lubricant films are required on the disk surface (3, 4).

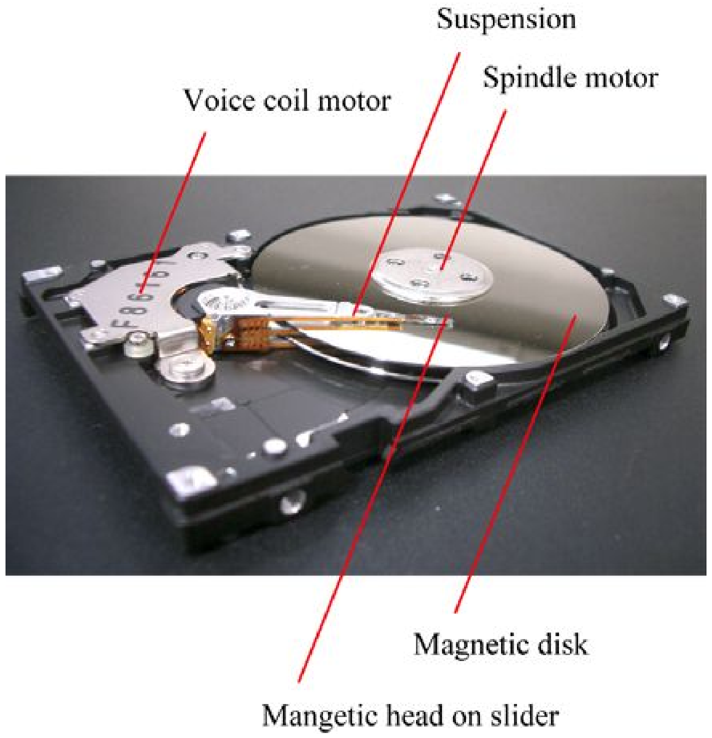

Fig. 1.1 Structure of hard disk drive.

1.1.2 Lubrication on Head Disk Interface

The typical composition of head disk interface (HDI) of an HDD is shown in Fig 1.2. In a magnetic disk, there are underlayer and magnetic layer on the glass substrate, and diamond like carbon (DLC) layer is on the magnetic layer as a protective film. On the top, liquid lubricant is applied to form molecularly thin flim. Digital data which is recorded on a magnetic disk are stored in the bit cells which are arranged in the magnetic layer. Each bit cell acts as a very small magnet and records a signal of 1 or 0, which corresponds to the direction of their magnetization. A slider flying over the magnetic disk that rotated at high speed, maintaining the magnetic spacing of nanometer order. In addition, the slider surface is coated with a DLC film to protect the magnetic head when it contacts the disk, and also prevent it from corrosion.

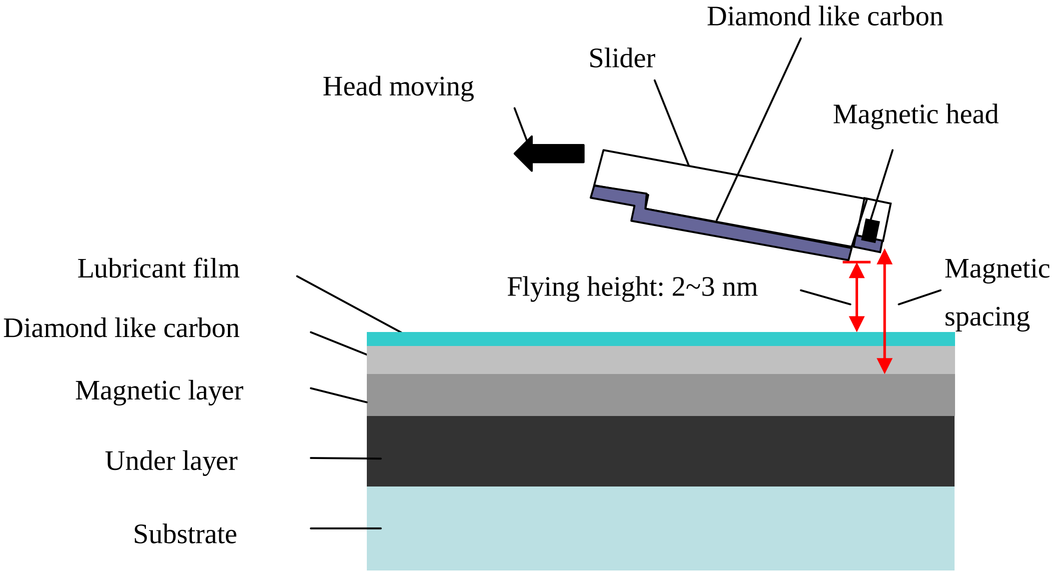

Fig. 1.2 Head disk interface of the hard disk drive.

In order to increase recording density of HDDs, deceasing size of bit cells is indispensable. So it is necessary not only to reduce the dimension of the magnetic head, but also to decrease the flying height of magnetic head in order to suppress the spreading of the magnetic leakage from the magnetic head. The relationship between the head to media spacing and areal density in products is shown in Fig 1.3 (5). It indicates that the head to media spacing should be decreased to about 1.5 nm to obtain the recording density of 1Tb / inch^2. In order to ensure the reliability and durability of the head and the media for this small gap, liquid lubricant films have been applied on the surface of the magnetic disk. Corresponding to the miniaturization of the gap between the head and disk, the thickness of the liquid lubricant films is required to be 1-2 nm, which is molecularly thin. The perfluoropolyether (PFPE) lubricants are commonly used as the liquid lubricants for HDI. Good viscosity, low surface tension, low volatility and good thermal stability are the important criteria for selection of the lubricants (6). PFPE lubricants with a polar group at the end of main chain are called the polar lubricants. The polar lubricant molecules bond to the disk surface chemically due to the effect of polar end groups. Here, the chemical bonding is hydrogen bondding. As shown in Fig 1.4, the molecules that strongly bond to the disk are called bonded molecules. However this chemical bond does not happen to all the molecules. Some of the molecules can not bond to the disk chemically, and are easy to flow, which are called mobile molecules. The bonded molecules form the bonded layer on the substrate to protect DLC from wearing and protect the magnetic disk. On the other hand, the mobile molecules can not only decrease the friction coefficient but also replenish the surface sites where the lubricant film is depleted (7-9).

Currently, with the increasing recording density of the HDDs, the flying height of magnetic head are continuously decreasing to less than 10 nm, as well as the thickness of liquid lubricant films requires to be 1-2 nm. Therefore, the control of the distribution of the liquid film is crucial to improve the recording density. For example, a lubricant meniscus may be formed between the head and disk at a near-contact region. Dewetting occurs when the lubricant thickness exceeds the critical one. In addition, the lubricant depletion due to the head contact becomes more severe in heat-assisted magnetic recording because heating makes surface tension change. The temporal scale of these phenomena is estimated at less than 1 s because the size is μm scale. Therefore, demands for the real-time observation are increasing. Moreover, the lateral resolution and thickness resolution is required sub-μm and sub-nm, respectively, due to the property of the lubricant film as mentioned above.

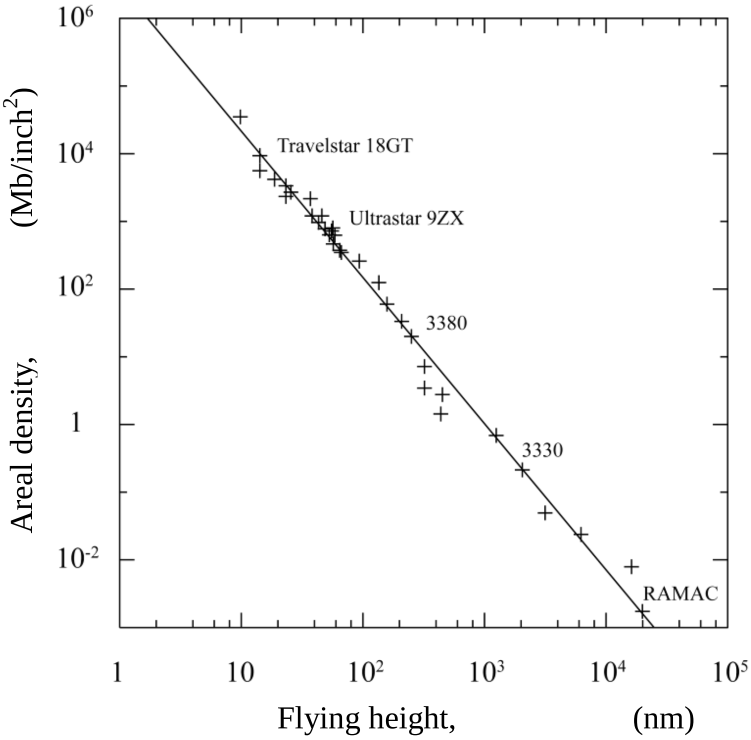

Fig. 1.3 Flying height vs. product areal density⁽⁵⁾.

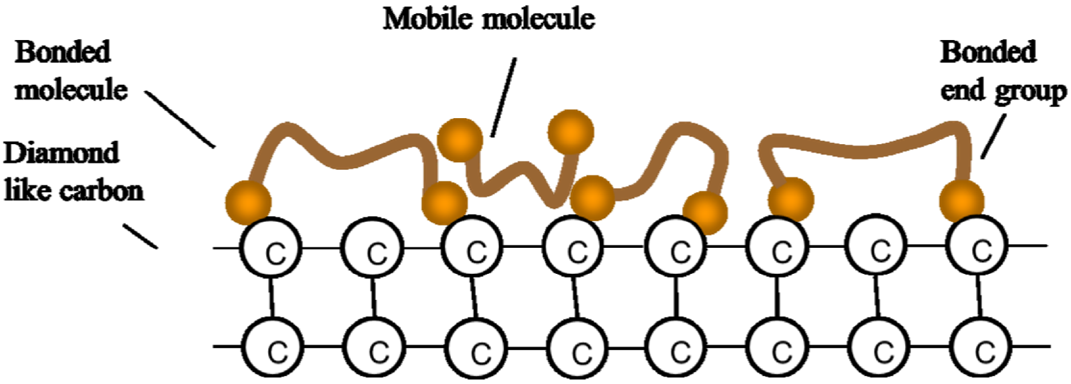

Fig. 1.4 PFPE lubricant molecules on the DLC overcoat.

1.2 Methods for Molecularly Thin Lubricant Observation

Lubricant films on the magnetic disks are molecularly thin, transparent and fluidic. Several different techniques have been used in the past to investigate phenomena on the surface of magnetic disks. Real-time visualization of nm-thick liquid lubricant-films by ellipsometric microscopy (EM) plays an important role in the analysis of lubrication for the HDDs. In order to achieve a high recording density in HDDs for the next generation it is essential to realize the contact recording. In the contact recording, the magnetic head flies on the magnetic disk, while always shows a contact state to a liquid lubricant film applied on the surface of the magnetic disk, which has the thickness of 1 ~ 2 nm. In order to ensure stable running of the magnetic head and the durability of the magnetic disk, the control of the distribution of the liquid film is important. The most popular mechanical method is atomic force microscope (AFM), and the optical method includes X-ray photoelectron spectroscopy (XPS), fourier transform infrared spectroscopy (FTIR), optical surface analyzer (OSA), ellipsometry, and so on. In secondary ion mass spectroscopy (SIMS), electron beam is used. In this part, there is a brief description for these methods of the observation and analysis of molecularly thin films.

1.2.1 Atomic Force Microscope (AFM)

The AFM was developed by Binnig in 1986 (10), which is a technology of detecting the interaction forces between the atoms or molecules to observe the surface morphology. It consists of a cantilever with a sharp tip at the end. When the tip is brought into proximity of a sample surface, and the small forces between the tip and the sample surface lead to a deflection of the cantilever according to Hooke's law. The deflection is detected by a four-quadrant photodiode. Light from a laser diode travels through the optical system and focuses on the back of the cantilever, and the reflection of the cantilever is detected as a light spot by the photodiode. When scanning, the cantilever deflects ups and downs with the sample surface topography, and the laser spot moves according to the cantilever deflection. The difference of the output signals collected by the each quadrant of the photodiode changes and the height of the sample surface can be obtained from the change of the difference signal. It has a high lateral resolution of about 0.1 nm and thickness resolution of 0.01 nm. However, since AFM measures point by point, the probe must be scanned in two directions when measuring a sample surface. It takes long time for scanning; therefore, the dynamic or real-time visualization of the thin film is difficult.

1.2.2 X-ray Photoelectron Spectroscopy (XPS)

In XPS, sample surface is radiated by X-ray so that stimulated emission of the inner electrons or valence electrons of atoms or molecules occurs. The stimulated electron is called photoelectron. By measuring the kinetic energy of photoelectrons emitted from the sample, the binding energy of the electrons can be obtained, which gives the sample information, such as composed chemical elements and structure. This method can also measure the thickness of the lubricant films by comparing the signal intensities of the photoelectrons from the lubricant and from the substrate due to the difference in electron density of the sample surfaces (11). The XPS method can provide a high thickness resolution of about 0.01 nm, however, the lateral resolution is low (tens of microns). This method must scan X-ray beam to get the thickness distribution as AFM. Therefore, it is not suitable for visualization of thin film. And another drawback is that the observed lubricant films can be degraded by the high power X-ray exposure (12).

1.2.3 Time-of-flight Secondary Ion Mass Spectroscopy (ToF-SIMS)

In secondary ion mass spectroscopy (SIMS), an ion beam with energy of 1-30keV is used to bombard the sample surface, and the sputtering of secondary ions are collected. In ToF-SIMS, the secondary ions are generated by the pulsed primary ion beam, where the sample is bombarded only for a very short time (13). In the time between two successive pulses, the generated secondary ions are post-accelerated and separated by their mass in a flight tube. Different ion species arrive at different times at the detector and the most ion species can be detected. And the thickness of lubricant films can be obtained by measuring the intensity of the secondary ions (14,15). This method has been used in the last three decades mainly in the applications of surface characterization of magnetic storages and solid lubricants (15-18), because of high sensitivity, a wide mass range, high mass resolution and high lateral resolution (13). However, it requires scanning mechanisms and moreover, it is a method that can destroy the sample surface. Thus this method is not suitable for the fluid liquid films.

1.2.4 Fourier Transform Infrared Spectroscopy (FTIR)

FTIR is a well-established, non-destructive method for determining the chemical composition of materials by resolving their chemical bonding. Because it resolves chemical bonds more clearly than techniques such as XPS, it is particularly useful for polymers, which tend to have many variation modes of chemical bondings. In addition, FTIR methods are effective non-contact and faster methods for measuring the thickness of thin films. Generally, Michelson interferometer is used in an FTIR spectrometer for generating the coherent light (19), and when light incident on the sample surface, a large portion of the light reflects from the surface and forms the primary reflection. The remaining radiation penetrates the film and reflects from the interface of the film and substrate, giving rise to the secondary reflection or secondary interferogram. And raw data from an FTIR spectrometer is sometimes called interferogram. It describes the retardation and path difference between the two reflections. These relate to the thickness of the film. The main benefit of the FTIR technique is the speed of the measurement. Other benefits are that the FTIR thickness measurement is non-destructive and reproducible as mentioned above, and the thickness resolution of a conventional one can be obtained about 0.1 nm, however the lateral resolution is several µm. And scanning is required in the system, so it is also difficult for this method to do the real-time visualization, and there is also a drawback that the spatial resolution is low (19).

1.2.5 Optical Surface Analyzer (OSA)

An OSA uses P- and S-polarized light to measure thickness changes in both lubricant and carbon layer of a magnetic disk (21). Polarized light interacting with the disk surface results in combination of absorption, reflection, and scattering. The amount of reflected and scattered light is measured by two photodetectors: P / S scattered (with an integrating sphere) and P / S specular. OSA uses S- and P-polarized light reflectivities will vary in different ways as a function of thickness of lubricant film and the substrate. The thickness of the lubricant becoming thinner, which increases the intensity of reflected S-polarized light, but decreases the intensity of reflected P-polarized light. The opposite is true for an increase of lubricant thickness. Both, S- and P-reflected light intensities increase in the case of DLC thinning. Wear particle or surface roughness increase leads to a decrease of S- and P-polarized light specular components due to increased light scattering. Magnetic disk is rotated at a high rate of speed and the optical head with the incident light beam moved over the surface in a spiral manner. This is a nondestructive surface-analysis technique that can provide 2-D image of thin films in high thickness resolution (22), however, the lateral resolution of the OSA is several microns (5 by 10 µm for orthogonal directions)(21). And rotation mechanisms are needed for scanning. Therefore, it is difficult to obtain the real-time observation of thin lubricant films due to the limitation of the rotation speed.

1.2.6 Ellipsometry

Ellipsometry was first developed more than 100 years ago, however, advances in electronics and computing were needed to make it applicable to a broad range of industries. In general, ellipsometry is based on the measurement of the elliptical states of polarized light reflected from or transmitted through a material surface. By studying interface-induced changes of the light, the amplitude change and the phase shift due to the reflection or transmission of the light,one can measure fundamental optical properties of the sample, including the refractive index, absorption coefficient, surface roughness, alloy concentrations, and thickness. Single-wavelength ellipsometry can measure only two parameters, while spectroscopic ellipsometry can analyze complex structures such as multilayers, interface roughness, inhomogeneous layers, and anisotropic layers. In the last two decades, imaging processing devices were introduced into the ellipsometry. The developed imaging ellipsometry is called ellipsometric microscopy (EM) (24-26), which can provide thickness distribution as a dark-bright contrast image by using an imaging device instead of a photodetector. So the image of the sample in a large field can be obtained, and the scanning mechanism is not required. In addition to its nondestructive nature, the advantages of EM are its high sensitivity (due to the measurement of the phase of the reflected light), large measurement range (from fractions of single layers to micrometers), and the ability to control real-time complex processes. Therefore, EM is a good candidate for real-time visualization.

1.3 Research Objective

Most of the methods for lubricant film measurement mentioned above require scanning mechanisms except EM. Therefore they do not apply to the dynamic observation of the lubricant films in HDI. Although conventional EMs can avoid these problems, they have a drawback of low lateral resolution of several μm. To meet this demand, vertical-objective-based EMs (VEMs) were recently proposed and the feasibility was demonstrated (27, 28). However, the method has not been established.

In this study, we firstly established the designs for the optical system and image detection of the vertical-objective-based EM to provide sub-μm lateral resolution with large field of view, and then investigated the imaging characteristic that is important for evaluation of lateral resolution and developed a thickness calibration where the ellipsometric light intensity signal is converted to the thickness. First, the light intensity signal is experted to convert to thickness directly which is required by real-time observation. Then a special method called phase shift method is developed for calibration, which means the VEM can determine the film thickness by itself. And for a further study, since the thickness of the film in HDI is 1-2 nm, the thickness resolution should be 0.1- 0.2 nm, the methods of improvement of thickness resolution are discussed. The methods for improvement of signal and suppression of noise are considered by analyzing the design principle of the VEM, such as the choises of the light source and incident angle, etc.

1.4 Other Applications

In this study, I concentrate on the observation of lubricant films on magnetic disks by VEM. Actually, it can also be used in biology or materials science fields. For example, molecular hybridization of DNA attracks many researchers in biology. Traditional molecular hybridization is generally in the membrane. The sample is fixed in the membrane with a fluorescent, biotin, or isotope-labeled probe. And then a probe of known sequence by hybridization reaction is used to detect the sequence information of the sample. Due to the attenuation of label signal over time, long time of the measurement is difficult. On the other hand, it is not required to make a label to the sample in EM-based detection. The thickness of the film of DNA will increase due to the molecular hybridization; therefore, EM can be used to measure the thickness difference to detect the molecular hybridization of DNA. In addition, EM can do real-time observation, and the measurement time is unrestricted. Moreover, this method does not destroy (or interfere with) the target to be measured system during the measurement process. Therefore, EM is expected to be a good candidate for the study on molecular hybridization of DNA.

1.5 Organization of This Dissertation

The remainder of this thesis consists of seven chapters.

In Chapter 2, the principle of VEM was explained. Considering that the VEM is based on ellipsometry, 2 × 2 matrix method, which is used for thickness determination in Chapter 4 was explained. Then the drawback of EM was explained.

In Chapter 3, the materials for this research were described, which included the information of magnetic disks and lubricants and the method for lubricant application.

In Chapter 4, setup of VEM was presented and the method to obtain the thickness of the thin films by measuring the phase shift was explained.

In Chapter 5, a method for improving the thickness resolution of VEM was developed. Effects of light intensity, incident angle and pinhole size on signal-to-noise ratio, which determined the thickness resolution was investigated. And the thickness resolution was improved up to 0.2 nm.

In Chapter 6, the developed VEM was applied to observations of dewetting process of nm-thick lubricant films on magnetic disks. The observation clarified that the films with different thicknesses dewet in different ways.

In Chapter 7, a new VEM called backside illuminated VEM was discussed for the study in future, the design of backside illuminated VEM was conceived and the feasibility of the method was discussed.

Finally, I concluded this thesis in Chapter 8.

Chapter 2 Principle of Vertical-Objective-Based Ellipsometric Microscope (VEM)

2.1 Ellipsometry

Ellipsometry is a method for obtaining the complex refractive index and the thickness of the sample by irradiating on the sample surface.The oblique light with known polarization state illuminating to a sample and analyzing the change in polarization state due to the reflection, the thickness of the sample can be obtained. It is possible for ellipsometry to measure with a high sensitivity thickness resolution of the order of 0.1 nm. In addition, the configuration is simple, so it has been widely used to measure the properties of thin films, recently. The principle of the ellipsometry will be explained in this chapter.

2.1.1 Polarization of Light and Reflection

Light is an electromagnetic wave. Electric vector ***E*** is generally used to describe the intensity and direction of the light, because the interaction of the electric field is stronger than that of the magnetic field. The ***E*** vector is always orthogonal to the direction of light propagation. As shown in Fig. 2.1, when a monochromatic light is incident onto a surface obliquely, the ***E*** vector can be described by two orthogonal vibration components E_p and E_s, which are parallel and perpendicular to the plane determined by incident and reflected light, respectively. This plane is called the plane of incidence. These vibration components have the same frequency, but generally different amplitude and phase.

As a result, the ***E*** vector moves along an ellipse when we observe at a fixed point in space. The behavior of a vector field is called polarization, and the vibration components E_p and E_s are called p polarization and s polarization, respectively.

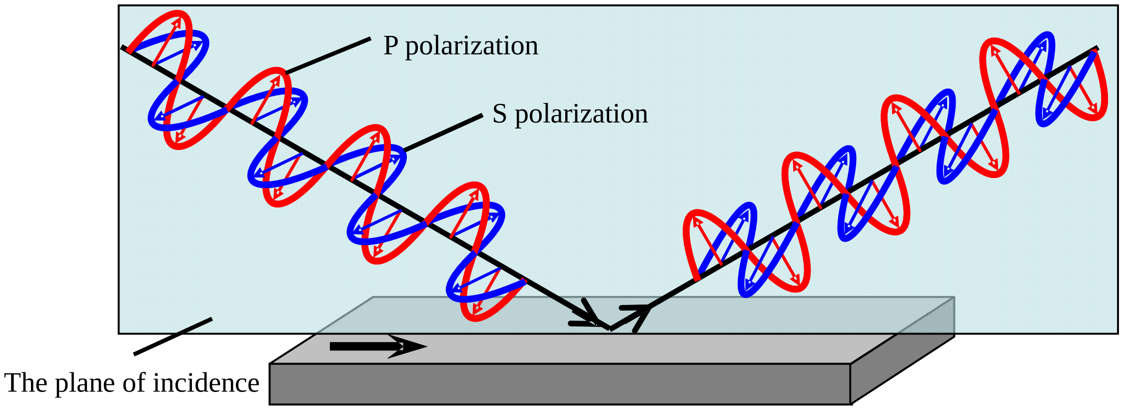

Fig. 2.1 Reflection of p polarization and s polarization light.

The propagation of plane waves in an absorbing medium is described by the complex index of refraction N, which is expressed as

$$N = n - ik \tag{2.1}$$

where n is the refractive index and k is called extinction coefficient of the medium$^{(20)}$.

The Fresnel equations on the amplitude and phase of reflected light can be deduced by considering the continuity condition of electromagnetic field of refracted and incident lights across the interface. Since the situations are different for the two orthogonal vibration components E_p and E_s, they should be discussed separately.

For p polarization, shown in Fig. 2.2 (a), since the tangential components of electric field vector ***E*** and magnetic field vector ***H*** are continuous across the interface, the equations below can be obtained:

$$E_{ip}\cos\theta_i - E_{rp}\cos\theta_r = E_{tp}\cos\theta_t\,; \tag{2.2}$$

$$H_{ip} + H_{rp} = H_{tp}\,. \tag{2.3}$$

Here, subscript ip, rp and tp express the incident, reflected and refracted light, respectively, as well as θ_i, θ_r, and θ_t are the angle of incidence, reflection and refraction, respectively. And

$$H = \frac{1}{v}E\,, \tag{2.4}$$

where v is the speed of light in the medium. In addition, the complex indices of refraction are N_0 and N_1 for the two mediums,

$$\frac{v_0}{v_1} = \frac{N_1}{N_0}\,. \tag{2.5}$$

Accoding to the law of reflection, $\theta_\mathrm{i} = \theta_\mathrm{r}$, these equations can be obtained:

$$r_p = \frac{E_{rp}}{E_{ip}} = \frac{N_1\cos\theta_i - N_0\cos\theta_t}{N_1\cos\theta_i + N_0\cos\theta_t}\,; \tag{2.6}$$

$$t_p = \frac{E_{tp}}{E_{ip}} = \frac{2N_0 \cos\theta_i}{N_1 \cos\theta_i + N_0 \cos\theta_t}, \tag{2.7}$$

which are the Fresnel complex-amplitude reflection (*r*) and transmission (*t*) coefficients for the p polarization.

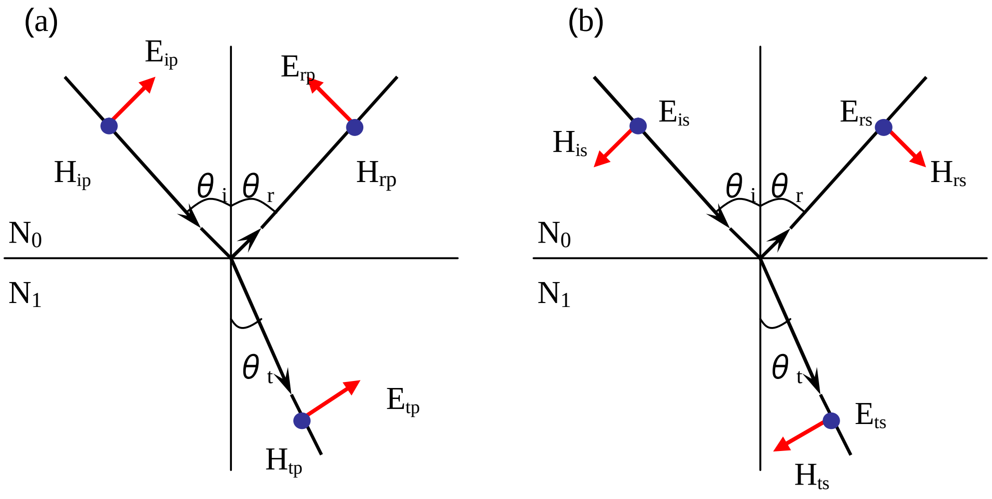

Fig. 2.2 (a) components E and H of P polarization; (b) components E and H of S polarization.

Similarly, for s polarization as shown in Fig. 2.2 (b), the continuity condition can be expressed as:

$$E_{is} + E_{rs} = E_{ts}, \tag{2.8}$$

$$H_{is} \cos\theta_i - H_{rs} \cos\theta_r = H_{ts} \cos\theta_t, \tag{2.9}$$

where is, rs and ts express the incident, reflected and refracted light for s polarization, respectively.

The Fresnel complex-amplitude reflection (r) and transmission (t) coefficients for the s polarization are expressed as

$$r_s = \frac{E_{rs}}{E_{is}} = \frac{N_0 \cos\theta_i - N_1 \cos\theta_t}{N_0 \cos\theta_i + N_1 \cos\theta_t} , \tag{2.10}$$

$$t_s = \frac{E_{ts}}{E_{is}} = \frac{2N_0 \cos\theta_i}{N_0 \cos\theta_i + N_1 \cos\theta_t} . \tag{2.11}$$

Eq. (2.6), (2.7), (2.10) and (2.11) are called Fresnel equations. Substituting the complex indices of refraction are N_0 and N_1 into Snell's law,

$$N_0 \sin\theta_i = N_1 \sin\theta_t . \tag{2.12}$$

Using $\sin^2\theta + \cos^2\theta = 1$, Eq. (2.12) can be transformed,

$$N_1 \cos\theta_t = \sqrt{N_1{}^2 - N_0{}^2 \sin^2\theta_i} . \tag{2.13}$$

So the angle θ_t can be eliminated from Fresnel equations, and

$$r_p = \frac{N_{10}{}^2 \cos\theta_i - \sqrt{N_{10}{}^2 - \sin^2\theta_i}}{N_{10}{}^2 \cos\theta_i + \sqrt{N_{10}{}^2 - \sin^2\theta_i}} , \tag{2.14}$$

$$r_s = \frac{\cos\theta_i - \sqrt{N_{10}{}^2 - \sin^2\theta_i}}{\cos\theta_i + \sqrt{N_{10}{}^2 - \sin^2\theta_i}} . \tag{2.15}$$

Here, $N_{10} = N_1 / N_0$, and the equations are based on choosing the direction of p and s so as to form right-handed Cartesian coordinate systems with the direction of propagation of the incident, reflected, and refractive waves.

In order to examine the effect of reflection and refraction on the amplitude and phase of the light wave separately, the Fresnel complex-amplitude reflection (r) and transmission (t) coefficients are rewritten as

$$r_p = |r_p| \exp(i\delta_{rp}) \tag{2.16}$$

$$r_s = |r_s| \exp(i\delta_{rs}) \tag{2.17}$$

$$t_p = |t_p| \exp(i\delta_{tp}) \tag{2.18}$$

$$t_s = |t_s| \exp(i\delta_{ts}) \tag{2.19}$$

$|r_\mathrm{p}|$ and $|t_\mathrm{p}|$ give the ratios of the amplitudes of the vibrations of the electric vectors of the reflected and refractive light waves, respectively. δ_rp and δ_tp give the phase shifts upon reflection and refraction, respectively. And they are with the similar meaning for $|r_\mathrm{s}|$, $|t_\mathrm{s}|$, δ_rs and δ_ts.

In ellipsometry, the measured quantity is the change of polarization due to reflection of light at the sample. The ratio ρ of the complex Fresnel reflection coefficients for p and s polarizations is usually used to describe this difference,

$$\rho = \frac{r_p}{r_s} = \tan\Psi \cdot e^{i\Delta} \tag{2.20}$$

$$\tan\Psi = \frac{|r_p|}{|r_s|} \tag{2.21}$$

$$\Delta = \delta_{rp} - \delta_{rs} \tag{2.22}$$

The ellipsometric angles ψ and Δ, are used to describe the change in polarization. In addition, the fraction of total intensity of an incident plane wave for p and s polarizations can be expressed by

$$\overline{R}_p = \frac{I_{rp}}{I_{ip}} = \left|\frac{E_{rp}}{E_{ip}}\right|^2 = |r_p|^2, \tag{2.23}$$

$$\overline{R}_s = \frac{I_{rs}}{I_{is}} = \left|\frac{E_{rs}}{E_{is}}\right|^2 = |r_s|^2. \tag{2.24}$$

Figure 2.3 shows the relationship between the incident angle θ_i and refletivity $\overline{R}_p$ and $\overline{R}_s$ for the air / glass interface, which have the indices of refraction of $N_0 = 1$ and $N_1 = 1.5$, respectively. The Brewster angle $\theta_B = 56.3$ deg is also shown in this figure, which is the incident angle where the reflected wave of p- polarized light disappears.

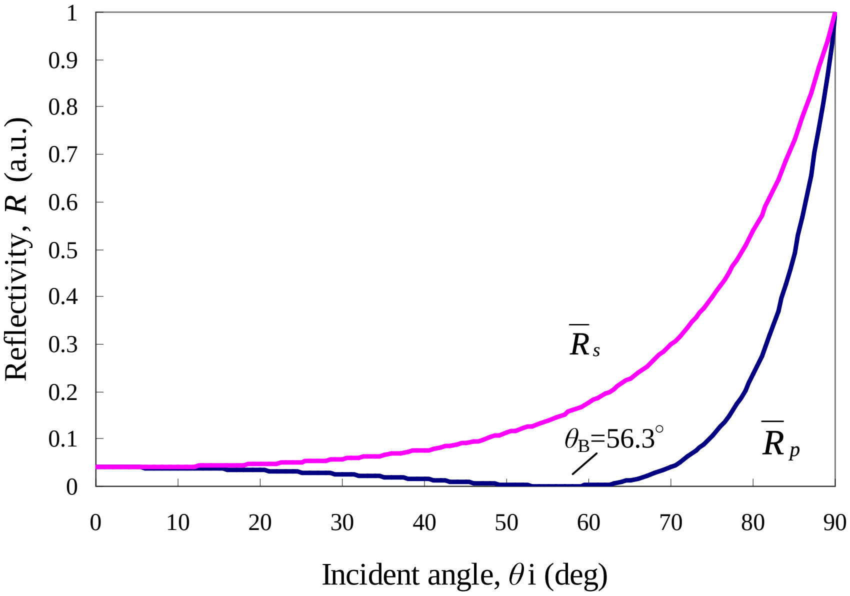

Fig. 2.3. Relationship between incident angle and reflectitivy for an air / glass interface.

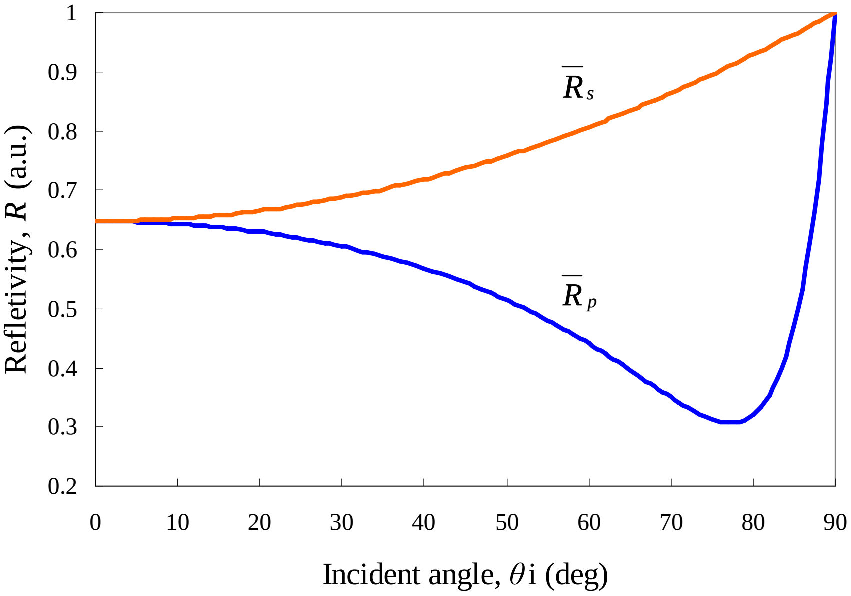

Fig. 2.4 Relationship between incident angle and reflectitivy for an air / magnetic disk interface.

In this study, I am interested in the air / magnetic disk interface. The typical value of the index of refraction for magnetic disk is 2.32 - 4.17i (29), and using this value, a simulation of the relationship between the incident angle and refletivity for p- and s- polarized light was done. The result shown in Fig. 2.4 indicates that the refletivity of s- polarized light is increasing with the incident angle increasing; on the other hand, that of p- polarized light reaches the minimum about 77 deg. At this angle, the difference of refletivities between the p- and s- polarized light intensity is significant, so the incident angle for ellipsometry is always set around this angle, typically 60 ~ 80 deg.

2.1.2 Analysis of Reflection and Transmission for a Multi-layer Structure by 2 × 2 Matrix Method

In ellipsometry, the polarized light is reflected at or transmitted (refracted) through the interface between different media. As shown in Fig. 2.5, a part of the plane wave incidence into the film is reflected at the air-film interface, and the other part is transmitted into the film and then separated to the light transmitted into the substrate and reflected at the film-substrate interface. When the light reflected from the film-substrate interface reaches the film-air interface, it is separated to reflection and transmission lights. The transmission light also contributes to the reflected wave that can be detected by the ellipsometry. As mentioned above, magnetic disk consists of multi-layer, such as lubricant film, DLC, magnetic layer, underlayer and glass substrate, therefore the multiple reflection must be considered.

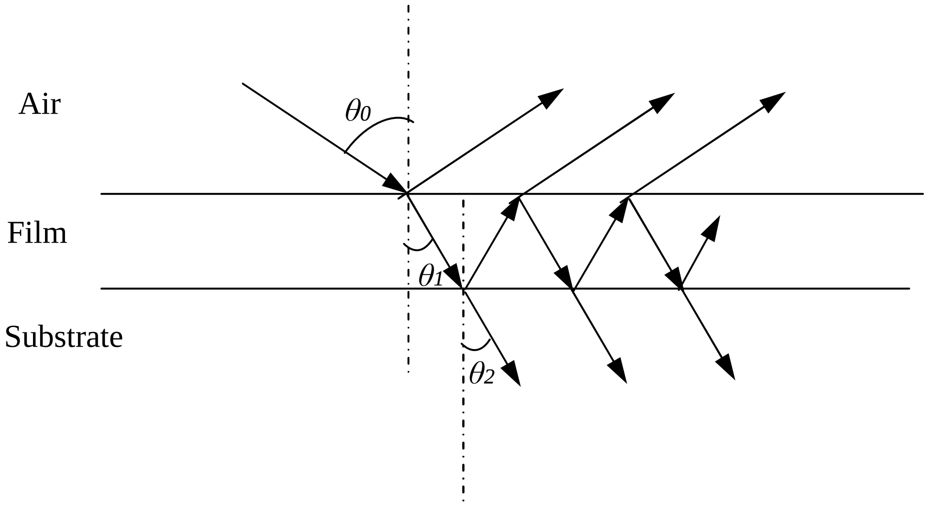

Fig. 2.5 Schematic of reflection and transmission at the interface of air / film / substrate.

2 × 2 matrix method (23) is widely used for analyzing reflection and transmission for multilayer structures. When light is incident on the multilayer structure, the change of the light can be decomposed into the reflection and transmission at the interface and propagation through the layer. Fig. 2.6 shows the layer model of a multilayer structure. θ_0 is the angle of incidence; θ_j and $\theta_{\mathrm{m+1}}$ are angles of refractive in the ***j***-th layer and substrate, respectively. The complex refractive index of the *j*-th layer is N_j, and its thickness is d_j. N_0 and $N_{\mathrm{m+1}}$ represent the complex refraction indices of the ambient and substrate, respectively. Using 2 × 2 matrices of ***I*** and ***L*** to describe the reflection / transmission and propagation, respectively, the scattering matrix ***S*** that determines the complex reflection coefficients can be expressed as follows:

$$S = \begin{bmatrix} S_{11} & S_{12} \\ S_{21} & S_{22} \end{bmatrix} = \boldsymbol{I}_{01}\boldsymbol{L}_1\boldsymbol{I}_{12}\boldsymbol{L}_2 \ldots \boldsymbol{I}_{(j-1)j}\boldsymbol{L}_j \ldots \boldsymbol{L}_m\boldsymbol{I}_{m(m+1)} . \tag{2.25}$$

For two-media interface (ab), the interface matrix $\boldsymbol{I}_{\mathrm{ab}}$ is given as follows:

$$I_{ab} = \begin{bmatrix} 1/t_{ab} & r_{ab}/t_{ab} \\ r_{ab}/t_{ab} & 1/t_{ab} \end{bmatrix}. \tag{2.26}$$

Where r_{ab} and t_{ab} are the Fresnel reflection and transmission coefficients of the ab interface, respectively. The layer matrix $\boldsymbol{L_j}$ can be written by

$$L_j = \begin{bmatrix} e^{j\beta_j} & 0 \\ 0 & e^{-j\beta_j} \end{bmatrix}, \tag{2.27}$$

where, β_j is the phase change that the multiply-reflected light propagation inside the film experiences. For simplicity, assuming that the light travels in the film from one boundary to the other, and β_j is given by

$$\beta_j = \frac{2\pi d_j N_j}{\lambda} \cos\theta_j, \tag{2.28}$$

where λ is the wavelength of the incidence, and θ_j and d_j are the angle of refraction and thickness of the certain layer, respectively.

For the purpose of ellipsometry, scattering matrix $\boldsymbol{S}$ for the stratified-structure has to be calculated for both polarizations parallel (p) and perpendicular (s) to plane of the incidence. Using $\boldsymbol{S}_{\mathrm{p}}$ and $\boldsymbol{S}_{\mathrm{s}}$ for p and s polarizations, and the p and s total amplitude reflectivities are obtained by

$$R_p = \frac{S_{21p}}{S_{11p}}, \tag{2.29}$$

$$R_s = \frac{S_{21s}}{S_{11s}}, \tag{2.30}$$

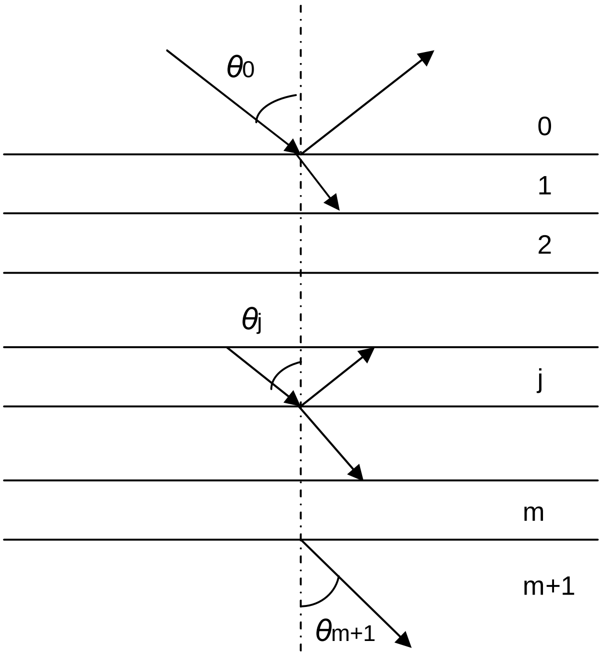

Fig. 2.6 Reflection and transmission in a multilayer structure.

2.1.3 Principle of Ellipsometry

The ellipsometry is an optical technique that can measure the optical properties, such as complex refractive index, or the thickness of thin films by using the change of the polarization state of the reflection. Polarized light is reflected at an oblique angle to a surface. And the change of the polarization is described by the ellipsometric angles ψ and Δ, which are defined by Eqs. (2.21) and (2.22). In order to measure the polarization state of reflected light, polarization devices: polarizer, analyzer and compensator, are necessary. The polarizer is used to obtain linearly polarized light when a non-polarized light is used as the light source. The analyzer can be used for determining the polarization state and compensator is used for the purpose of giving a phase difference between orthogonal polarization components mainly, which is also called wave plate (30). The ellipsometry can be classified according to the arrangement of the polarization devices as shown in Fig. 2.7. Since the null ellipsometer has a simple structure with high-precision (31), let us consider null ellipsometer for the introduction. The schematic setup of null ellipsometer is shown in Fig. 2.8. Non-polarized light passes through a polarizer (P) and a quarter wave plate (C) combination. Here, the angles of the polarizer and quarter wave plate are written as P and C, respectively. The non-polarized light becomes elliptically polarized after passing P and C. The elliptically polarized light is reflected off the sample, passes an analyzer (A). The angle of P and C is adjusted so that the reflected light from the sample is completely linearly polarized. A photo-detector behind the analyzer is used to detect the light intensity as the signal. The ellipsometric null condition is obtained when the angle of analyzer A is adjusted so that the transmission axis is perpendicular to the polarization axis of the reflected light. The angles of P, C, and A when the null condition is obtained are related to the optical properties of the sample. Analysis of the measured data by using optical modeling of the sample leads to the film thickness and complex refractive index of the sample.

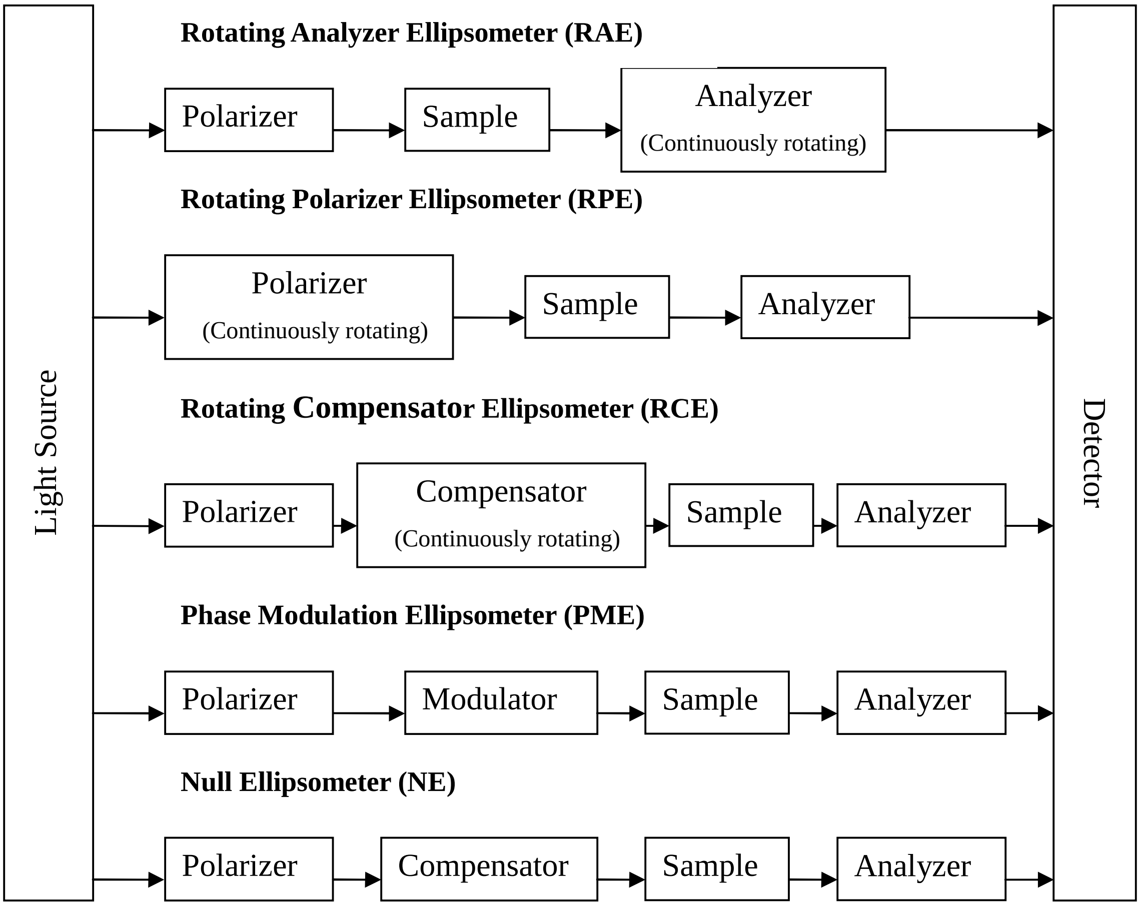

Fig. 2.7 Types of ellipsometry.

In old ellipsometers, the operator observed the light beam that was reflected off the sample through an eyepiece. The polarizers and compensators were rotated by hand until the effect of the polarization was inverted and no light would pass through the instrument. Modern null ellipsometers use a computer controlled mechanism for the rotation of the polarization elements and automatically calculate the ellipsometry signal very quickly.

2.2 Conventional Ellipsometric Microscope (EM)

2.2.1 Principle of Conventional EM

Ellipsometry can provide visualization of thickness distribution by using an imaging device like a CCD camera as a detector, which is called ellipsometric microscope (EM) or imaging ellipsometer. In this thesis, this method is called EM. It can provide a real-time measurement of the distribution of the film thickness and complex refractive index of the sample. This kind of ellipsometry has attracted the attention of many researchers from the 1990s (26, 32-34). An advanced EM operates by using the principle of classical null ellipsometer and real-time ellipsometric contrast is imaged with a single-wavelength ellipsometer setup with a laser as light source. The principle of the measurement is shown in Fig. 2.9. Here, the sample is a substrate partially covered with a thin-film. The polarization state depends on the thickness and refractive index of the sample surface. So, the uncovered region and film-covered region have different intensity of the reflected light. In the setup, thickness distribution is converted into dark-bright contrast with an analyzer.

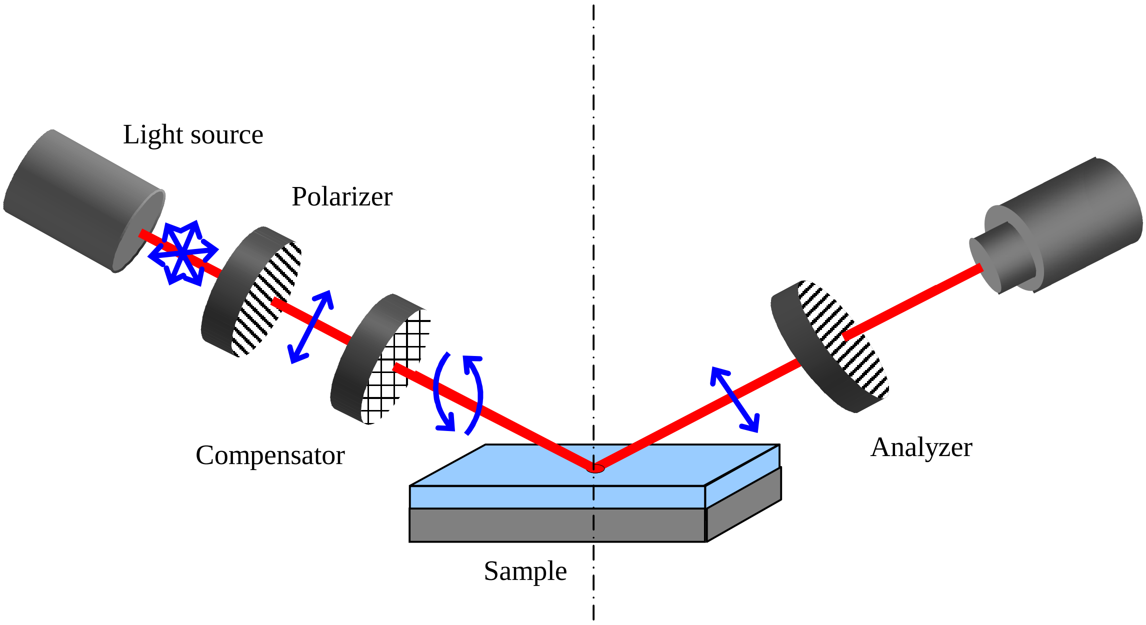

Fig. 2.8 Schematic setup of a null ellipsometer.

In order to represent the polarization state of light, the Jones matrix is widely used. In the Jones matrix, the electromagnetic wave is described by a Jones vector with two orthogonal complex-valued entries for the electric field, so p- and s- polarized light are defined as follows,

$$E = \begin{bmatrix} E_p \\ E_s \end{bmatrix}. \tag{2.31}$$

After light passes through the polarization devices, the polarization state changes. The effects of the polarization devices can be also expressed by the 2 × 2 Jones matrix. For example, when the angle between the p-axis and the fast axis of the quarter wave plate is 45 deg, the Jones matrix of quarter wave plate can be given by

$$J_Q = \frac{1}{\sqrt{2}} \begin{bmatrix} 1 & -i \\ -i & 1 \end{bmatrix}. \tag{2.32}$$

If the incident light is expressed by vector ***E***, the light passes through the quarter wave plate, ***E'*** can be given by

$$E' = J_Q E = \frac{1}{\sqrt{2}} \begin{bmatrix} 1 & -i \\ -i & 1 \end{bmatrix} E \tag{2.33}$$

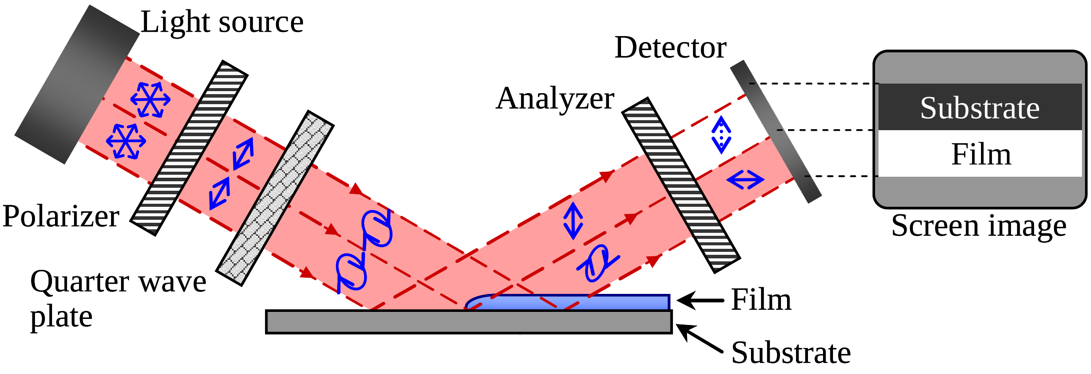

Fig. 2.9 Principle of ellipsometric microscope.

In EMs, using P, Q and A to express the angle between the p-axis and the axis of polarizer (polarizer angle), the angle between the p-axis and the fast axis of the quarter wave plate (quarter wave plate angle), and the angle between the p-axis and the axis of analyzer (analyzer angle), respectively. The model is shown in Fig. 2.10.

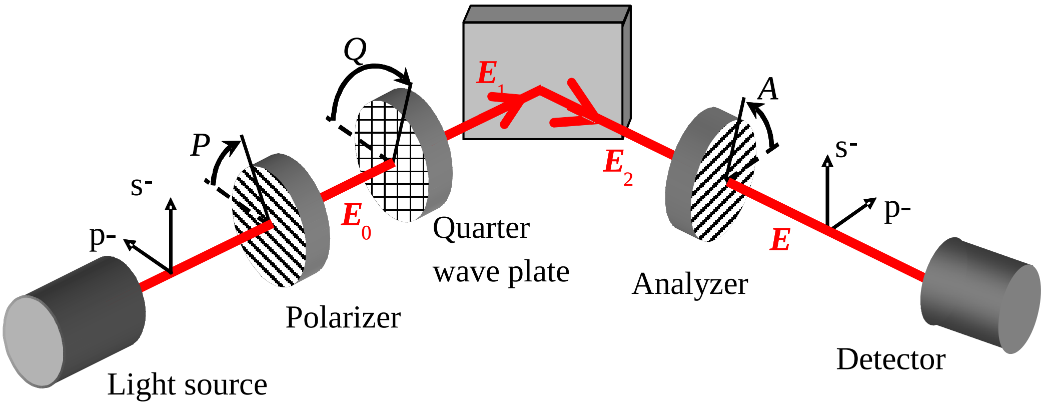

Fig. 2.10 Rotation angles of polarization devices.

First, non-polarized light passes through the polarizer to obtain the linearly polarized light. Its direction of vibration is parallel to the axis of polarizer, Jones matrix to express the linearly polarized light is

$$\mathbf{E}_0 = \begin{bmatrix} E_{0p} \\ E_{0s} \end{bmatrix} = \begin{bmatrix} E_0 \cos P \\ E_0 \sin P \end{bmatrix}. \tag{2.34}$$

The quarter wave plate is adjusted so that Q is 45 deg. Passing through the quarter wave plate, the light can be given by

$$\mathbf{E}_1 = \begin{bmatrix} E_{1p} \\ E_{1s} \end{bmatrix} = \frac{1}{\sqrt{2}} \begin{bmatrix} 1 & -i \\ -i & 1 \end{bmatrix} \mathbf{E}_0 . \tag{2.35}$$

Then, using R_p and R_s in Eqs. (2.29) and (2.30), the light reflected from the sample surface is given by

$$\mathbf{E}_2 = \begin{bmatrix} E_{2p} \\ E_{2s} \end{bmatrix} = \begin{bmatrix} R_p E_{1p} \\ R_s E_{1s} \end{bmatrix}. \tag{2.36}$$

The synthetic complex amplitude E of the light after the analyzer can be expressed by

$$E = E_{2p} \cos A + E_{2s} \sin A . \tag{2.37}$$

Using Eqs. (2.34) - (2.36), Eq. (2.37) can be rewritten by

$$
\begin{aligned}
E &= \frac{1}{\sqrt{2}} E_0 \left[R_p \cos A(\cos P - i \sin P) + R_s \sin A(\sin P - i \cos P)\right] \\
&= \frac{1}{\sqrt{2}} E_0 R_s \left[\rho \cos A(\cos P - i \sin P) + \sin A(\sin P - i \cos P)\right]
\end{aligned}
, \tag{2.38}
$$

where ρ is the ratio of the complex Fresnel reflection coefficients for p and s polarizations, can be expressed by

$$
\rho = \frac{|R_p|}{|R_s|} e^{i\Delta} = re^{i\Delta}, \tag{2.39}
$$

where r is the amplitude ratio for p- and s-polarized lights.

The detected light intensity I can be obtained,

$$
\begin{aligned}
I &= |E|^2 = \left| \frac{1}{\sqrt{2}} R_s E_0 \left[\rho \cos A(\cos P - i \sin P) + \sin A(\sin P - i \cos P)\right] \right|^2 \\
&= \frac{|R_s|^2 |E_0|^2}{2} \left| r \cos A \cos(P + \Delta) + \sin A \sin P - i\left[r \cos A \sin(P + \Delta) + \sin A \cos P\right] \right|^2 \\
&= \frac{|R_s|^2 |E_0|^2}{2} \left\{ \left[r \cos A \cos(P + \Delta) + \sin A \sin P\right]^2 + \left[r \cos A \sin(P + \Delta) + \sin A \cos P\right]^2 \right\} \\
&= \frac{|R_s|^2 |E_0|^2}{2} \left\{ r^2 \cos^2 A + 2r \sin A \cos A \sin(2P + \Delta) + \sin^2 A \right\}
\end{aligned}
, \tag{2.40}
$$

$I_0 = |E_0|^2$ is the intensity of incident light, so Eq. (2.40) can be rewritten as

$$
I = \frac{|R_s|^2 I_0}{2} \times \left\{ r^2 \cos^2 A + 2r \sin A \cos A \sin(2P + \Delta) + \sin^2 A \right\}. \tag{2.41}
$$

According to the Eq. (2.41), null condition can be obtained,

$$2P_d + \Delta_d = \frac{\pi}{2}, \tag{2.42}$$

$$r_d \cos A_d + \sin A_d = 0 . \tag{2.43}$$

Here subscript d is used to describe the condition for the region that uncovered with films (bared disk only). It means the null condition is usually set for the film-uncovered region in EMs, as shown in Fig. 2.9. In this study, I focus on the film thickness on the magnetic disks, the relationship between the light intensity and the film thickness has been simulated according to the air / film / magnetic disk structure, and the refractive indices are 1, 1.3, and 2.35-3.93i, respectively. The incident angle θ_0 = 60 deg is set, in addition the wavelength of the light λ is 550nm. The null condition is obtained when the *P*, *Q* and *A* are set at -27.7 deg, 45.0 deg and -53.0 deg, respectively. The result is shown in Fig. 2.11, and it also indicates that the intensity is a periodic function of the film thickness, and its period is about 283 nm.

2.2.2 Drawback of Conventional EMs

Since EMs is based on the principle of measurement of multi-point light intensity distribution, it is necessary to measure the light intensity of the sample surface point by point. Therefore, uniform, parallel and oblique incident light is required. In addition, in order to improve the lateral resolution, objective lenses with a high magnification ratio or large numerical aperture (NA) must be used, which can magnify the light intensity distribution and make the image of the sample on the CCD camera, as shown in Fig. 2.12. Diffraction-limited resolution γ is determined by the wavelength λ and the NA of the objective lens and can be provided by (35)

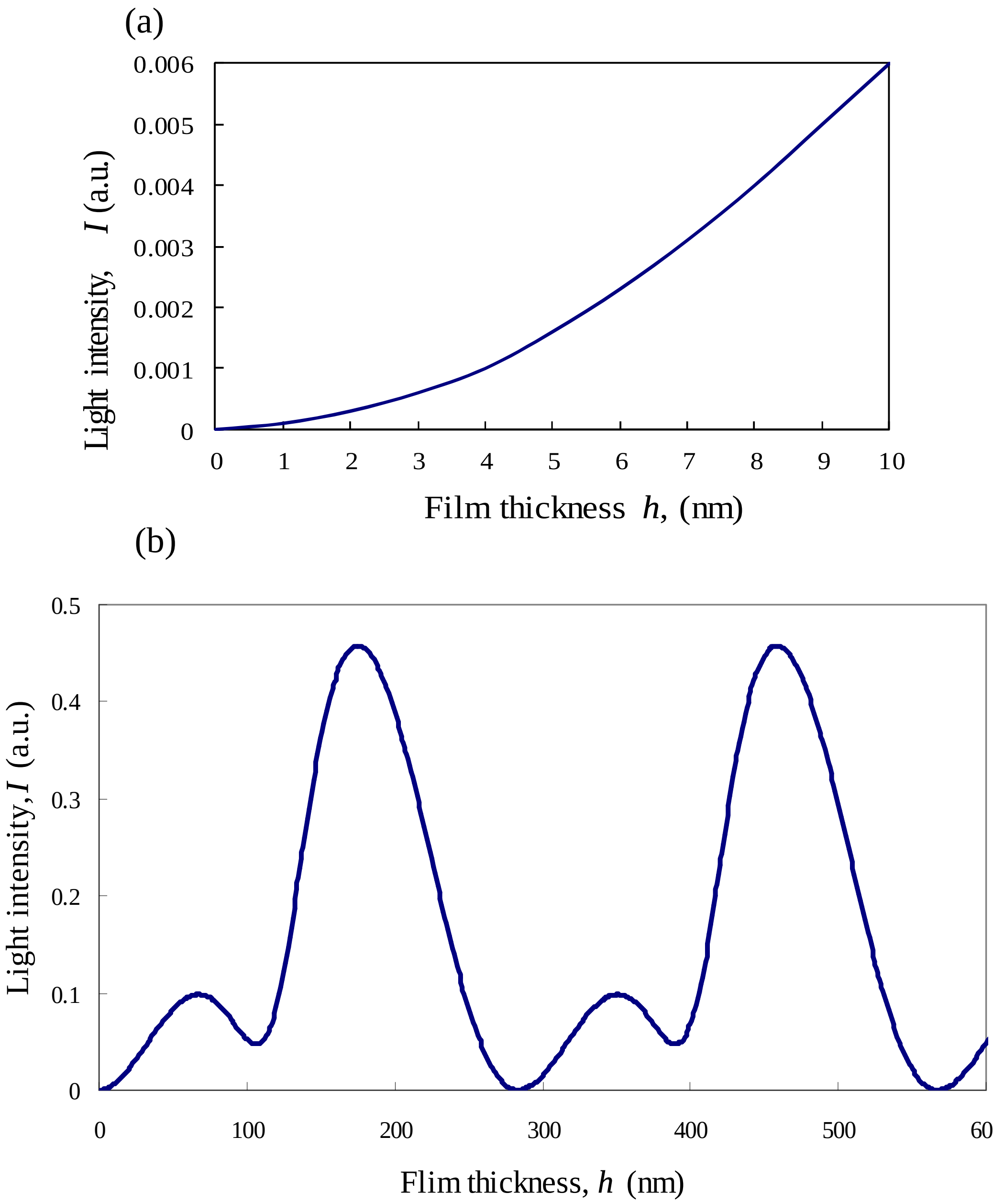

Fig. 2.11 Simulated results of film thickness vs. light intensity. (a) Relationship between light intensity and film thickness at null condition (h = 0~10 nm). (b) Relationship between light intensity and film thickness at null condition (h = 0~600 nm) as a periodic function.

$$\gamma = 0.61\frac{\lambda}{\mathrm{NA}}, \tag{2.44}$$

where

$$\mathrm{NA} = N_0 \sin U \ . \tag{2.45}$$

Here, N_0 is the refractive index of the media, and U is the half of the angular aperture. It is clear that large NA leads to high lateral resolution from Eq. (2.44). In other words, objective lenses with a large NA is needed for EMs to obtain high lateral resolution, however, this method has a drawback that high resolution lens causes the narrow field of view.

In optics, depth of field (DOF) is the distance between the nearest and farthest objects whose images are acceptably sharp. Since the region in focus is limited, sharpness of the image decreases on each side of the focal point, so that within the DOF, the unsharpness is negligible under normal imaging conditions (36). The relationship between the DOF and NA is given by

$$DOF = 2\frac{\lambda}{\mathrm{NA}^2}, \tag{2.46}$$

Since the objective lens is set obliquely to the sample surface in EMs, as shown in Fig 2.12, the focus area (FA) that is determined by DOF, can be expressed by

$$FA = 2\frac{\lambda}{\mathrm{NA}^2 \sin\theta_i} \ . \tag{2.47}$$

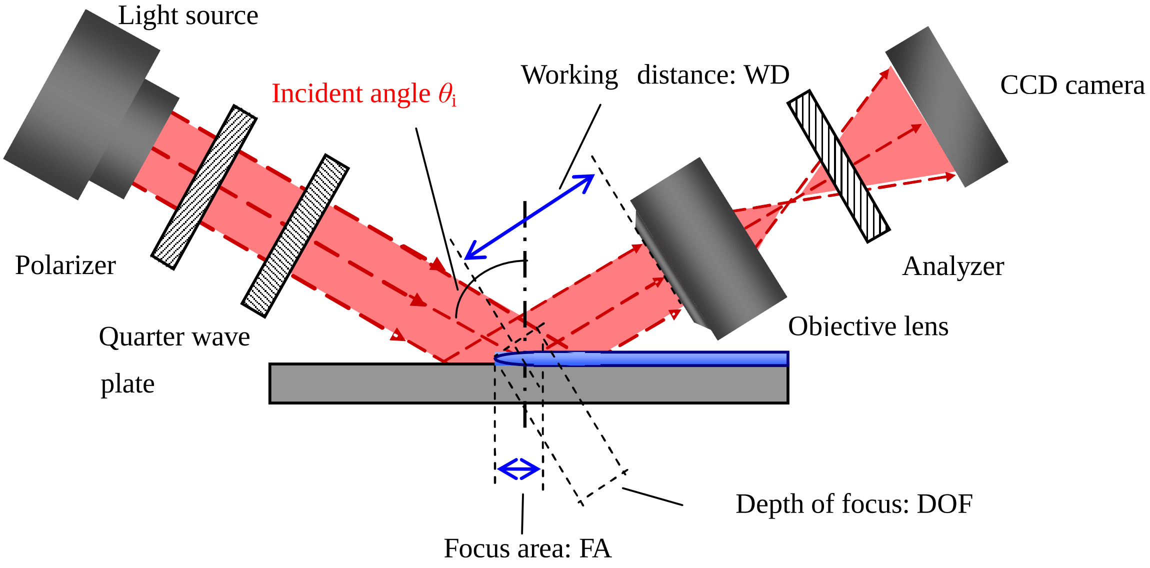

Fig. 2.12 Setup of an EM.

This equation means that FA becomes smaller with increase of NA. For example, using an objective lens with NA = 0.95, the incident angle of 60 deg, and the light wavelength of the light is 550 nm, the lateral resolution γ is estimated at 0.35 µm from Eq. (2.44), and FA is only 1.4 µm according to Eq. (2.47). This is ther reason why a high resolution lens causes the narrow field of view in EMs. Thus, EM has a drawback that the observation with high lateral resolution is difficult due to the narrow FA for high NA lenses.

In addition, observation with high lateral resolution is difficult due to a geometrical reason. Working distance (WD) of objective lens with high NA is usually small. Fig. 2.13 shows geometric relationship of the diameter of the objective lens and WD in the case of oblique observation for EM. The condition where the sample and the objective lens do not contact can be expressed by

$$\mathrm{WD} > \frac{D_{obj} \tan \theta_r}{2}, \tag{2.48}$$

where θ_r is the angle of reflaction, and D_{obj} is the diameter of the objective lens. D_{obj} is around 25 mm typically and $\theta_r = \theta_i$ (60~80 deg), so, according to Eq. (2.47), WD should be larger than 22 mm for usual setups. However, the NA of objective lens that satisfies this condition is about 0.3 at most, and the lateral resolution is about 13 μm (37).

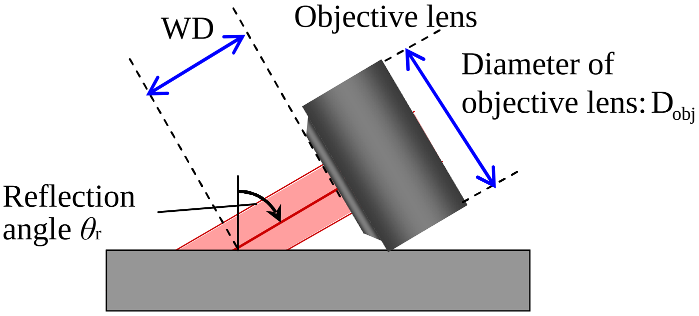

Fig. 2.13 Mechanical interference of an objective lens.

2.3 Vertical-Objective-Based EM (VEM)

To overcome this drawback, vertical-objective-based EMs (VEMs) were recently proposed and the feasibility was demonstrated (27, 28, 38). In the VEM, the objective lenses are set vertically to obtain the high lateral resolution and the off-axis light is focused onto the back focal plane of the objective lens to get the oblique illumination as shown in Fig. 2.14. Although a usual objective lens consists of a group of lenses, an effective lens is considered as shown in the figure instead. The incident angle θ_i can be adjusted by changing the shift distance from the main axis. Objective lens is used for both a condenser lens for illumination and an imaging lens. The typical setup of a VEM is shown in Fig. 2.15. Parallel light beam from the light source passes through the polarizer and quarter wave plate, and then focuses on the back focus plane of the objective lens by a collector lens. Here, this type of illumination is called off-axis Kohler illumination. After the objective lens, the light beam becomes parallel again and incident on the sample surface at a certain angle. The reflected light from the sample passes through the objective lens and the analyzer. After the imaging lens, ellipsometric contrast is imaged on CCD camera. This imaging system is similar to the setup of an optical microscope with infinity corrected optical system.

In the VEM, since the objective lens is set vertical to the sample surface, FA is no longer determined by DOF, which is determined by NA, and the whole area of illumination on sample surface can be focused. Therefore, large NA of objective lens can not reduce the the field of view, and it is determined by the area of illumination and size of the imaging device (CCD camera) in VEM. Selecting the appropriate magnification for the lens group and size of CCD camera to match the magnification, large field of view can be obtained. Meanwhile, large NA of the objective lens can be choosen for high lateral resolution.

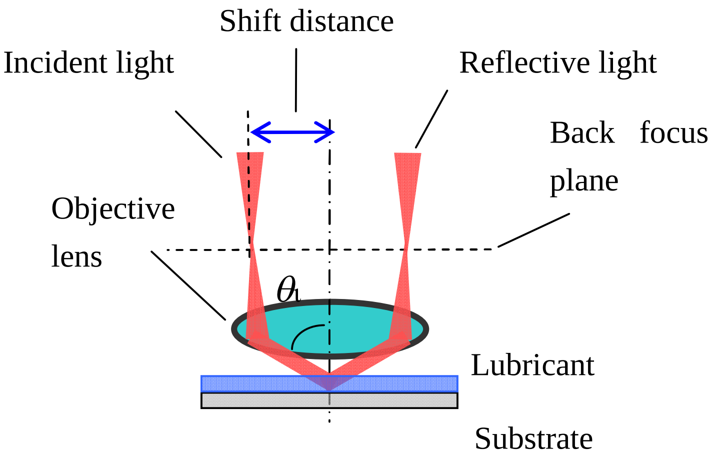

Fig. 2.14 Off-axis parallel light generation by focusing light on a back focal plane.

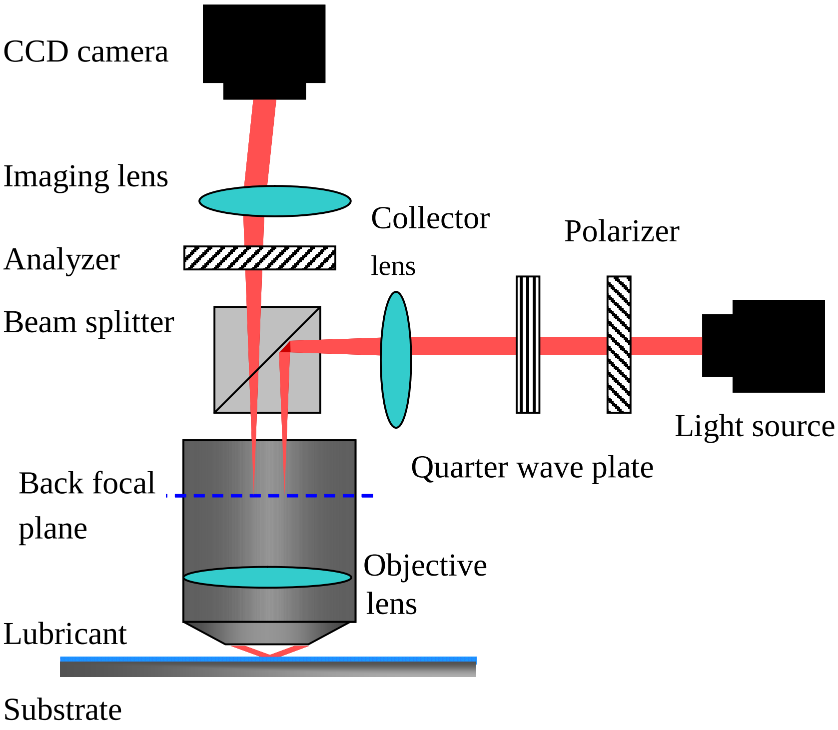

Fig. 2.15 Setup of a VEM.

Chapter 3　Materials

In order to achieve a high recording density in magnetic disk, contact or near-contact HDI will be required. In this type of HDI, the magnetic head flies on the magnetic disk with a liquid lubricant film of thickness of 1 ~ 2 nm applied on the surface. The characteristic of the lubricant film on magnetic disk is important to the improvement of recording desity. Therefore, visualization methods of nm-thick lubricant films are always used to obtain the characteristic of the lubricant film on magnetic disks. Thus, based on this background, magnetic disks with lubricant were chosen as the samples in this study. In this chapter, the materials such as the disk, lubricants, and the method for applying the lubricant to the substrate is explained.

3.1　Magnetic Disks and Lubricants

3.1.1　Disks for Longitudinal Magnetic Recording and Perpendicular Magnetic Recording

Magnetic disks were used as a substrate in this study. Figure 3.1 shows the types of magnetic recording (5). Digital data to be recorded on the magnetic disk are stored in the bit cells, which are arranged in the magnetic layer (recording medium). Each bit cell is a very small magnetic unit. Signals of 1 or 0 are recorded by using the direction of magnetization. Magnetic head roughly consists of a read element and inductive write element in any of the recording method. An inductive write element includes a coil layer, and a gap is formed between the first and second pole piece layers by a gap layer on an air bearing surface. The pole piece layers are connected to from a closed magnetic circuir. Current conducted to the coil layer induces a magnetic flux in the pole pieces that causes a magnetic field at a write gap on the air bearing surface for the purpose of switching the magnetization direction on the magnetic disks. In recent read element designs of the head, a spin value sensor, giant magnetoresistive (GMR) sensor has been employed for sensing magnetic fields from the rotating magnetic disk, which detects the change of the electrical resistance due to the change of the direction of magnetization from the bit cell according to the magnetoresistance effect.

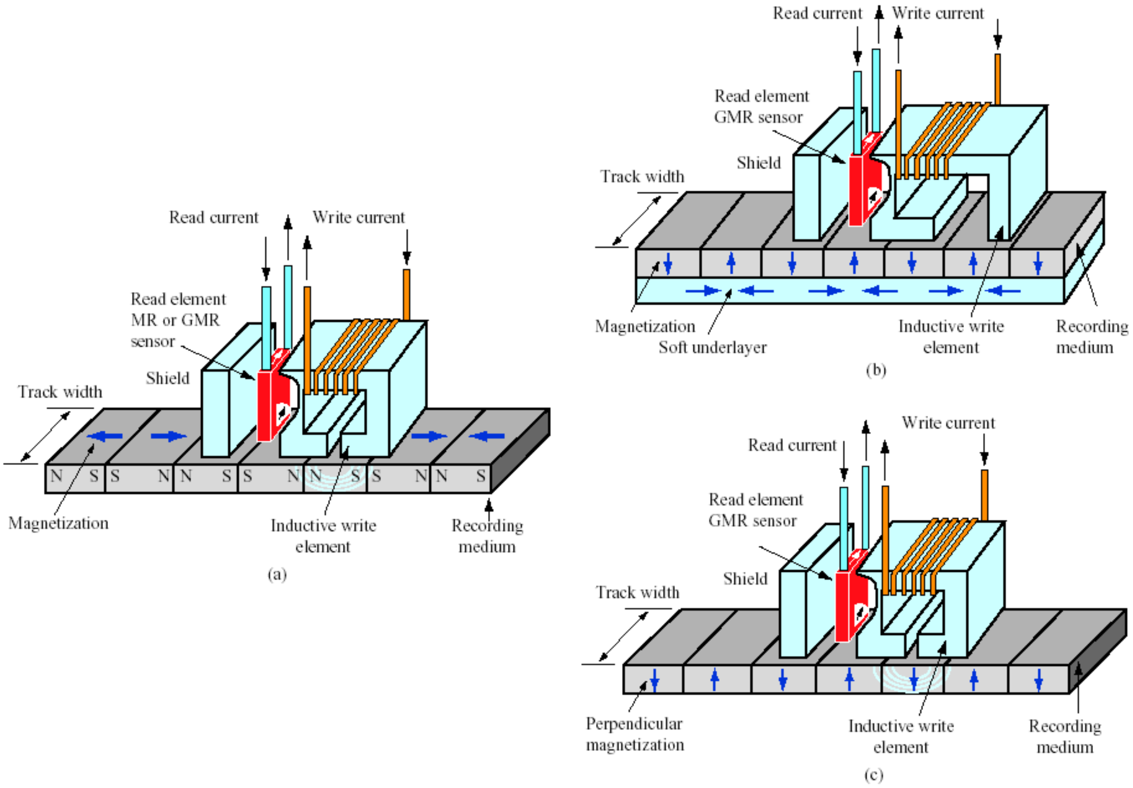

Fig. 3.1 Types of magnetic recording: (a) Longitudinal magnetic recording. (b) Perpendicular recording, using a probe head and a soft underlayer in the medium. (c) Perpendicular recording, using a ring head and no soft underlayer.

Current magnetic recording technology is divided into two types. One is is longitudinal magnetic recording (LMR), which placed the magnetization of the bit cell in-plane direction of the disk (Fig. 3.1(a)). And the other is perpendicular magnetic recording (PMR), which placed the magnetization vertically to the plane of the disk (39), (Fig. 3.1(b) and (c)). LMR is used to be a major recording method, however, it is considered to have difficulty due to thermal stability when areal density is more than 40 to 100 Gb / inch^2. PMR was invented in 1975 and commercialized for the first time in 2005. It is becoming a mainstream, replacing LMR.

Thus, magnetic recording technology is shifting from LMR to PMR. One significant difference between the two media is that the total thickness of the magnetic recording related layers is significantly thicker in PMR case, than that in LMR case. In general, the thicker the sputtered layers, the greater the surface roughness is. In addition, in the LMR disks, a subnanometer-high groove structure in a circumferential direction, which is called nanotexture, is fabricated by abrasive machining of rotating magnetic disks to improve their recording properties. In this study, both 3.5 inch LMR disks and 2.5 inch PMR disks were used as the sample substrate. The thickness of LMR disk and PMR disk were 1.25 mm and 0.635 mm, respectively. It consisted of DLC, longitudinal magnetic recording layer, intermediate layer, underlayer and Al substrate in LMR disk, as well as DLC, perpendicular magnetic layer, intermediate layer, soft magnetic layer and glass substrate in PMR disk. The arithmetic average roughness R_a was about 0.23 nm and 0.37 nm for LMR disk and PMR disk, respectively.

3.1.2 Sample Lubricant

Polar and nonpolar perfluoropolyether (PFPE) lubricants (Fomblin Zdol4000 and Z03, Solvay Solexis) with molecular weight of about 4000 g / mol were used as test lubricants. Their molecular structures are given in Fig. 3.2. The symbol of ⓧ is the end group of the lubricants, which is different between the Zdol4000 and Z03. Figure 3.3 shows the structure of Zdol4000. The cross-sectional area of the straight chain is about 0.6 ~ 0.7 nm and the length of the Zdol4000 and

Z03 is about 14 nm. The end group of the lubricant molecule tends to take the shape of a random coil, as shown in Fig. 3.4. Because the lubricant molecules always change its shape by thermal fluctuations, the radius of molecules is obtained as the statistical value, not determined uniquely. The radius of gyration shown in Table 3.1 is the value that was estimated using the formula of the relationship between the molecular weight M_n and the radius R_g, and the molecular weight in Ref. (40),

$$R_g \propto M_n^{1/2} . \tag{3.1}$$

It is known that the lubricant molecules on the substrate take the flat shape rather than the random coil in the bulk state (41). It is possible that a thickness of about 2 nm can completely covered the surface of the substrate.

Table 3.1 Properties of PFPE lubricants (Zdol400, Z03).

Properties	Zdol4000	Z03
End group, X	$-CH_2OH$	$-CF_3$
Molecular weight, M_n (amu)	4000	4000
Vapor pressure at 20 ℃ (Torr)	1×10^{-8}	—
Vapor pressure at 100 ℃ (Torr)	1×10^{-4}	—
Surface tension at 20 ℃ (dyne/cm)	22	23
Radius of gyration R_g (nm)	1.5	1.4
Viscosity at 20 ℃ (Pas)	0.18	0.05

Difference between the two types of lubricants Zdol4000 and Z03 is the chemical structure of the end group (ⓧ in Fig. 3.2). Both ends of the Z03 are terminated with fluorine. On the other hand, both ends of the Zdol4000 are terminated with hydroxyl group. The interaction between molecules is stronger than the effect caused by molecular polarity of the hydroxyl group for Zdol4000. In addition, it is known that Z03 molecules adsorb physically onto the magnetic disk. The Z03 molecule is easy to move because it adsorbs weakly by physical adsorption. Zdol4000 molecules chemically adsorb onto the magnetic disk by the polar end groups. However, the chemical adsorption does not occur for all the molecules on the disk, some of the molecules physically adsorb and are easy to move. The ratio of the amount of bonded and mobile molecules is represented by bonding ratio, which is defined as the ratio of the amount of the molecule that bonded on the substrate comparing with the total amount of molecules containing in the lubricant film.

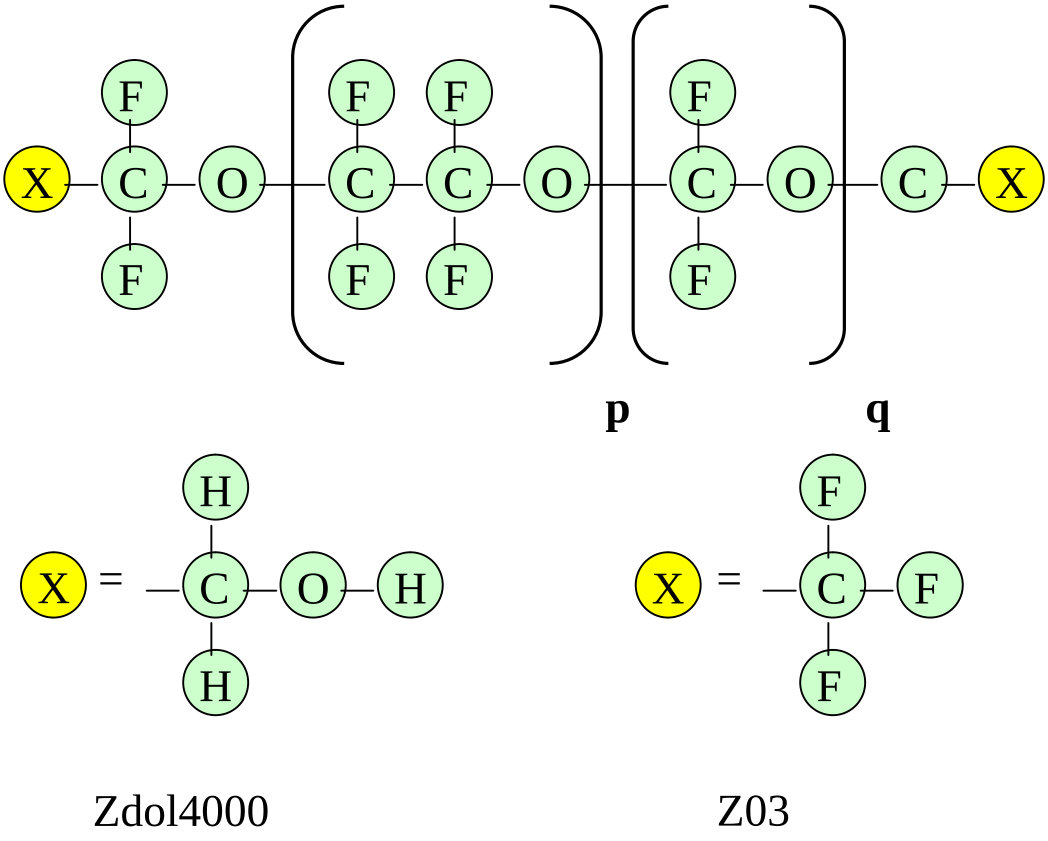

Fig. 3.2 Chemical formula of lubricant of Fomblin Zdol4000 and Z03.

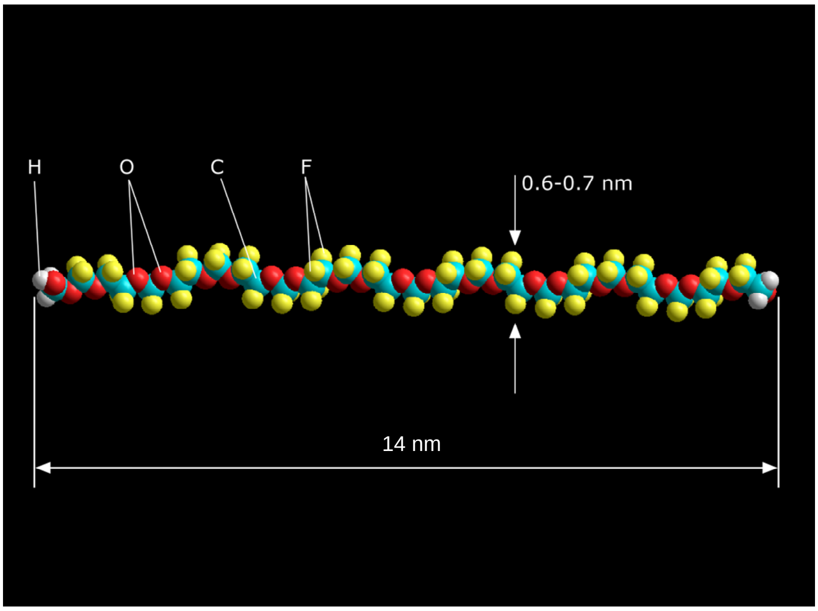

Fig. 3.3 Structure of PFPE Zdol with a molecular weight of 4000 amu.

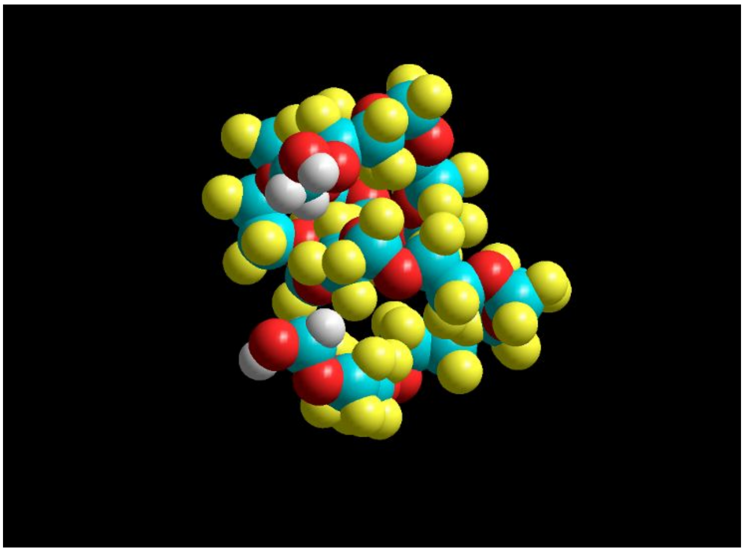

Fig. 3.4 Molecular conformation of Zdol4000 with a shape of random coil.

3.2 Lubricant Application Method

The lubricant film was applied onto the disk by a dip coating method. An overview of the dip coating method is shown in Fig. 3.5. First, a solution was prepared by diluting the lubricant with a highly volatile solvent. Next, the substrate was placed to be the lubricant solution vertically to the liquid surface with a hand-made stage, which was driven by a stepping motor, and put the disk down so that a part of the disk was immersed into the solution, and then drew the disk up from the lubricant solution at a constant rate without any pause. Since the volatile of the solvent is high, evaporation from the disk surface happens immediately after the dip; simultaneously the lubricant molecules with low volatility are left on the disk surface to form a thin lubricant film. In this way, the thickness of the lubricant film on the disk can be adjusted with a precision of the order of 0.1 nm by adjusting the removal speed and lubricant solution density. As mentioned in 3.1.2, in this study, the solvent using for diluenting Zdol4000 and Z03 is hydrofluoroether: HFE-7200, and the properties of HFE-7200 is shown in Table 3.2.

Table 3.2 Properties of HFE-7200.

Properties	HFE-7200 ($C_4F_9OC_2H_5$)
Boiling point temperature (℃)	76
Freezing point temperature (℃)	-138
Vapor pressure (MPa)	0.0160
Density (kg／m^3)	1430
Viscosity (Pas)	5.7×10^{-4}
Surface tension (mN／m)	13.6
Aqueous solubility (ppm(Wt))	20

The removal speed was adjusted between 0.5 ~ 2.6 mm / sec, the concentrations of the solution were 0.15%, 0.2% and 0.6% in this study, and the disk in the solution without staying during the dipping process. The environment temperature and relative humidity were about 23~26 ℃ and 60%~70%rh for both application process and thickness measurement, respectively.

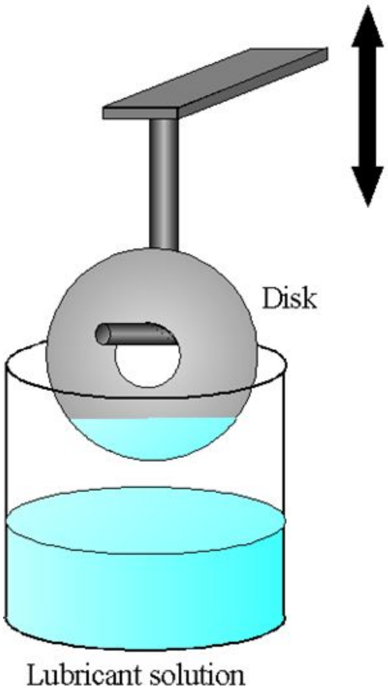

Fig. 3.5 Schematic diagram of a dip coating method.

3.3 Measurement for Film Thickness

In this study, we evaluated the lubricant film thickness using a scanning ellipsometer (MARY-102, Five Lab). In Fig. 3.6, and Fig. 3.7 the optical system of the ellipsometer and the outward appearance of it are shown, respectively. Table 3.3 shows the specification for it. In this device, He-Ne laser light is obliquely incident on the sample surface and it is elliptically polarized with a polarizer and quarter wave plate. As explained in section 2.1.3, thickness of the sample is obtained by analyzing the polarization state of reflected light. By scanning the laser spot, it is possible to measure the distribution of the film thickness in one or two dimensional. Resolution of in-plane direction of the ellipsometer is determined by the diameter of the laser spot. The diameter of the laser spot of the ellipsometer used in this study is about 35 μm. The obtained film thickness is considered to be the film thickness averaged in the laser spot. The lubricants of Zdol4000 and Z03 have almost same refractive indices of n = 1.3, which are widely used in HDDs. And the refractive index n and extinction coefficient k of the magnetic disk are measured by ellipsometer for the unlubricated disk.

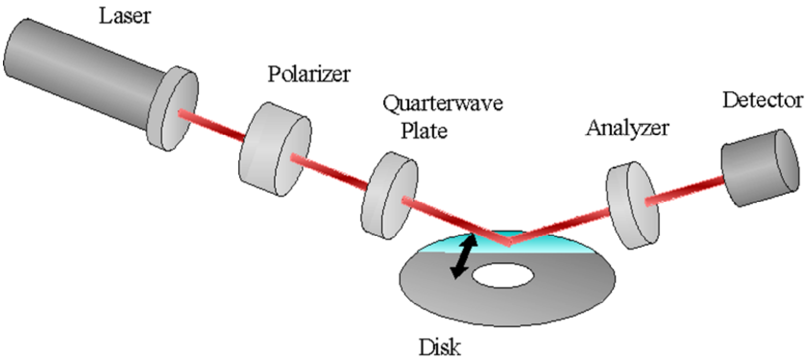

Fig. 3.6 Schematic diagram of the scanning ellipsometer.

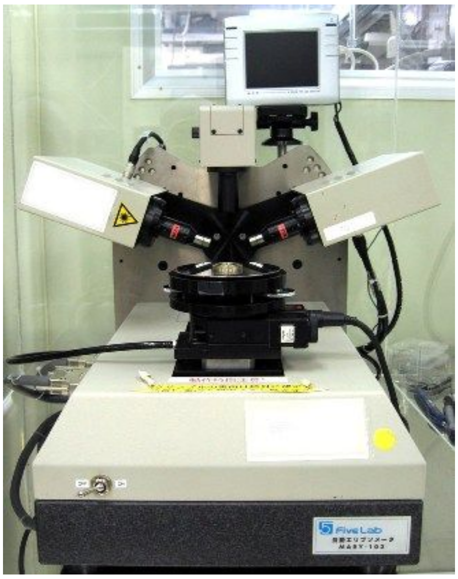

Fig. 3.7 Photograph of the scanning ellipsometer (MARY-102).

Table 3.3 Specifications of the scanning ellipsometer (MARY-102).

Method	Rotating retarder method
Light source	He-Ne laser (λ : 632.8 nm) MAX 0.8 mW
Beam dia.	35 μm
Incident angle	45°-90°, 0.01°step
Accuracy	Δ=±0.01° Ψ=±0.01°
Sample time	0.05 sec min

Chapter 4 Imaging characteristics of VEM and Thickness Determination

4.1 Introduction

As described in Chapter 2, EM can provide thickness distribution as a dark-bright contrast image. Although EM is expected to be a useful tool for observation of lubricant on magnetic disks, conventional EMs have a drawback of low lateral resolution of several μm. To overcome this drawback, vertical-objective-based EMs (VEMs) were proposed, however, the method has not been established. Especially, imaging characteristics of VEM is not clarified and a method for thinness determination has not been established. The imaging characteristic is important for evaluation of lateral resolution and thickness calibration where the ellipsometric signal is converted to the thickness is essential to quantitative measurement. In this chapter, after setup of VEM is explained, the imaging characteristic is investigated and a method for the thickness determination is proposed.

4.2 Setup of VEM

Based on ellipsometry, the sample is illuminated with a light at a large incident angle to improve the ellipsometric image contrast. To meet this demand, in conventional EMs, the objective lens is obliquely set to the sample surface. However, this leads to a narrow field of view when high resolution objective lenses are used. That means sample scanning is necessary, which is not suited for the real-time visualization. In the VEM, the objective lenses are set vertically to obtain the high lateral resolution that is free from the problem of narrow field of view by introducing the off-axis

Kohler illumination as described in Chapter 2. The details of setup of VEM are decribed below.

4.2.1 Off-Axis Kohler Illumination System

Figure 4.1 shows the setup for illumination system of VEM. In this system, a super luminescent diode (SLD) with NA of 0.5 was used as a point light source. Since a conventional inverted microscope (IX71, Olympus) was used in the system, in which Lens 2 (focal length f_2 = 200 mm) and objective lens (focal length f_o = 3.6 mm) were already mounted, the design of the illumination system was required to adapt to the microscope. A lens with a focal length f_1 of 80 mm was chosen as Lens 1 to create the parallel light. The oblique incidence was obtained by shifting the light source away from the main axis, and the incident angle θ can be given by

$$\theta = \arcsin\frac{H}{f_o}, \tag{4.1}$$

where H is the shift length of the light source image on the back focal plane of the objective lens. After optical consideration, the shift length of the light source h can be obtained by

$$h = \frac{f_1}{f_2}H. \tag{4.2}$$

Thus, when the incident angle θ = 60 deg, and f_o = 3.6 mm, f_1 = 80 mm, f_2 = 200 mm, the the shift length of the light source h is estimated at about 1.25 mm from Eq. (4.2). As mentioned above, the objective lens was fixed in the microscope; it was difficult to measure the incident angle θ directly. Therefore, we measured the incident angle by a method shown in Fig. 4.2. The incident angle can be obtained by the shift length *s* of the light spot from the main axis. In this measurement the laser spot was defeted away from the front focal plane, and the distance between the front focal plane and the detectionplane is expressed by r_0 in Fig. 4.2. The incident angle θ can be given by

$$\theta = \arctan\frac{s}{r_o}, \tag{4.3}$$

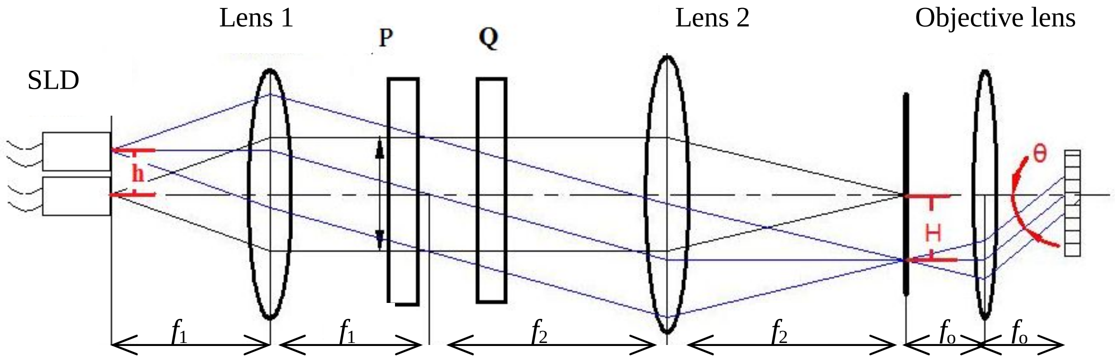

Fig. 4.1 Schematic of off-axis Kohler illumination system setup for generation of the oblique parallel light.

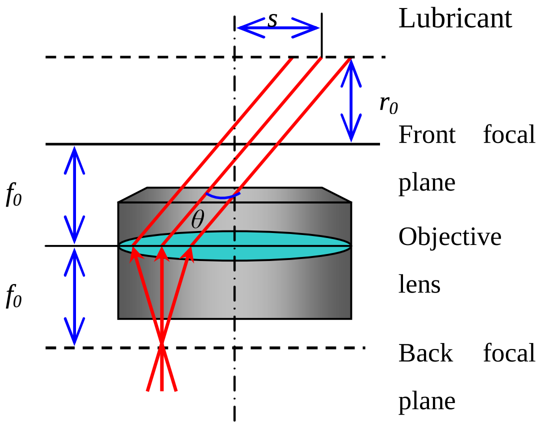

Fig. 4.2 Experimental setup for measurement of imcident angle *θ*.

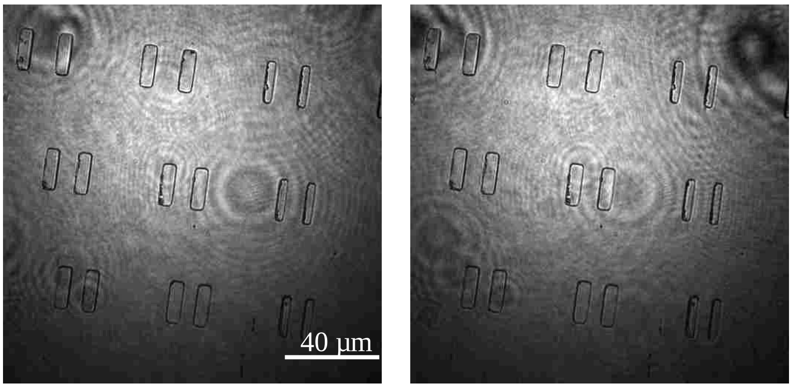

(a) θ = 0 deg (b) θ = 50 deg

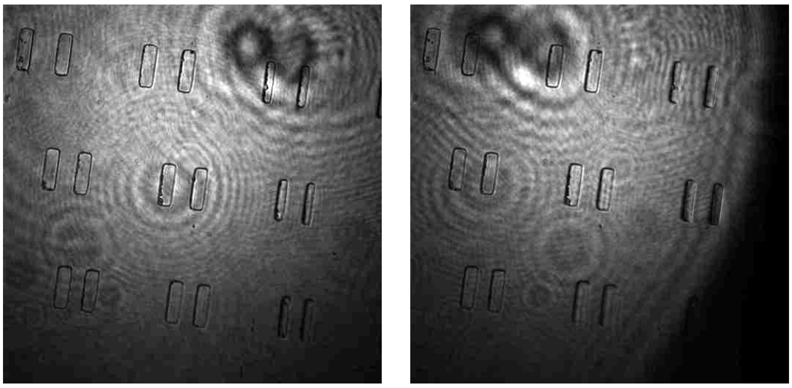

(c) θ = 60 deg (d) θ = 70 deg

Fig. 4.3 Images of VEM for different incident angles.

The images of the VEM for different incident angles are shown in Fig. 4.3. The incident angle was set 0, 50, 60 and 70 deg in this experiment. The sample used in this experiment was a silicon substrate with some partterns. The patterns were formed by a variety of grooves with a depth of 500 nm, which were fabricated by dry etching the substrate Si. Figure 4.4 shows the arrangement of the patterns. In the figure, the black area is etched region. The size of the minimum pattern is 5 × 20 μm^2 which can be seen in Fig. 4.3. So the imaging area of this illumination system can be measured by using this sample. The measured area of the image is 160 × 160 μm^2. As explained in Chapter 2, significant difference of the reflectivities between p- and s- polarized light can be obtained when the incident angle equals to the Brewster angle, which is around 70 deg, so the angle of 60 or 70 deg should be chosen rather than 0 or 50 deg. However, when the incident angle was increased up to 70 deg, the sample could not be fully illuminated due to the limit of the diameter of the objective lens (diameter d_o = 6.84 mm). Therefore, 60 deg of the incident angle was chosen in this study.

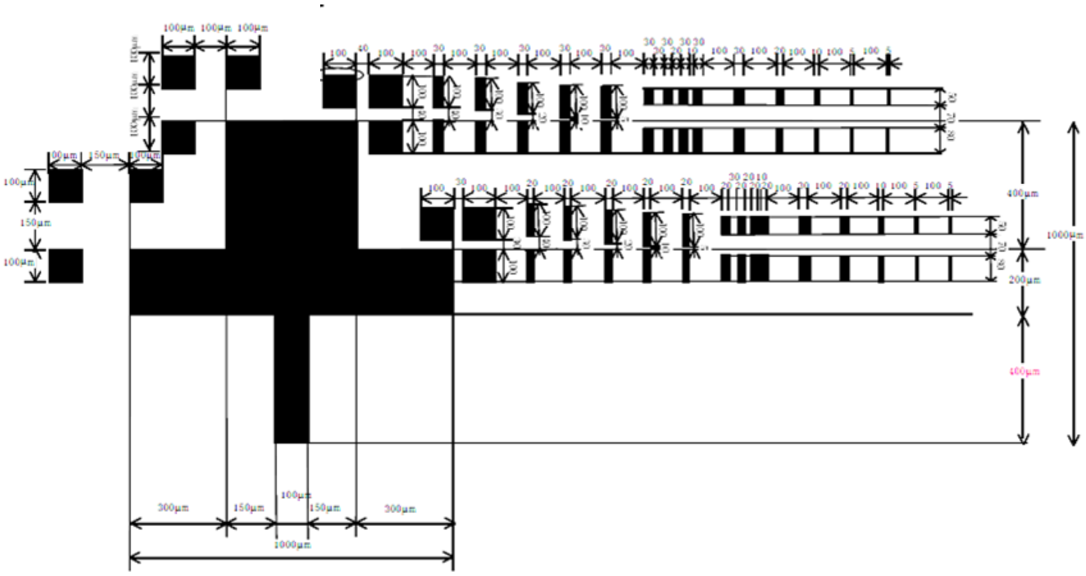

Fig. 4.4 Schematic arrangement of pattern on the silicon wafer.

4.2.2 Light Source

EMs generally require a monochromatic light. Laser light sources are good candidates for the monochromatic light source because the laser light intensity can be modulated at high frequency, which is higher than that of a filtered light from usual lamp light sources. However, laser light sources may generate noise images due to the optical interference because the coherence length of the usual lasers is longer than the distance of the optical devices. In our VEM, in order to reduce the temporal coherence, a SLD (ASLD68-050-B-FA, Amonics) was used as a light source. The specifications of the SLD are shown in Table 4.1.

Table 4.1 Specifications of ASLD68-050-B-FA.

Properties	
Center wavelength, λ (nm)	679.624
Output power (mW)	> 3.9
3 dB bandwidth (nm)	7.29
Output stability	+/- 0.02 for 8 hours

Table 4.2 Specifications of SK-11-MG-5.

Properties	
Wavelength, λ (nm)	450 ~ 950
Entrance pupil (mm)	5 standard
Exit pupil (mm)	5 standard
Transmission	>50% at 550 nm
Size (mm)	110(H) × 140(W) × 55(L)

In the images shown in Fig. 4.3, a number of concentric interference fringes on the image can be seen. Since the VEM converted the light intensity of the image to the film thickness as explained in Chapter 2, the interference fringes are the background noise image, therefore, elimination of these interference fringes is mandatory for VEM. The interferenc noise is considered to be caused by the spatial coherence due to the small diameter of SLD (the theory of the coherence will be described in detail in Chapter 5). Therefore, a bandle-fiber-based device, called speckle killer (SK-11-MG-5, Nanophoton) was used to reduce the speckle coherent noise. The specification of the speckle killer is shown in Table 4.2, and the appearance is shown in Fig. 4.5. The image taken by VEM with the speckle killer is shown in Fig. 4.6. Comparison between Fig. 4.3 and 4.6 indicates that speckle killer reduced the coherent noise and successfully improved the image quality.

Fig. 4.5 Speckle killer unit.

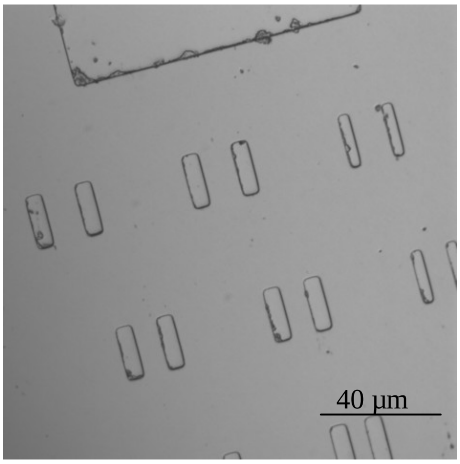

Fig. 4.6 Silicon pattern images obtained by VEM with speckle killer.

4.2.3 Optical System of VEM

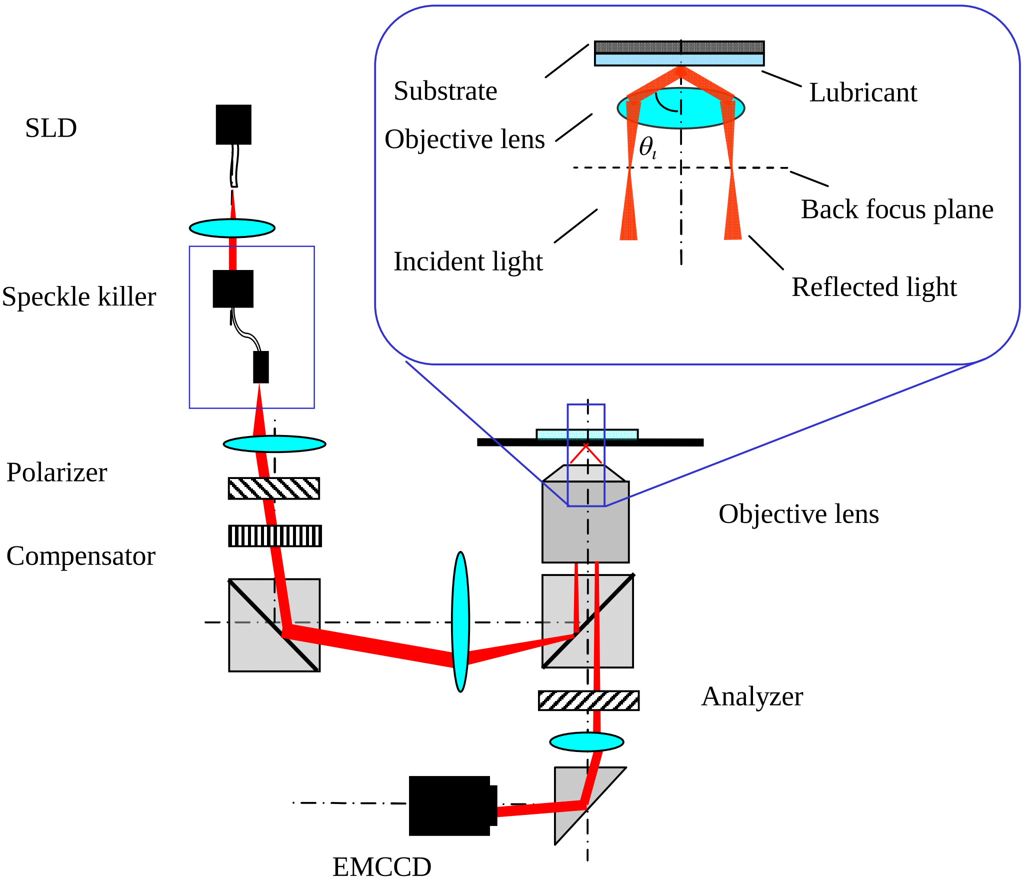

Fig. 4.7 Schematic setup of VEM.

The schematic of our VEM is shown in Fig. 4.7. As described in Section 4.2.1, a commercial inverted microscope was modified and an objective lens with a numerical aperture (NA) of 0.95 was used. In our setup, the incident angle was set to be 60 deg. In order to reduce the temporal coherence, a SLD was used as the light source whose wavelength λ was about 680 nm and the coherence length was 63.3 μm. In addition, a bandle-fiber-based device, called speckle killer, was used to reduce the spatial coherence as described in Section 4.2.2. The light reflected from the sample was imaged through the objective and imaging lenses onto a highly sensitive electron multiplying CCD camera (Cascade II:512, Photometrics) with an area of 8 × 8 mm^2 and 512 × 512 pixels. And area of one pixel is 0.31 × 0.31 μm^2 on the image.The vertical setting of the objective lens to the sample surface can provide diffraction-limited lateral resolution γ and a sufficiently wide field of view. Diffraction-limited resolution γ is determined by the wavelength and the NA of the objective lens and can be provided by Eq. (2.44). γ is estimated at about 0.41 µm in this experiment. The area in focus was about 160 × 160 μm^2, which means that the field of view is wide enough to provide imaging without scanning. The developed setup of the VEM is shown in Fig.4.8 as a photograph.

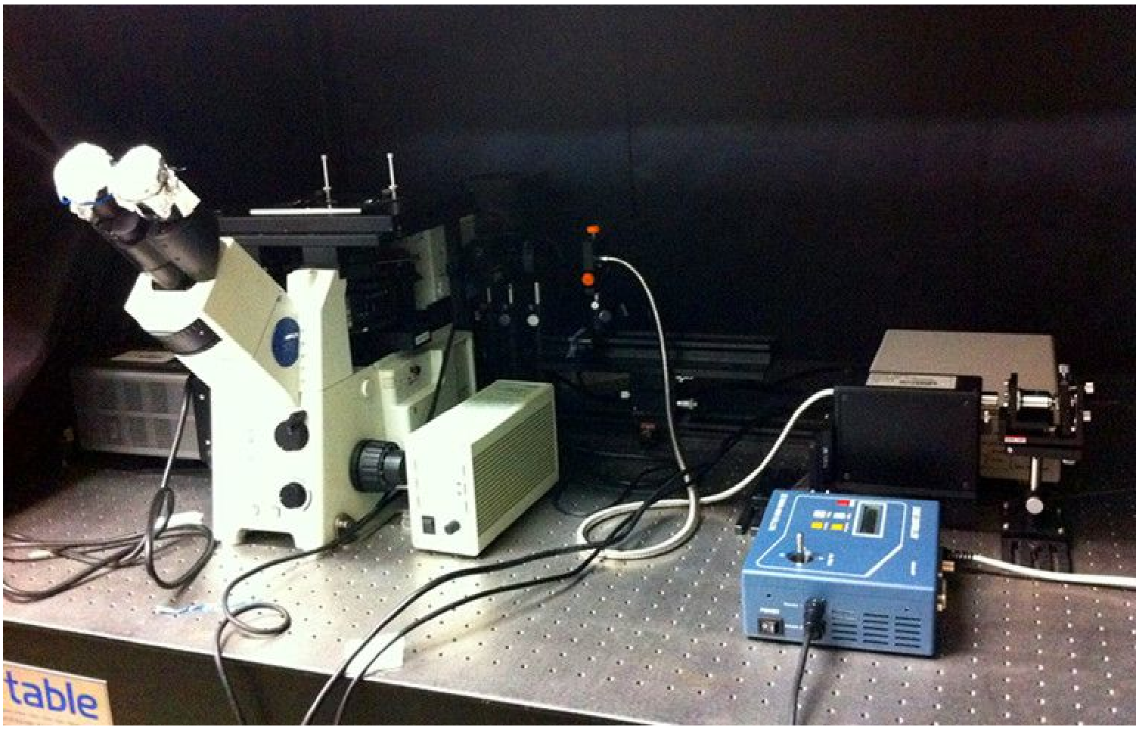

Fig. 4.8 Photograph of VEM.

4.3 Method for Conversion from Light Intensity to Thickness

In real-time visualization, thickness distribution of the lubricant film is determined by the light intensity. In order to convert the light intensity I to the thickness h directly, linear relationship between I and h is expected. For the calibration, an instrument such as an ellipsometer is usually used to obtain the film thickness. In this study, a new method for calibration called phase shift method was provided. Using this method, VEM could provide the film thickness by itself without any other instruments.

4.3.1 Conversion by Using the Linear Relationship

In EMs, a sample is illuminated by parallel and oblique light with well defined polarization. The measured quantity is the change of polarization due to light reflection at the sample. The ellipsometric angles ψ and Δ, which are used to describe the change in polarization, are given by Eq. (2.20). Moreover, the intensity signal of ellipsometric microscope I is generally given by Eq. (2.39). Usual ellipsometers can only carry out single-point measurement at one time, which is not suitable for real-time visualization of deforming liquid films because it requires too much time. If visualization method can directly convert the intensity I of all the points of the sample to the film thickness h at a time, the method can provide real-time visualization. We used the phenomenon that the relationship between image intensity I of EMs and film thickness h depends on the angles of the polarization devices; polarizer, quarter wave plate, and analyzer. Figure 4.9 shows the effect of the polarizer angle on the relationship between I and h. Here, the I-h curve was obtained by using 2 × 2 matrix method, which was described in Chapter 2. The layer model consisted of air, lubricant film and magnetic disk as a substrate, whose refractive indices were 1, 1.3, and 2.35-3.93i, respectively. The air and disk were semi-infinitely thick. The null condition for the unlubricated disk was achieved when the angles of analyzer and polarizer are A_d = 53.2 deg and P_d = 28 deg, respectively. Here, these values were obtained by using Eqs. (2.42) and (2.43). The null condition commonly used for null ellipsometry as explained in Section 2.2. I-I_d in the figure expresses the normalized intensity difference between the lubricated and unlubricated disks. The intensity was normalized by the incident light intensity. Figure 4.9 shows that the intensity difference I-I_d is approximately proportional to the thickness h at P = 55 deg. The fitting curve of the data at P = 55 deg to a straight line is shown in Fig. 4.9. Diviation from the straight line can be found for P = 60 or 65 deg. Therefore, P = 55 deg was chosen as the condition that gives the linear relationship between I-I_d and h. This result indicates that the polarizer angle can be adjusted so that the intensity difference I-I_d is approximately proportional to the thickness h in VEM. This can provide a direct conversion from I to h. This can provide real-time thickness measurement in the observation.

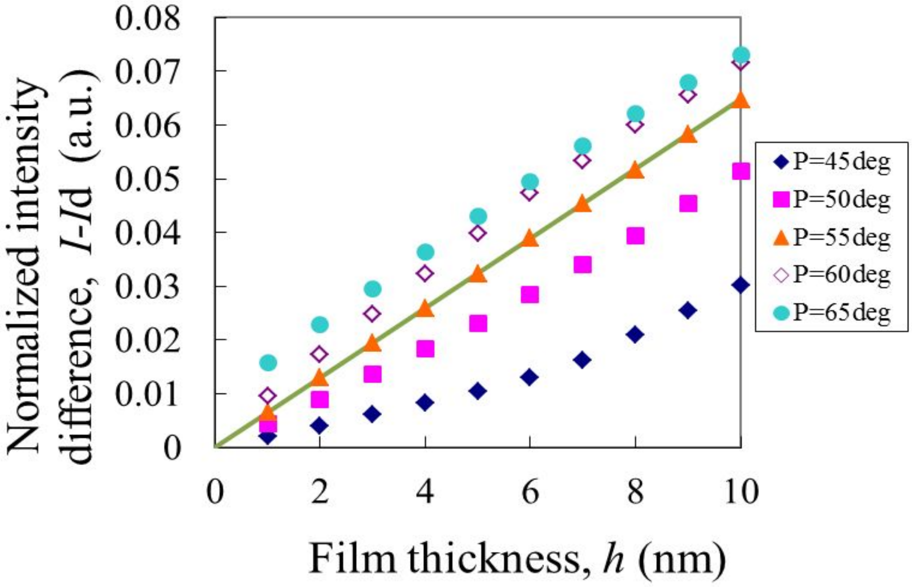

Fig. 4.9 Simulated relationships between intensity and thickness for different polarizer angles *P*.

4.3.2 Thickness Determination by a Phase Shift Method

To convert I to h, the measurement of h is needed. If VEM itself can measure the film thickness, any other measurement devices such as an ellipsometer is not needed. For this purpose, based on a phase shift method, a thickness measurement method for the VEM was developed. When the thickness is small, the phase shift $|\Delta - \Delta_d|$ is approximately proportional to the thickness $^{(26)}$.

$$h = \frac{1}{\alpha}\left|\Delta - \Delta_d\right|. \tag{4.4}$$

Here, Δ and Δ_d are the phase shifts between p- and s-polarized lights for lubricated and unlubricated disks, respectively. Here, Δ_d is the phase shift at the null condition. Using the relationship as shown in Eq. (4.4), the thickness h can be determined if the coefficient α and the phase shift $|\Delta - \Delta_d|$ are obtained.

The coefficient α was theoretically obtained using the 2 × 2 matrix method. When the wavelength of light λ is 680 nm, and the refractive indices of the lubricant and disk are $N_1 = 1.3$ and $N_2 = 2.35\text{-}3.93i$, the coefficient α was obtained as $\alpha = 0.626$. Since the coefficient α was obtained, if the phase shift $|\Delta - \Delta_d|$ can be experimentally obtained, the film thickness can be obtained by VEM.

A method for measuring $|\Delta - \Delta_d|$ is discussed below. First, P_d and A_d were measured experimentally. To obtain P_d and A_d, a disk with the polar lubricant Zdol4000 was used. Because it tends to dewet on the magnetic disk, small droplets can be observed after dewetting. The disk was set on the stage, and the angles of polarizer and analyzer were changed so that the image was in dark except for the droplets. When the intensity of the substrate reached the minimum, P_d and A_d were obtained. Besides, the intensity signals for the lubricated disk at different polarizer angles P_i (i = 0 to N-1) are measured when set the analyzer angle A was fixed at $A = A_d$. Using Eqs. (2.41), (2.42), and (2.43), the light intensity signal for the i-th polarizer angle P_i can be rewritten by

$$I_i = a_0 + a_1 \cos(2|P_i - P_d|) + a_2 \sin(2|P_i - P_d|)\,, \tag{4.5}$$

where

$$a_0 \equiv R_s I_0 \cos^2 A_d (r^2 + r_d^2)/2\,, \tag{4.6}$$

$$a_1 \equiv -2R_s I_0 \cos^2 A_d r r_d \cos(|\Delta - \Delta_d|)\,, \tag{4.7}$$

$$a_2 \equiv -2R_s I_0 \cos^2 A_d r r_d \sin(|\Delta - \Delta_d|)\,. \tag{4.8}$$

Here, we used the relationship that $2P_i+\mathit{\Delta} = 2(P_i-P_d)+(\mathit{\Delta}-\mathit{\Delta}_d)+2P_d+\mathit{\Delta}_d = 2(P_i-P_d)+(\mathit{\Delta}-\mathit{\Delta}_d)+\pi/2$. The difference in R_s between the lubricated and unlubricated disks is small. Therefore, it can be considered that the lubricated and unlubricated disks take an equal value. From Eqs. (4.7) and (4.8), we can get

$$|\mathit{\Delta} - \mathit{\Delta}_d| = \tan^{-1}\left(\frac{a_2}{a_1}\right). \tag{4.9}$$

Here, I_{mi} is the measured light intensity, and may contain measurement error and be different from the true signal I_i. Therefore, a least mean square method was used to reduce the measurement error. Mean square error between measured and true intensity signals ε is

$$\varepsilon = \sum_{0}^{N-1} (I_{mi} - I_i)^2 \ . \tag{4.10}$$

Rewriting $2|P_\mathrm{i}$-$P_\mathrm{d}|$ to be $\mathit{\Pi}_\mathrm{i}$, the conditions to minimize ε are

$$\frac{\partial \varepsilon}{\partial a_i} = 0 \qquad (i = 0, 1, 2). \tag{4.11}$$

Eq. (4.11) can be written as

$$\begin{pmatrix} 1 & \frac{1}{N}\sum_{0}^{N-1}\cos\mathit{\Pi}_i & \frac{1}{N}\sum_{0}^{N-1}\sin\mathit{\Pi}_i \\ \frac{1}{N}\sum_{0}^{N-1}\cos\mathit{\Pi}_i & \frac{1}{N}\sum_{0}^{N-1}\cos^2\mathit{\Pi}_i & \frac{1}{N}\sum_{0}^{N-1}\sin\mathit{\Pi}_i\cos\mathit{\Pi}_i \\ \frac{1}{N}\sum_{0}^{N-1}\sin\mathit{\Pi}_i & \frac{1}{N}\sum_{0}^{N-1}\sin\mathit{\Pi}_i\cos\mathit{\Pi}_i & \frac{1}{N}\sum_{0}^{N-1}\sin^2\mathit{\Pi}_i \end{pmatrix} \begin{pmatrix} a_0 \\ a_1 \\ a_2 \end{pmatrix} = \begin{pmatrix} \frac{1}{N}\sum_{0}^{N-1} I_{mi} \\ \frac{1}{N}\sum_{0}^{N-1} I_{mi}\cos\mathit{\Pi}_i \\ \frac{1}{N}\sum_{0}^{N-1} I_{mi}\sin\mathit{\Pi}_i \end{pmatrix}. \tag{4.12}$$

P_i, P_d and I_mi were measured for the sample, then, the coefficients a_1 and a_2 were obtained and the phase shift $|\mathit{\Delta}$-$\mathit{\Delta}_\mathrm{d}|$ was determined by using Eq. (4.9)

4.3.3 Experimental Procedure

In order to obtain the thickness from the captured image, it is required to clarify the relationship between film thickness and light intensity in the VEM. The theoretical relationships between the angles of polarization devices and the film thickness as shown in Fig. 4.9 should be proved expermentally. Therefore, the relationship between film thickness and light intensity were experimentally obtained at various angles of polarization devices. To develop the calibration by phase shift method, the polarizer is also required to be rotated for different ligjt intensity of the image. Therefore, they followed almost the same experimental procedures.

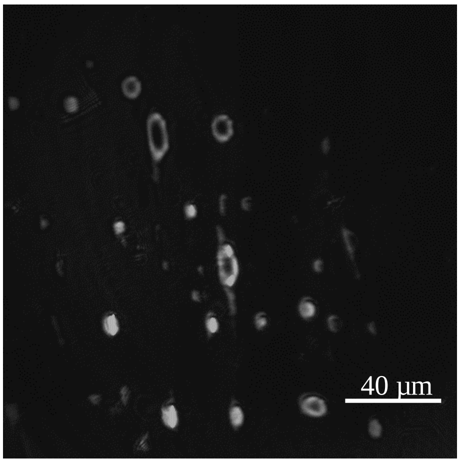

Fig. 4.10 Dewetted image taken by VEM for null condition.

Firstly, the null condition should be determined, because the adjustment of the analyzer was required in this condition in the experiment. Here, the polar lubricant Zdol4000 was used. It tends to dewet on the magnetic disk. A dewetted disk which had small droplets on was used for the adjustment. The disk was set on the stage, and the angles of polarizer and analyzer were changed so that the image was in dark except for the droplet. When the intensity of the substrate reached the minimum, the null condition was obtained, as shown in Fig. 4.10.

Here, I used dewetted disk with Zdol4000 instead of unlubricated disk. The reason was as follows: one is that, null condition is required to obtain the analyzer angle A_d in this study. The simulated result of the I-h curve at different analyzer angles is shown in Fig. 4.11. Comparing the intensities at $h = 0$ (unlubricated disk) and $h = 2$ nm (2 nm-thick-film-covered disk), we can find that both of the intensities of unlubricated disk and lubricated disk reach the minimum at the null condition ($A = 53$ deg). It indicates the dewetted disk can be used to find the null condition although the dark area is covered with monolayer lubricant. The other reason is that light intensity was not so sensitive in the experiment to the analyzer angle when it was dark. On the other hand, the relative intensity difference between the droplets and the monolayer lubricant changed more. Here, relative intensity difference between the droplets and the monolayer lubricant is defined as the ratio of intensity difference between the droplets and the monolayer lubricant and the intensity of the monolayer lubricant. It can also be proved theoretically. In Fig. 4.11, consider droplets have a thickness of 10 nm (It may much more than 10 nm actually), and the monolayer lubricant is 2 nm-thick. Comparing the relative intensity difference between the droplets and the monolayer lubricant for $A = 51$, 52, 53, 54, 55 deg, the value is 2.4, 7.8, 19, 7.6 and 2.6, respectively. It reaches the maximum when $A = 53$ deg, which is the null condition. Therefore, it is easy to obtain the null condition by measuring the relative intensity difference, since the relative intensity difference reached maximum, the null condition could be obtained.

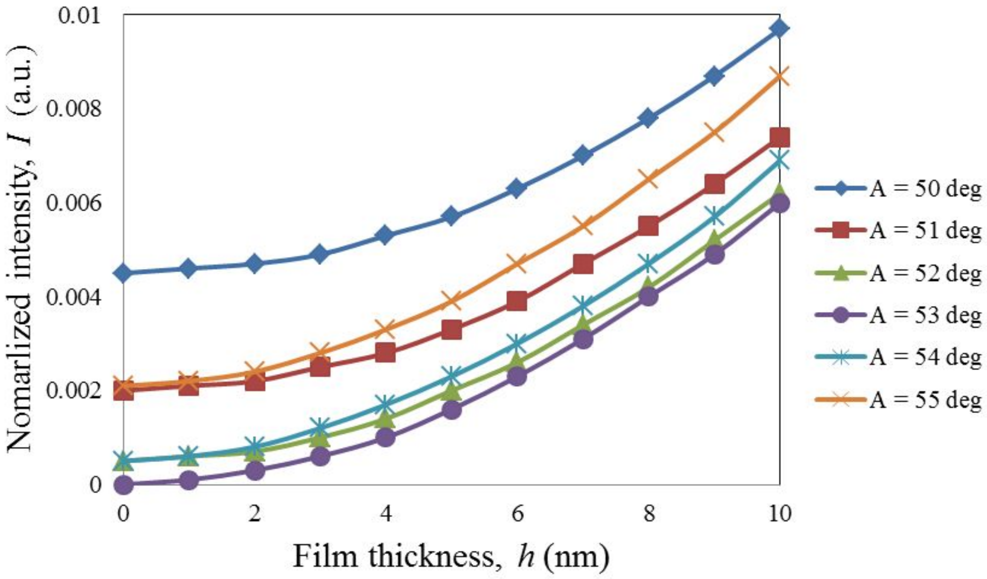

Fig. 4.11 Simulated relationships between intensity and thickness for different analyzer angles *A* (The polarizer angle at the null condition, A_d is 53 deg).

The experiments were performed according to the following steps.

1. Z03 lubricant with HFE-7200 was diluted. And the mixture was stirred for about 20 minutes. The concentrations of the solution were 0.2% and 0.6% depending on the target film thickness.
2. The amplitude ratio Ψ and phase difference Δ of the magnetic disk without the lubricant were measured with a scanning ellipsometer, and refractive index n and extinction coefficient k of the magnetic disk were obtained. In addition, the laser spot was scanned on the disk in the radial direction (r = 24 to 32 mm). The scan step was 0.05 mm, and sampling points were 161 points. The thickness was obtained as an average value for four times measurement at each measurement point.
3. Using the solution prepared at Step 1, the lubricant was applied to disks mentioned in Step 2 by a dip coating method. The removal speed was adjusted between 0.5 ~ 2.6 mm / sec,

depending on the target film thickness, and the lubricant film was partially coated. The length of film covered region in the radial direction was about 30 mm.

4. The thickness of the coated film was measured by the ellipsometer immediately after the coating. The scan range was the same as Step 2.
5. After the measurement of film thickness in Step 4, the sample was promptly set to VEM, and lubricant film image was taken. The camera settings were exposure time 0.10 sec, gain 2, gamma 1, pixel size 512 × 512, binning 1 × 1, on-chip charge multiplication gain 2800.
6. Move the sample stage so that the lubricant uncovered region could be observed by the VEM, and image was taken with the camera settings the same as in Step 5.
7. The polarizer was rotated with a step of 5 deg and 10 steps, and then the same peocesses was conducted as described in Step 5 and 6.
8. The light intensities of the films for different thicknesses at different angles of polarizer were measured, and the relationships between light intensity and thickness at different polarizer angles were obtained, and the the angle of polarizer could be determined so that the light intensity is propotional to the thickness. And the phase shift method could be achieved by recording the light intensity at different polarizer angles.

4.3.4 Results and Discussion

a) Conversion intensity to thickness

Figure 4.12 shows the result of the polarizer adjustment so that the intensity difference I-I_d is proportional to the thickness h. In this experiment, the nonpolar lubricant was used and the thickness was measured by the phase shift method mentioned above. The intensity was also 10-time averaged. The error bar expresses the standard deviation of each measured intensity. The measured relationship between the light intensity and film thickness as a function of polarizer angle P is shown. In the figure, the intensity difference between lubricated and unlubricated disks is shown, where I and I_d are the intensities of the lubricated and unlubricated disks, respectively. Here, the analyzer was set at 34.2 deg, where the null condition was satisfied when P = 52 deg. As the simulation predicted in Fig. 4.9, the different polarizer angles produced the different dependency. This indicates that the polarizer angle can be selected so that the intensity difference I-I_d is proportional to h (P = 86 deg). In Fig. 4.13, the data at P = 86 deg in Fig. 4.12 are plotted. The error bar expresses the standard deviation of each measured intensity. Using this linear relationship, the light intensity can be directly converted into film thickness in our VEM. The polarizer angle when I-I_d was proportional to h is different from the theoretical angle in Fig. 4.9. The reason is considered to be that the light beam was reflected at the optical devices such as beam splitters (Fig. 4.7), and the polarization state was changed after this additional reflection. Similar to the derivation of Eq. (2.42), the null condition can be obtained as

$$2P_d + \Delta_d + \Delta_{\mathrm{d}}' = \frac{\pi}{2}, \tag{4.13}$$

Where Δ_d’ is the additional phase change. Δ_d is a important parameter for thickness determination as show in Eq. (4.4). Although the polarization state changes due to Δ_d’, the thickness determination may not be affected, since the effect of Δ_d’ exists in both Δ and Δ_d and is canceled by the subtraction in Eq. (4.4).The typical noise level was about 0.8 nm, which was obtained from the observed image for the film with a thickness h of 2.7 nm (I-I_d = 763, σ = 226).

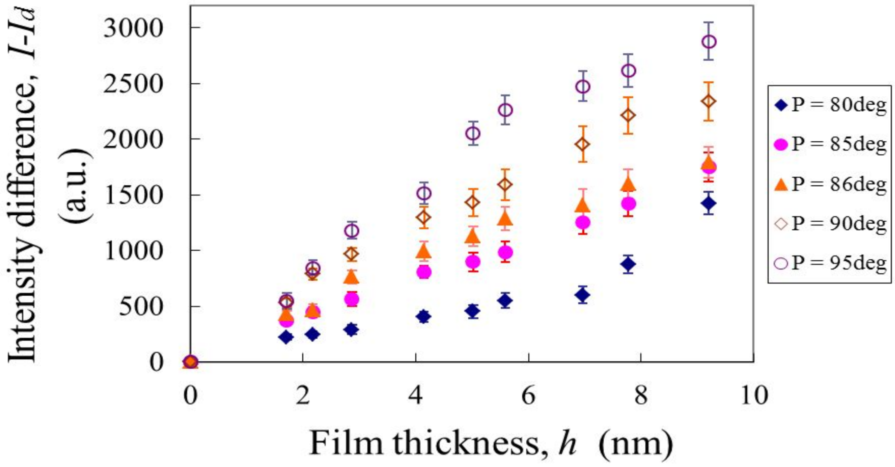

Fig. 4.12 Experimental relationships between intensity and thickness for different polarizer angles *P*.

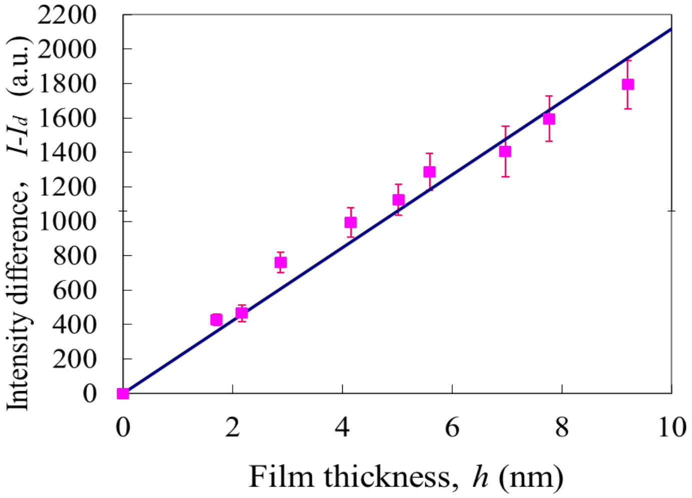

Fig. 4.13 Relationship between intensity and thickness at *P* = 86 deg.

b) Thickness determination by phase shift method

In Fig. 4.14, the thickness obtained by the VEM using the phase shift method was compared with that by an ellipsometer. In this experiment, the nonpolar lubricant was used. In the phase shift method, the polarizer angles were changed from 62 to 102 deg at an interval of 5 deg. In this experiment, the polarizer was manually rotated. This procedure required a long time and the large interval could cause the measurement error due to the light intensity fluctuation. Therefore, 10-time averaged values were used as the intensity. The error bar expresses the standard deviation of each measured thickness by VEM. The solid line is a straight line with a slope of one. And this result indicates the measurements by our method agree well with those by the ellipsometer. The measurement error was 0.3 nm, whick was described by standard deviation from the straight line. This shows that the phase shift method can determine the thickness at an accuracy of about 0.3 nm. Thus, using the phase shift method, the lubricant film thickness can be measured by our VEM itself, without any other instruments.

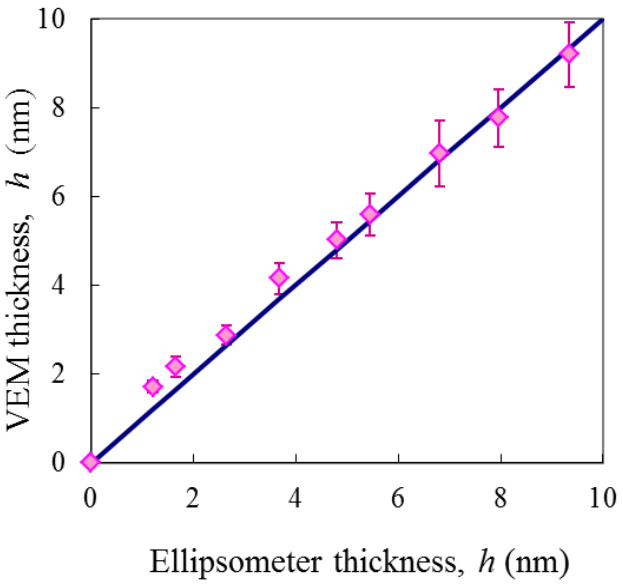

Fig. 4.14 Thicknesses comparison between obtained by VEM and by an ellipsometer.

In addition, the magnetic disks have some fluctuations of the refractive index *n* and extinction coefficient *k*, and those effects on the thickness measurement should be discussed. In this experiment, we obtained the thickness resolution of 0.2 nm using 2.2 nm-thick lubricant film, which means the noise was about 15% of the signal. And we used an ellipsometer to measure the *n* and *k* of the samples, the fluctuations defined as standard deviation were about 0.01 for both *n* and *k* for 80 sampling points at distance of 8 mm, which means the fluctuations of *n* and *k* were less than 1%. Although the VEM and ellipsometer have different lateral resolutions, the noise level of VEM is much higher than the *n* and *k* errors of ellipsometer. Therefore, we might consider that the noise caused by the optical system was much larger than the *n* and *k* fluctuations.

4.4 Lateral Resolution

An ideal point object for characterization of optical imaging system, due to the diffraction limit, can not be imaged as the ideal image point, but a Fraunhofer diffraction image. Therefore, each point of the real object is imaged as a diffuse light spot, and if the two diffuse spots are too close, it difficult to distinguish the two points. Lateral resolution depends on the distance between two distinguishable light points. However, it is difficult to obtain lateral resolution from measurement of the distance between two distinguishable light points, since the ideal point light source can not be found, experimentally. Therefore, in the actual measurement, modulation transfer function (MTF) is usually used to evaluate the lateral resolution for an optical system. MTF is the magnitude response of the optical system to sinusoids of different spatial frequencies. It is much easier to creat a sinewave input than point light source input, that is why MTF testing is more common. Here, the spatial frequency is defined as the inverse of the spatial period of the sinusoid. In our experiment, the MTF was analyzed using a 1951-USAF-test pattern. The image of the test pattern taken by the VEM is shown in Fig. 4.15. The *y*-axis in the figure was the direction of the incident plane. In the test pattern, a chromium film pattern of three equal-width black line was deposited on a glass substrate.

A unit of lp / mm (line pairs per mm) was used to express this interval, which corresponds to spatial frequency per 1 mm. The partterns in the horizontal direction were used to evaluate the vertical resolution limit, as well as the vertical bars were used to evaluate the horizontal resolution limit of the imaging optical system. Numbers on the test pattern indicates the target group number. The three-bar width and spacing becomes narrower as the number is greater. Within each group, there are six kinds of different widths of the three-bar patterns, which are called elements. Table 4.3 shows the relationship between the group and elements of spatial frequency test targets used in this study. In this experiment, the polarization devices were removed because the patterns were made of chromium film on a glass substrate and could be imaged without the polarization devices.

Figure 4.15 shows that the finest three-bar (+9-3) can be resolved, which corresponds to the 0.78 μm of resolution. Therefore, we can not obtained the lateral resolution directly, and have to analyze the contrast as a characterization of the optical system. Contrast is the difference in luminance that makes an object distinguishable. Contrast C is defined by the following equation using the maximum and minimum of light intensity in the image $I_{\max}$ and $I_{\min}$,

$$C = \frac{I_{\max} - I_{\min}}{I_{\max} + I_{\min}} . \tag{4.14}$$

Generally, the contrast C of output of an optical system is smaller than that of the input in amplitude, and the change is evaluated by the ratio between the contrast of the output and the input intensity in all spatial frequency. This is MTF. However, to determine the MTF, it requires the input light to be a sinewave, which is difficult to achieve actually. For the square wave signal of the test pattern image, contrast transfer function (CTF) was obtained instead.

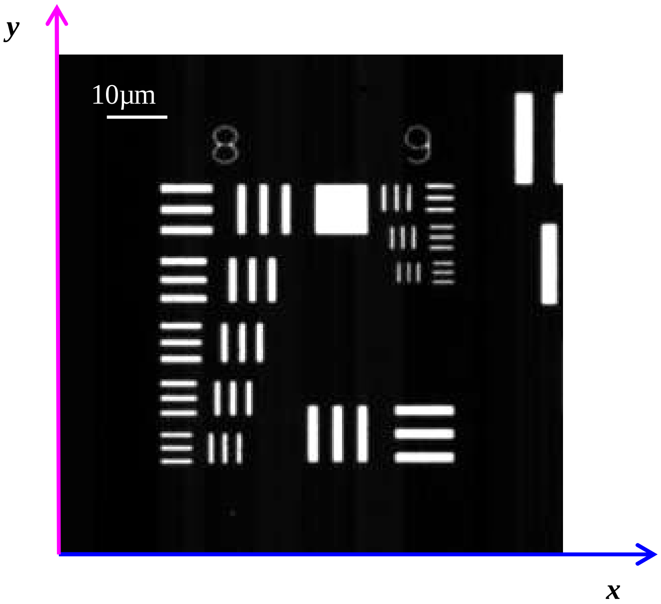

Fig. 4.15 1951-USAF-test pattern taken by the VEM without the polarization elements.

Table 4.3 Number of Line Pairs / mm in USAF Resolving Power Test Target 1951.

	Group number									
Element	+0	+1	+2	+3	+4	+5	+6	+7	+8	+9
1	1.00	2.00	4.00	8.00	16.00	32.0	64.0	128.0	256.0	512.0
2	1.12	2.24	4.49	8.98	17.95	36.0	71.8	144.0	287.0	575.0
3	1.26	2.52	5.04	10.10	20.16	40.3	80.6	161.0	323.0	645.0
4	1.41	2.83	5.66	11.30	22.62	45.3	90.5	181.0	362.0	---
5	1.59	3.17	6.35	12.70	25.39	50.8	102.0	203.0	406.0	---
6	1.78	3.56	7.13	14.30	28.50	57.0	114.0	228.0	456.0	---

First, the contrast of input intensity C_i should be obtained. By convention, the CTF is normalized to unity at zero spatial frequency. For low spatial frequencies, the CTF is close to 1 (or 100%) and generally falls as the spatial frequency increases until it reaches zero. Therefore, in the experiment, move the test target so that the whole field of view of VEM is the image of the chromium film to obtain the maximum of input $I_{i\text{-max}}$ as an average intensity value of the whole image, and move the test target so that the whole field of view is the image of the glass substrate to obtain the minimum of input $I_{\text{i-min}}$ as an average intensity value of the whole image. Therefore, C_i was obtained.

Then, the contrasts of the output for each frequency C_o were calculated. Average the intensity of the three-bar patterns in direction that parrallel to the bars, as shown in Fig. 4.16(42), the maximum and minimum intentisy $I_{\text{o-max}}$ and $I_{\text{o-min}}$ for each three-bar patterns could be found from these average values. Then C_o was obtained. CTF = C_o/C_i.

The CTF was converted to MTF using an approximate conversion (43)

$$MTF(f) = \frac{\pi}{4}\left[CTF(f) + \frac{1}{3}CTF(3f) - \frac{1}{5}CTF(5f) + \frac{1}{7}CTF(7f) - \cdots\right], \tag{4.15}$$

where f is the spatial frequency. Here, I used line pair per mm of each target group approximation of Eq. (4.15).

Generally, it is considered that small features can be resolved when the intensity of MTF is greater than 0.1 for the imaging system. The human eye can not identify the density differences in the MTF of 0.1. Therefore, I obtained the lateral resolution from the spatial frequency at the intensity of MTF = 0.1. The measured MTF for the test pattern are shown in Fig. 4.17. The hollow and solid triangles are used to describe the MTF for the patterns parallel to the incident plane and perpendicular to the incident plane, respectively. The minimum size of patterns on the test target is 0.78 µm, therefore the curves were extrapolated as an approximate line by using a least square method. Using the criteria of the intensity of MTF = 0.1, the estimated resolutions were about 0.55 µm and 0.48 µm for the patterns parallel to the incident plane and perpendicular to the incident plane, respectively. This means the lateral resolution for the directions vertical to the incident plane and parallel to the incident plane were about 0.55 µm and 0.48 µm, respectively. This indicates that our microscope almost achieved a diffraction limited lateral resolution of 0.41 µm as decribed in Section

4.2.3, which is principle limit in optical microscopes. In addition, the oblique illumination does not significantly affect on the image formation because the imaging characteristics are almost same in the parallel and perpendicular directions to the incident plane.

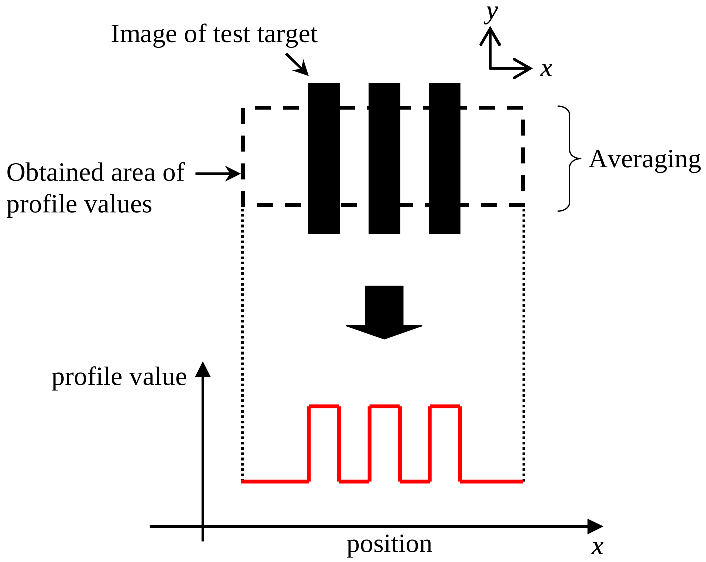

Fig. 4.16 A method for obtaining profile values of the test target image.

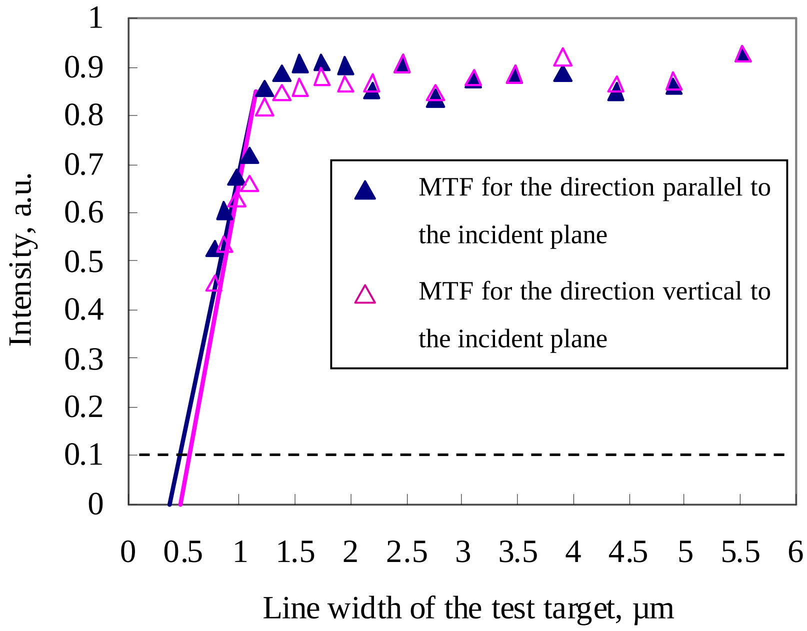

Fig. 4.17 MTF of the VEM obtained from the observation of the test pattern.

4.5 Summary

A VEM for the real-time observation of thin liquid lubricant films was investigated. The developed VEM shows that the vertical setup of the objective lens can provide about 0.5 μm lateral resolution. Moreover, conversion of the light intensity to the film thickness was investigated. The phase shift method can determine the thickness with an error of about 0.3 nm. This shows that other thickness measurement devices such as ellipsometer are unnecessary. In addition, the polarizer setting so that the intensity difference I-I_d is proportional to h can provide the direct conversion from I to h, which enables real-time observation. From these experiments, the achieved thickness resolution was 0.8 nm. Since the thickness of the lubricant film for current HDDs is 1-2 nm, it is difficult to observe the lubricant films by our current microscope due to the low thickness resolution. However, this method has the potential of the thickness resolution of 0.1 nm as usual ellipsometers do. If the signal to noise ratio of the observed image is increased, the thickness resolution can be improved, which will be described in the next chapter.

Chapter 5 Improvement of Thickness Resolution

5.1 Introduction

In the last chapter, the feasibility of VEM for thin lubricant films was confirmed, as well as the thickness determination was demonstrated. However, the thickness resolution was about 0.8 nm considering 1-2 nm thick lubricant film on magnetic disk in HDDs, the improvement of the thickness resolution is necessary. In this chapter, the design principle of the VEM, especially the methods for improvement of thickness resolution are presented.

5.2 Definition of Thickness Resolution

In order to investigate the methods for improving the thickness resolution, it is essential to consider how the thickness resolution should be defined. In practice, due to the noise of the imaging system, the intensity on CCD does not have uniform distribution, even though the sample film has a uniform thickness. This causes the error of thickness analysis for VEM. Therefore, we used signal to noise ratio (SNR) to describe the thickness resolution. As shown in Fig. 5.1, I and I_d are the mean values of the light intensities in the lubricant covered and uncovered regions respectively, and σ is the standard deviation of the light intensity in the lubricant covered region. The intensity difference between lubricant covered and uncovered regions $I-I_d$ is the signal S, and the standard deviation σ is the noise N. Therefore, the SNR can be given by

$$SNR = \frac{I - I_d}{\sigma}. \tag{5.1}$$

And the thickness resolution h_m, which is defined as the thickness when SNR = 1, can be expressed by

$$h_m = \frac{h}{SNR}. \tag{5.2}$$

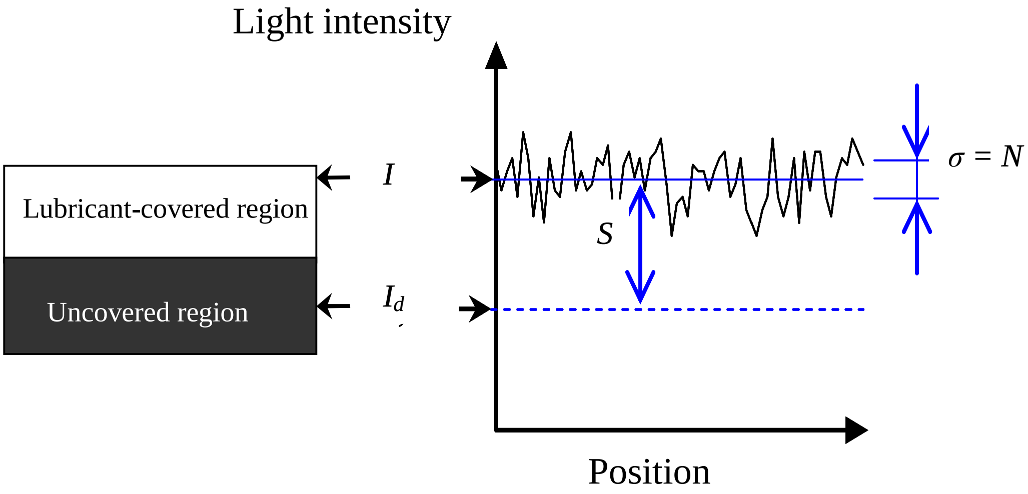

Fig. 5.1 Definition of SNR of lubricant image.

The equation indicates that higher SNR is required to improve the thickness resolution, and signal enhancement and noise suppression is required.

5.3 Improvement of Ellipsometric Signal

5.3.1 Improvement of Signal with a High Power Light Source

High power light source can increase the light intensity; however, the shot-noise is also increased. In light detectors, the signal is generally proportional to the light intensity whereas the noise is proportional to the square root of the light intensity when shot-noise is dominant. Therefore, the SNR is proportional to the square root of the light intensity (44). This relation was valid in the VEM Since a CCD camera was used as the light detector and the light intensity was rather large. This means that the higher power of the light source can improve the thickness resolution.

5.3.2 Improvement of Signal by Optimization of Incident Angle

Since intensity difference between lubricant covered and uncovered regions I-I_d is defined as the signal, in order to compare the signal of different situations, a normalized ellipsometric signal was used in this study. The normalized ellipsometric signal I_n here is defined by

$$I_n = \frac{I - I_d}{I_d} . \tag{5.3}$$

The ellipsometric signal depends on the incident angle θ because the signal is determined by the complex reflectivity of the sample, which changes according to the incident angle. Moreover, the signal intensity of ellipsometric microscope I was given by Eq. (2.41). The normalized intensity was calculated by using Eqs. (5.3) and (2.41). The light intensity signal I is determined by the ellipsometric parameters R_s, r and Δ, and these parameters are the functions of N, d, λ, θ. As N, d, and λ are determined by the sample, only θ is an adjustable parameter for the improvement of ellipsometric signal.

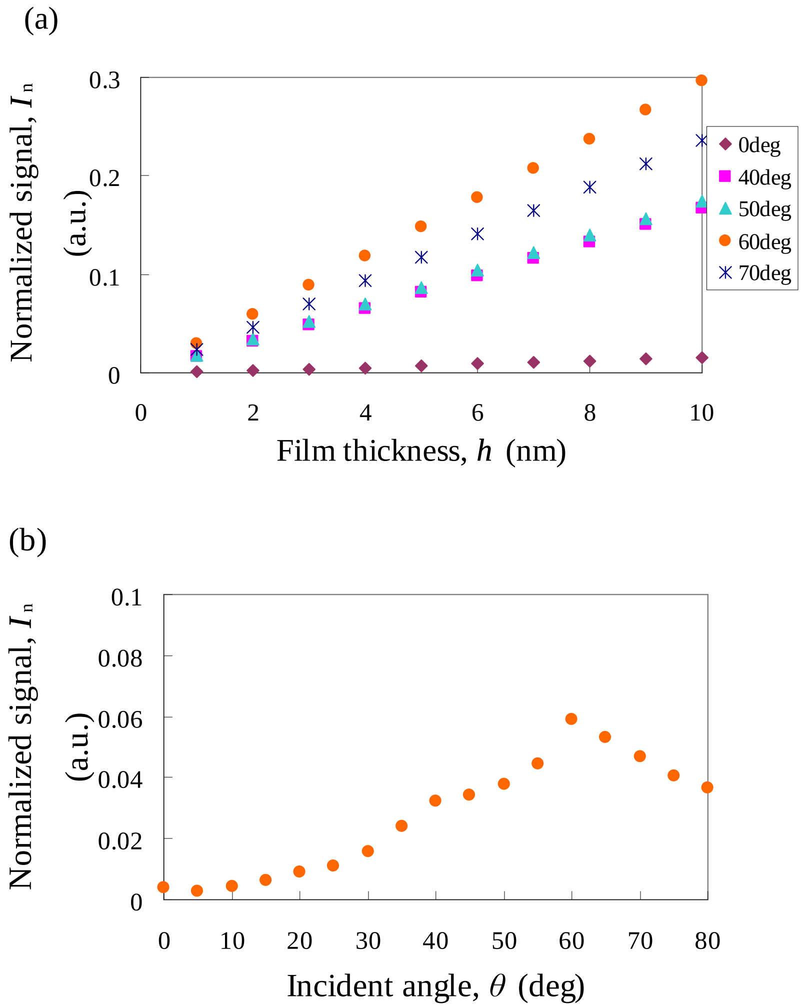

Fig. 5.2 Simulated relationship between normalized signal I_n and thickness h for different incident angles: (a) relationship between the contrast ratio and thickness after adjustment of polarizer angle so that the intensity is proportional to the thickness for each incident angle for different incident angles; (b) relationship for incident angle θ and normalized signal I_n for a 2 nm-thick lubricant film.

As described in Chapter 4, in the VEM, the polarizer is adjusted so that the light intensity signal I

is proportional to the film thickness *h* in order to simplify conversion from the light intensity to the thickness. The simulated relationships between normalized signal I_n and film thickness *h* for different incident angles is shown in Fig. 5.2 (a). The model used in the simulation is the same as that in the simulation in Section 2.2.1.

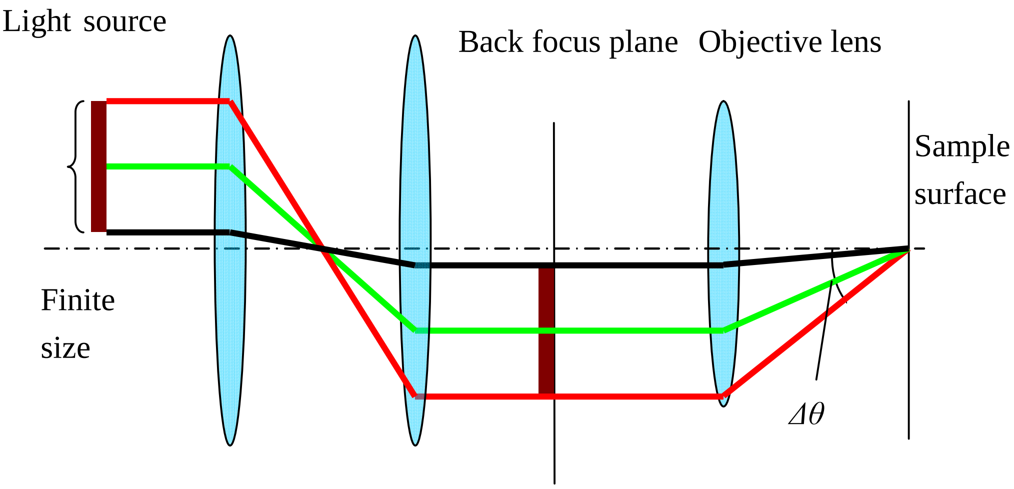

Fig. 5.3 Illumination system for actual setup.

In the simulation, shown in Fig. 5.2 (a), the compensator and analyzer were set at null condition, where the unlubricated disk takes the minimum intensity. The polarizer was adjusted so that the intensity was proportional to the thickness for each incident angle. Figure 5.2 (b) shows the relationship between the normalized intensity signal and incident angle at a thickness of 2 nm. From these results, it is concluded that the incident angle affects the normalized intensity signal significantly, and it reaches the maximum when the incident angle θ is 60 deg.

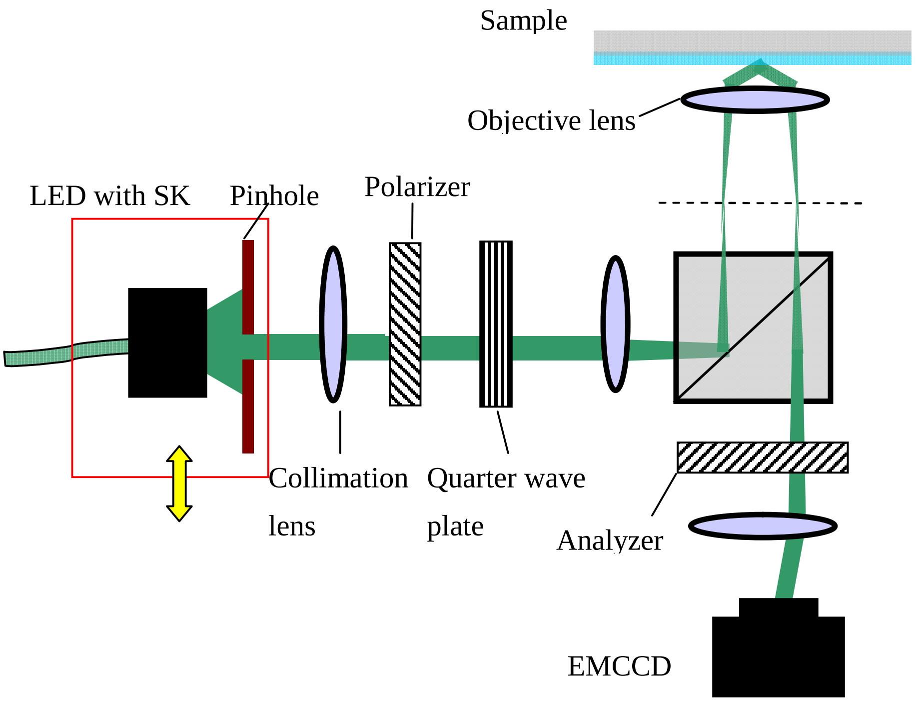

Fig. 5.4 Setup of the optical system with a pinhole for controlling the width of the incident angle.

Moreover, the results shown in Fig. 5.2 indicate an additional requirement for an actual setup of VEM. The light source is not a point in an actual setup, which causes that the incident angle may have a width of $\Delta\theta$ (Fig. 5.3), which affects the ellipsometric intensity, as shown in Fig 5.2(b). So both θ and $\Delta\theta$ should be controlled. Thus, in the optical system of VEM, a pinhole was added behind the light source for controlling the width of the incident angles $\Delta\theta$ as shown in Fig. 5.4.

5.3.3 Improvement of Signal by Use of Short Wavelength

In addition, some other attempts for thickness resolution impromvement have been done for a further experiment, such as the relationship between the wavelength λ of the light source and the ellipsometric signal.

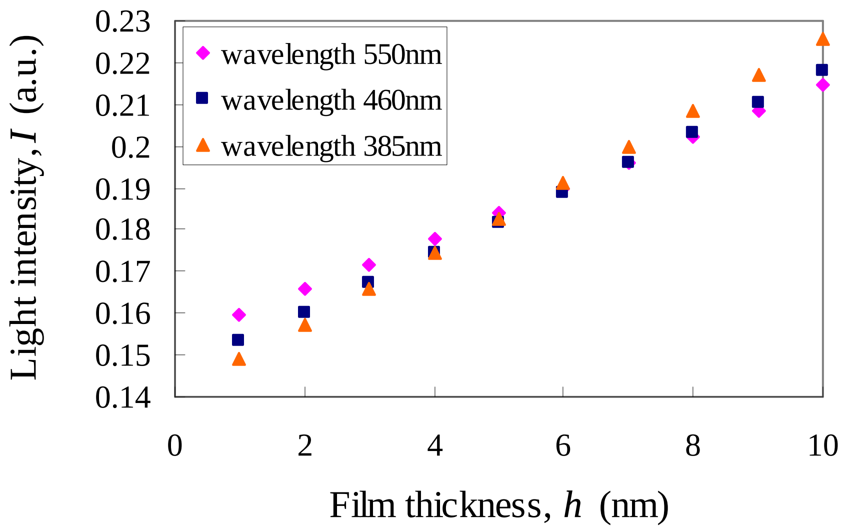

Fig. 5.5 Simulated relationships between intensity and thickness for different wavelength of the light source.

Figure 5.5 shows the simulated relationships between light intensity *I* and film thickness *h* for different wavelength of the incident light. The polarizer and analyzer angles were adjusted so that the light intensity *I* was proportional to the thickness *h* in this calculaiton. The slope of this *I*-*h* curve increases when the wavelength decreases. In other words, shorter wavelength makes the sensitivity to the thickness larger. In addition, we added the simulation of the slope of *I*-*h* curve for different wavelength as shown in Fig. 5.6. This demonstrates that the slope or sensitivity decreases by increasing the wavelength of light source. If the noises for each wavelength have the same level, high sensitivity can lead to a high thickness resolution. The results of noises of light sources of different wavelengths are shown in Table 5.1. The sample used in the test was unlubricated disk and the light intensities were adjusted closer for comparison. The experimental data indicates that the light sources have a similar level of noise. Therefore, choosing the light source with shorter wavelength is a way to improve the thickness resolution.

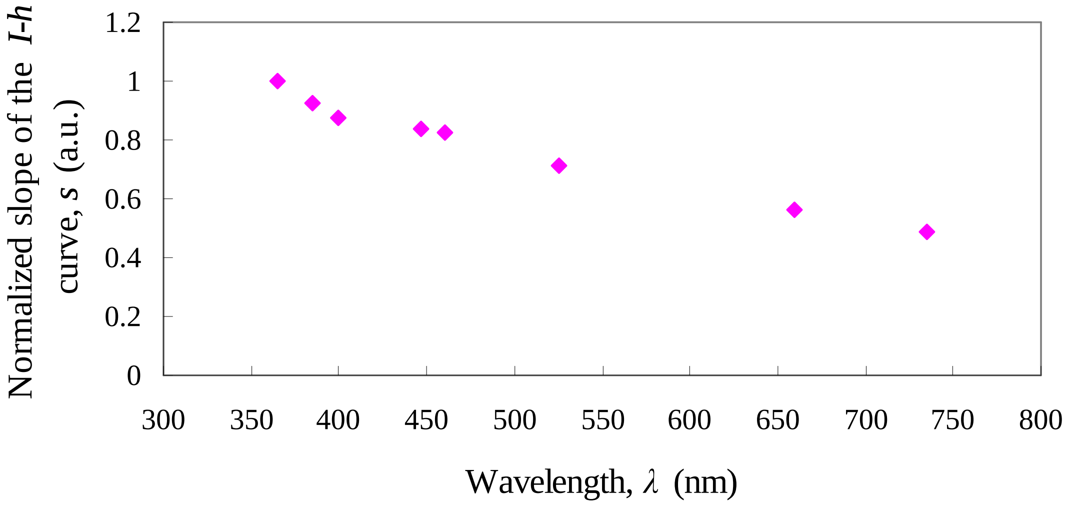

Fig. 5.6 Simulated relationship between the slope of the *I-h* curve, *s* and wavelength of light source *λ*.

Table 5.1 Noises of light source for different wavelengths.

Wavelength λ, nm	385	460	525
Light intensity I_d	11439	12585	12003
Standard deviation σ	202	221	212

5.4 Suppression of Noise

Suppression of noise is important to improve SNR. Here, the noise suppression of VEM is discussed.

As mentioned in Section 4.2.2, in the VEM, coherent noise is important in addition to shot noise generated by the detector. As mentioned above, the shot noise increases with the light intensity increasing, however it does not decrease the SNR, because the signal increases more rapidly than the noise when the light intensity increases. Thus, the effect of shot noise can be suppressed by the increase of the light source power. On the other hand, since the coherent noise is proportional to the light intensity, a different approach is needed for the suppression of the coherent noise.

As shown in Fig. 4.3, coherence noises appear as dark-bright fringe images in VEM. Coherence is a property of waves that enables interference, which includes temporal and spatial coherence. When we discuss the coherent noises, the temporal coherent noise and spatial coherent noise must be separately expressed.

5.4.1 Suppression of Temporal Coherence Noises

Temporal coherence is the property that the phase difference between the lights emitted at different times does not change with time. If the coherent lights passing through the different distance paths arrive at the same point, interference fringes are generated. Temporal coherence is usually characterized by coherent length. Coherence length l_c is the maximum optical path difference when interference can occur. It is given by

$$l_c = \frac{\lambda^2}{\Delta\lambda}. \tag{5.4}$$

where λ and $\Delta\lambda$ are the wavelength and width of the wavelength of the light source, respectively. The smaller $\Delta\lambda$ is, and the temporal coherence noises occur more clearly. For the coherence length is larger than 100 m of He-Ne lasers with $\Delta\lambda$ of 10^{-6}~10^{-9} nm, and the lasers tend to cause interference due to the high temporal coherence. To decrease the temporal coherent noise, a light source with large wavelength width is necessary. In VEM, the temporal coherence is mainly caused by the reflection in the optical devices, so when the minimum of the distance between two optical devices is larger than l_c, the temporal coherent noise can be reduced. In VEM, the objective lenses have the smallest distance of 1 mm order, so the light source with l_c smaller than 1 mm is needed.

5.4.2 Suppression of Spatial Coherence Noises

Spatial coherence is the property that the phase difference between the lights emitted at different positions does not change with time. Usually, distant points have poorer phase correlation. Therefore, the larger light source can decrease the spatial coherent noise. In the VEM, as shown in Fig. 5.4, the area of light source was adjusted by setting the pinhole behind the light source and the light passing through the pinhole was converted to the parallel beam by the collimation lens. The coherence is evaluated by the degree of coherence $|\mu_{12}|$, which corresponds to the visibility of interference fringes. The lights are coherent when $|\mu_{12}| = 1$, and incoherent when $|\mu_{12}| = 0$. The average degree of coherence between the light passing through the center of the optical axis and all the lights passing through the pinhole is given by (27)

$$\left\langle |\mu_{12}| \right\rangle = \frac{1}{\pi a^2}\int_0^a 2\pi \left| \frac{2J_1\left(\frac{2\pi R}{\lambda f} r\right)}{\frac{2\pi R}{\lambda f} r} \right| r dr \tag{5.5}$$

where a, R and f are the radius of the pinhole, radius and focal length of the collimation lens, respectively. $J_1(x)$ is the first Bessel function of the first kind. Figure 5.7 shows the calculated relationship between the pinhole diameters a and the average degree of coherence $<|\mu_{12}|>$. Here, R = 27 mm, f = 60 mm, and λ = 512 nm, which are the values in the experimental setup. The estimation indicates that the larger pinhole decreases the degree of coherence. The degree of coherence decreases down to 1/10 at about a diameter of 28 μm and 1/100 at 100 μm. This means suppression of the spatial coherence noise requires the pinhole diameter of larger than around 100 μm.

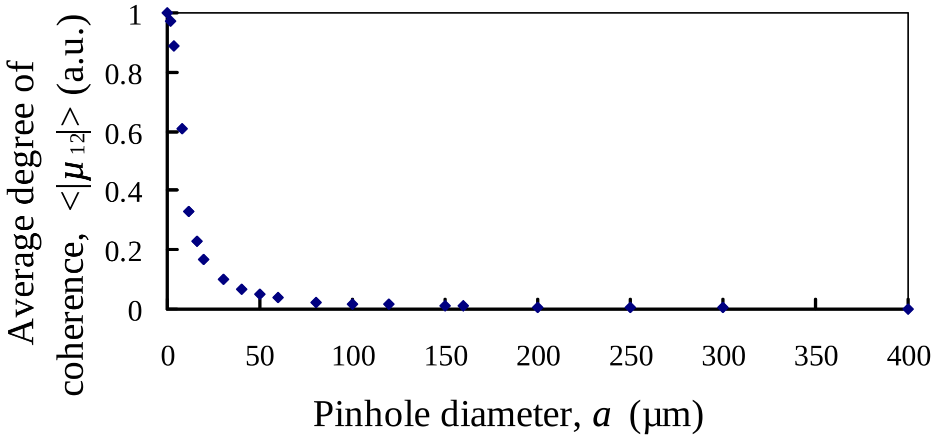

Fig. 5.7 Calculated relationship between the pinhole diameter *a* and the average degree of coherence $<|\mu_{12}|>$.

5.5 Experimental Verification

As described in Sections 5.3 and 5.4, the incident angle and pinhole size were found to be important factors to improve SNR of VEM. Here, the theoretical prediction was experimentally verified.

5.5.1 Improvement of Ellipsometric Signal

For our setup, the incident angle as well as the pinhole size may affect the ellipsometric contrast, so we compared the normalized intensities of lubricated and unlubricated regions on the disk at different incident angles and different pinholes. A 2.7 nm-thick nonpolar lubricant film Z03 on the magnetic disk was used as the sample. The application method was the same as that explained in Section 4.4, and the sample disks used in this experiment were longitudinal disks. The polarizer, compensator and analyzer were set so that the intensity was proportional to the thickness for each incident angle, as shown in Fig. 5.8 (a). The relationship between the normalized intensities and incident angle is shown in Fig. 5.8 (b). The error bar expresses the standard deviation of each measured intensity. The normalized intensities reached the maximum at the incident angle θ of about 60 deg for all the pinholes, which well matched the theoretical results as shown in Fig. 5.2 (b). As explained in Section 5.3.2, the pinhole size may affect the signal by mixing the signals at different incident angles. For different pinholes, the normalized intensities changed not much except for 1 mm-diameter pinhole and non-pinhole conditions, and the normalized intensity I_n decreased significantly at the last two conditions. The larger pinhole causes the larger range of the incident angles and the normalized intensity I_n is smaller because it is averaged over the larger ranges. In the experiment, some other factors may affect the result, for example, the noise influence. When the pinhole is small, such as 20, 100 and 200 μm-diameter pinholes, the noises may be too large to lead to the distortion of I_n. Therefore, the difference of I_n is not clear between the small pinholes, whereas, clear for 1-mm-diameter pinhole and non-pinhole conditions, due to the smaller noises. These results indicate that the larger pinhole decrease the signal. This agrees with the theoretical prediction in Section 5.3.2.

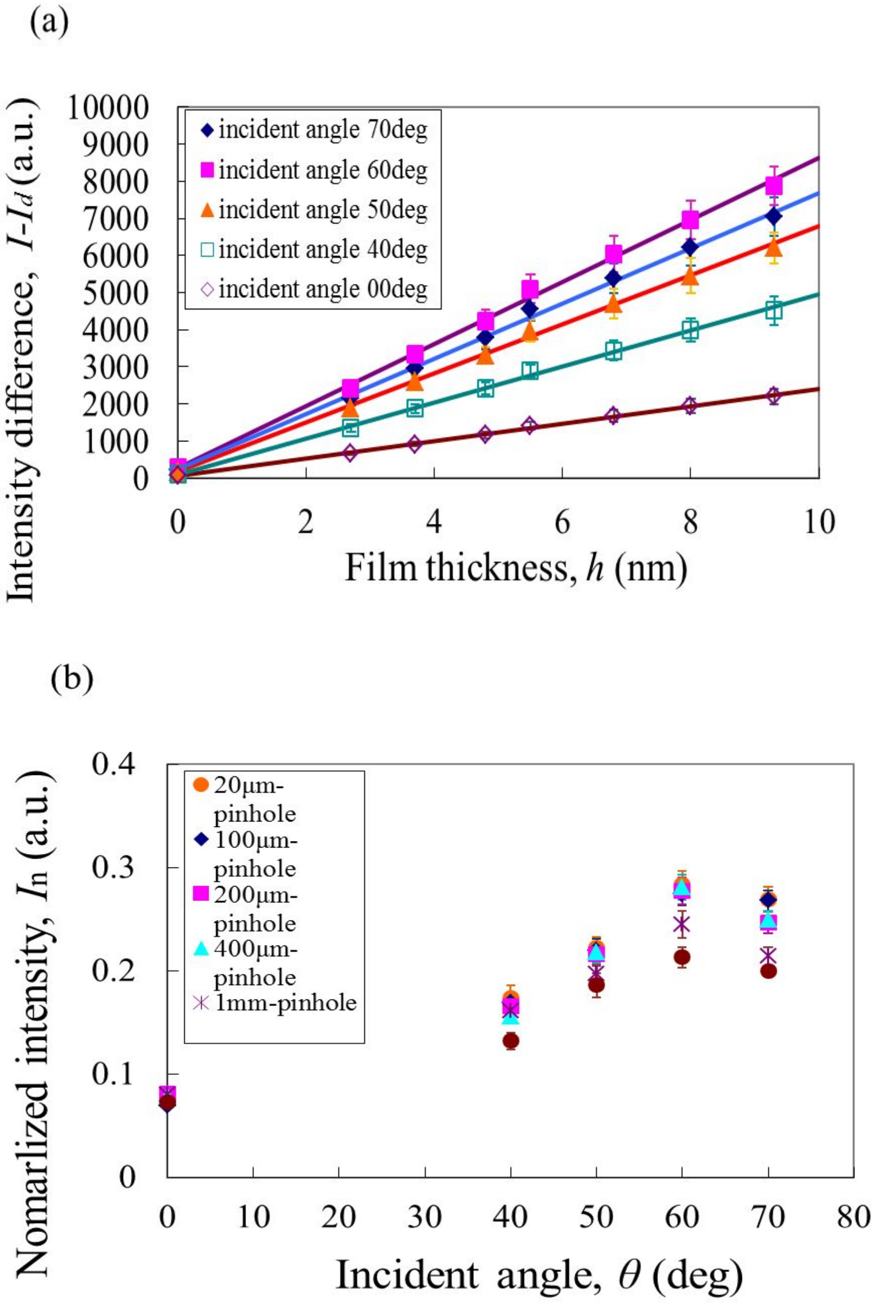

Fig. 5.8 Experimental relationships between intensity and thickness: (a) The polarizer was adjusted so that I-I_d is proportional to h for different incident angles when the diameter of pinhole is 400 μm; (b) Relationship between the incident angle and normalized intensity, normalized intensity of 2.7 nm-thick lubricant image at different pinhole sizes and different incident angles.

5.5.2 Suppression of Noise

We also compared the noise level at different incident angles with different pinholes. The relationship between noise and incident angle is shown in Table 5.1. We used the standard deviation of the light intensity of the image to define the noise level. In this experiment, the 400-μm-diameter pinhole was used, and a 1951-USAF-resolution-test-chart was used as the sample. The laser power was adjusted so that the light intensities on the CCD were equal for the different incident angles. Table 5.2 indicates that effect of the incident angle on the noise is not significant. Figure 5.9 shows the noise images on test pattern for different pinhole diameters when the incident angle was 60 deg. The coherent noises, which appeared as interference fringes, were clearly observed when the diameter of pinhole was 20 μm. The larger pinhole reduced the coherent noises, which corresponded to the theory as shown in Fig. 5.7. However another noise was observed in the images of 100- and 200-μm-pinhole, which was considered to be caused by the pinhole camera effect. Since the speckle killer is composed by a bundle of optical fibers, if the pinhole is small enough, it is seems as a camera, the bundle of fibers can be imaged on the other side of the pinhole. When the diameter of pinhole was larger than 400 μm, the pinhole-camera-image was obscure, because the larger pinhole made the lights from different parts of the light source coincide and the light intensity became uniform. The result shows that pinhole size affects the noises rather than incident angle.

Table 5.2 Light intensity I and standard deviation σ of the test pattern image for a 400-μm-diameter pinhole.

Incident angle θ, deg	40	50	60	70
Light intensity I	7075	7090	7088	7069
Standard deviation σ	226	230	222	219

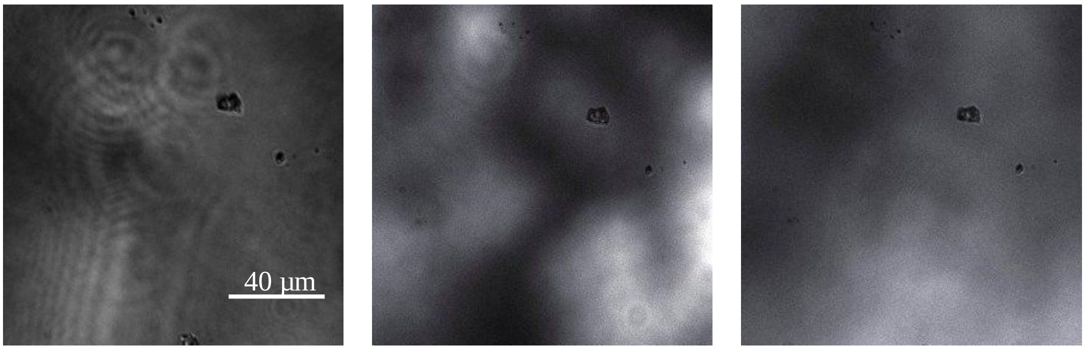

d: 20 µm d: 100 µm d: 200 µm

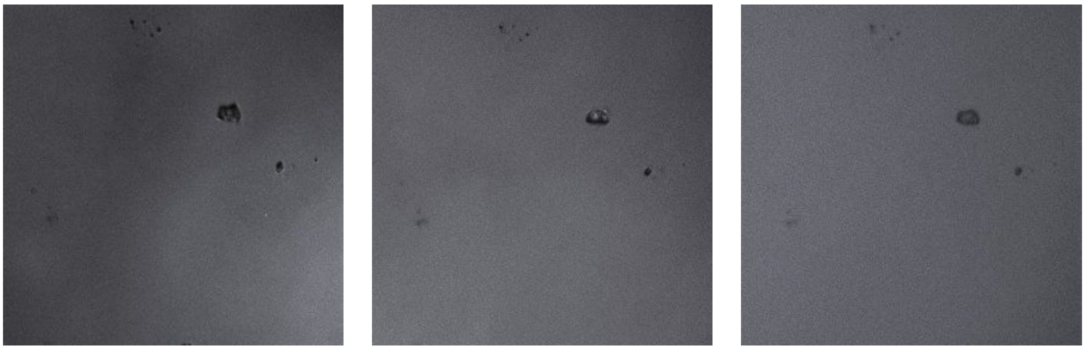

d: 400 µm d: 1 mm d: Non-pinhole

Fig. 5.9 Noise images for different pinhole diameters.

5.5.3 Thickness Resolution

As the effect of incident angle on the noise *N* can be ignored and the ellipsometric signal reached the maximum when the incident angle θ was 60 deg, we compared the thickness resolutions for different pinholes when the incident angle θ was 60 deg. The results calculated using Eq. (5.2) are shown in Fig. 5.10. The sample was a disk with a 2.7 nm-thick lubricant film, and the intensity for the unlubricated disk I_d was adjusted as a fixed value so that the effect of shot noise on standard deviation could be omitted. It was measured for 10 times for each pinhole to obtain the thickness resolution, and the result shows in Fig. 5.10 is the average one. The error bar shows standard deviation of the thickness resolution for each measurement. In Fig. 5.10, the experiment at a diameter of 5000 μm means that without pinhole. The results indicate that when the pinhole diameter is from 20 μm to 400 μm, the thickness resolution becomes better with the increase of the pinhole diameter, due to the noise suppression and the best thickness resolution was achieved when pinhole diameter was 400 μm and took almost equal values for pinhole diameter of 1000 μm and non-pinhole (5000 μm). In this experiment, a 400-μm-diameter pinhole was chosen rather than 1000 μm and non-pinhole, since the size of the light source is well controlled so that the smaller width of the incident angle $\Delta\theta$ could be obtained and might be easy to adjust the experiment setup. The power of light source was also increased comparing with the data in Table 5.2 to obtain a better thickness resolution. In addition, as explained in Section 5.3.3, the Shorter wavelength makes the intensity contrast larger, using a light source with short wavelength and increasing the input light intensity by increasing the output power of the light source, signal $I\text{-}I_d$ was improved. By the above improvements, the achieved thickness resolution was about 0.2 nm as shown in Table 5.3. The intensity on the left side in Table 5.3 (I = 11066) is quite larger than that in Table 5.2 (I = 7088). The reason is that in Table 5.2, I compared the resolution for different incident angles. In order to reduce the effect of shot noise for different light intensities, the light intensities on the CCD should be adjusted at the same level for different incident angles. Since light intensity reaches the maximum for θ = 70 deg shown in Table 5.2 (I = 7069).The light power of θ = 40, 50, 60 deg should be reduced. And the intensity in Table 5.3 is the maximum when θ = 60 deg for optimum of resolution.

Thus, choosing 400-μm-diameter pinhole and incident angle of 60 deg and increasing the light intensity can provide the higher ellipsometric signal, which can improve thickness resolution. The thickness resolution can be improved from 0.8 nm to 0.2 nm. The image of the 2.2 nm-thick lubricant films taken by the modified VEM is shown in Fig. 5.11. The noise images as shown in Fig

5.9 could be reduced.

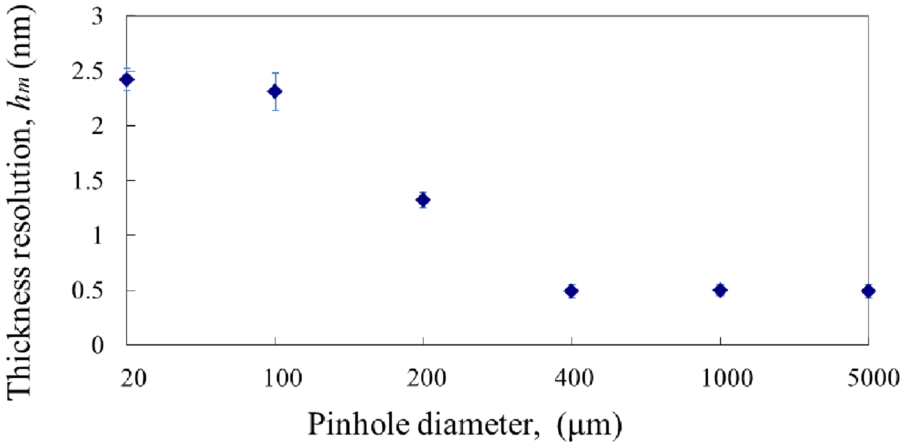

Fig. 5.10 Thickness resolution for different pinholes (θ = 60 deg).

Table 5.3 Thickness resolution for increasing the light intensity, θ = 60 deg.

	Before increasing	After increasing
Film thickness, h (nm)	2.7	2.2
Wavelength, λ (nm)	512	460
I	11066	16936
I_d	8637	15919
σ	437	104
SNR	5.56	9.78
h_m	0.49	0.23

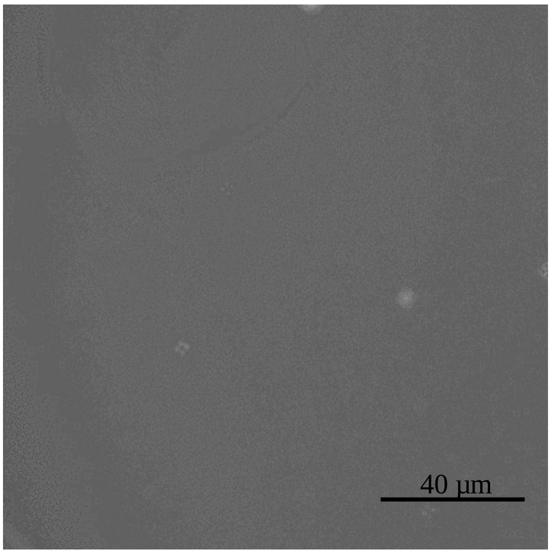

Fig. 5.11 An VEM image of liquid uniform film (Thickness = 2.2 nm)

5.6 Summary

The method to improve the thickness resolution was presented by analyzing the effects of incident angle and pinhole size on the SNR. Both the incident angle and pinhole size affect the ellipsometric signal, significantly, as well as the pinhole size may determine the noise level. Thus, by choosing the optimum pinhole size and incident angle (400-µm-diameter pinhole and 60-deg-incident angle in this setup), the thickness resolution was improved to 0.2 nm.

Chapter 6 Obersavation of Dewetting of Molecularly Thin Lubricant Films

As explained in previous chapters, VEM with a thickness resolution of the order of 0.1 nm was demonstrated. In this chapter, application of the VEM is observavtion of molecularly thin lubricant films. Here, dewetting of thin lubricant films is focused on. Dewetting is a process that can occur at a solid-liquid or liquid-liquid interface. For unstable thin lubricant films, because of the larger interaction between lubricant molecules than that between lubricant and disk, the lubricant films coheres and forms droplets. Dewetting on the magnetic disks attracts many researchers, because the dynamic performance of nm-thick lubricant on disks has significant effect on the recording density improvement of the HDD, due to the small gap of 2-3 nm between the head and disk. In this chapter, we observed the dewetting by the VEM. The observation of dewetting process can also help us evaluate our optical system.

6.1 Materials and Methods

In our experiment, both 2.5 inch PMR disks and 3.5 inch LMR disks were used as the substrate, so that the phenomenon can be compared on different types of substrates. As explained in Section 3.1.1, the LMR disk and PMR disk have different surface profiles, with and without nano-textures, respectively. Polar perfluoropolyether (PFPE) lubricants (Fomblin Zdol4000) with molecular weight of about 4000g/mol were used as the lubricant samples. The polarizer and analyzer angles were adjusted so that the light intensity I was proportional to the thickness h in this measurement. Since the two types of disk had different complex index of refraction N, the polarizer and analyzer angles were also different. The angles of these polarization elements in the experiments are shown in Table 6.1.

The scanning ellipsometer was also used to obtain the film thickness in this experiment rather than phase shift method by using VEM, since dewetting occurred in a short time after film application. Although phase shift method could determine the film thickness by VEM itself, the polarizer was manually rotated and it took much time for the measurement. Procedure of dewetting observation of the lubricant film distribution by VEM is as follows:

1. Z03 lubricant with HFE-7200 was diluted. And the mixture was stirred for about 20 minutes. The concentrations of the solution were 0.15%, 0.20% and 0.40% depending on the target film thickness.
2. The amplitude ratio Ψ and phase difference Δ of the magnetic disk without the lubricant were measured with a scanning ellipsometer, and refractive index n and extinction coefficient k of the magnetic disk were obtained. Since the diameters of the two types of disks were different, the measurement range were also different. For LMR disks, the laser spot was scanned on the disk in the radial direction (r = 24 to 32 mm). The scan step was 0.05 mm, and sampling points were 161 points. For PMR disks, the laser spot was scanned on the disk in the radial direction (r = 15 to 25 mm). The scan step was 0.1 mm, and sampling points were 101 points. The thickness was obtained as an average value for four times measurement at each measurement point.
3. Using the solution prepared at Step 1, the lubricant was applied to disks mentioned in Step 2 by a dip coating method. The removal speed was adjusted between 0.5 ~ 2.6 mm / sec, depending on the target film thickness, and the lubricant film was partially coated. The length of film covered region in the radial direction from the outer periphery of disk space was about 30 mm.

4. The thickness of the coated film was measured by the ellipsometer immediately after the coating. In addition, the scan range was the same as Step 2.
5. After the measurement of film thickness in Step 4, the sample was promptly set to VEM and lubricant film image was taken. The camera settings were exposure time 0.10 sec, gain 2, gamma 1, pixel size 512 × 512, binning 1 × 1, on-chip charge multiplication gain 2800.
6. After the observation of dewetting (about 30 min after observation), move the sample stage so that the lubricant uncovered region could be observed by the VEM, and image was taken with the camera settings the same as in Step 5.

Table 6.1 Angles of polarization elements in the experiments for different disks.

Disk type	PMR	LMR
complex index of refraction *N*	2.1-3.5i	2.3-3.9i
Angle of polarizer *P* (deg)	55	86
Angle of quarter wave plate *Q* (deg)	45	45
Angle of analyzer *A* (deg)	39.3	34.2

6.2 Results

The observation of lubricant films with six kinds of thickness on the PMR disks was conducted. The average value of the thicknesses were measured with an ellipsometer : 8.4, 7.1, 6.6, 5.2, 4.0 and 2.4 nm. On the other hand, dewetting of 6.6-nm-thick film on an LMR disk was observed for comparison. The observation started about 5 minites after lubricant application. The time was recorded from the beginning of the observation. The area of the observation was 160 × 160 μm^2.

- **8.4 nm-thick lubricant film on PMR**

Figure 6.1 shows the dewetting images of the 8.4 nm-thick polar lubricant film on the PMR disk observed in real time by our VEM.

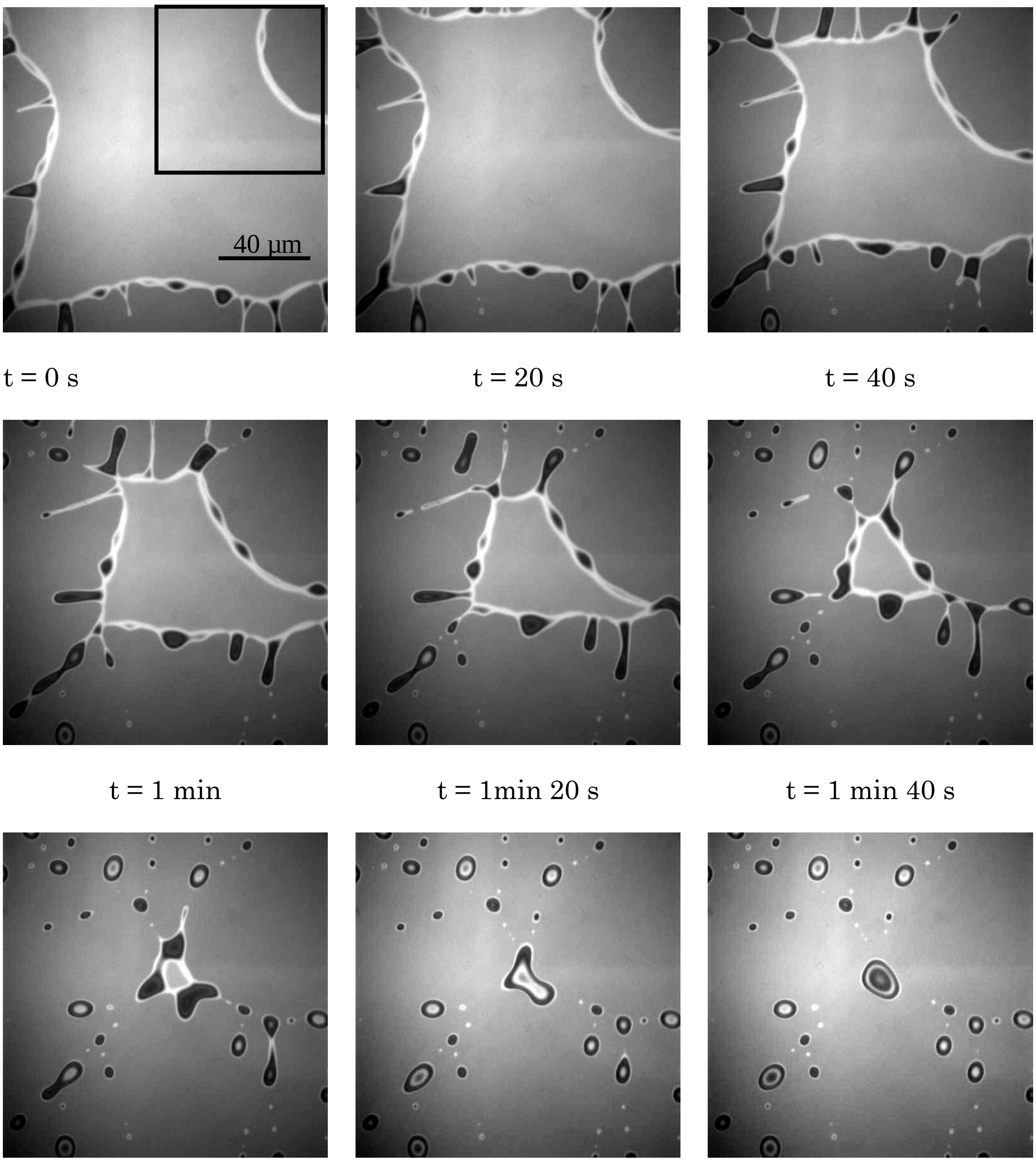

t = 0 s t = 20 s t = 40 s

t = 1 min t = 1min 20 s t = 1 min 40 s

t = 2 min t = 2 min 20 s t = 2 min 40 s

Fig. 6.1 VEM images of 8.4 nm thick lubricant on PMR at different times.

- **7.0 nm-thick lubricant film on PMR**

Figure 6.2 shows the dewetting images of the 7.1 nm-thick polar lubricant film on the PMR disk.

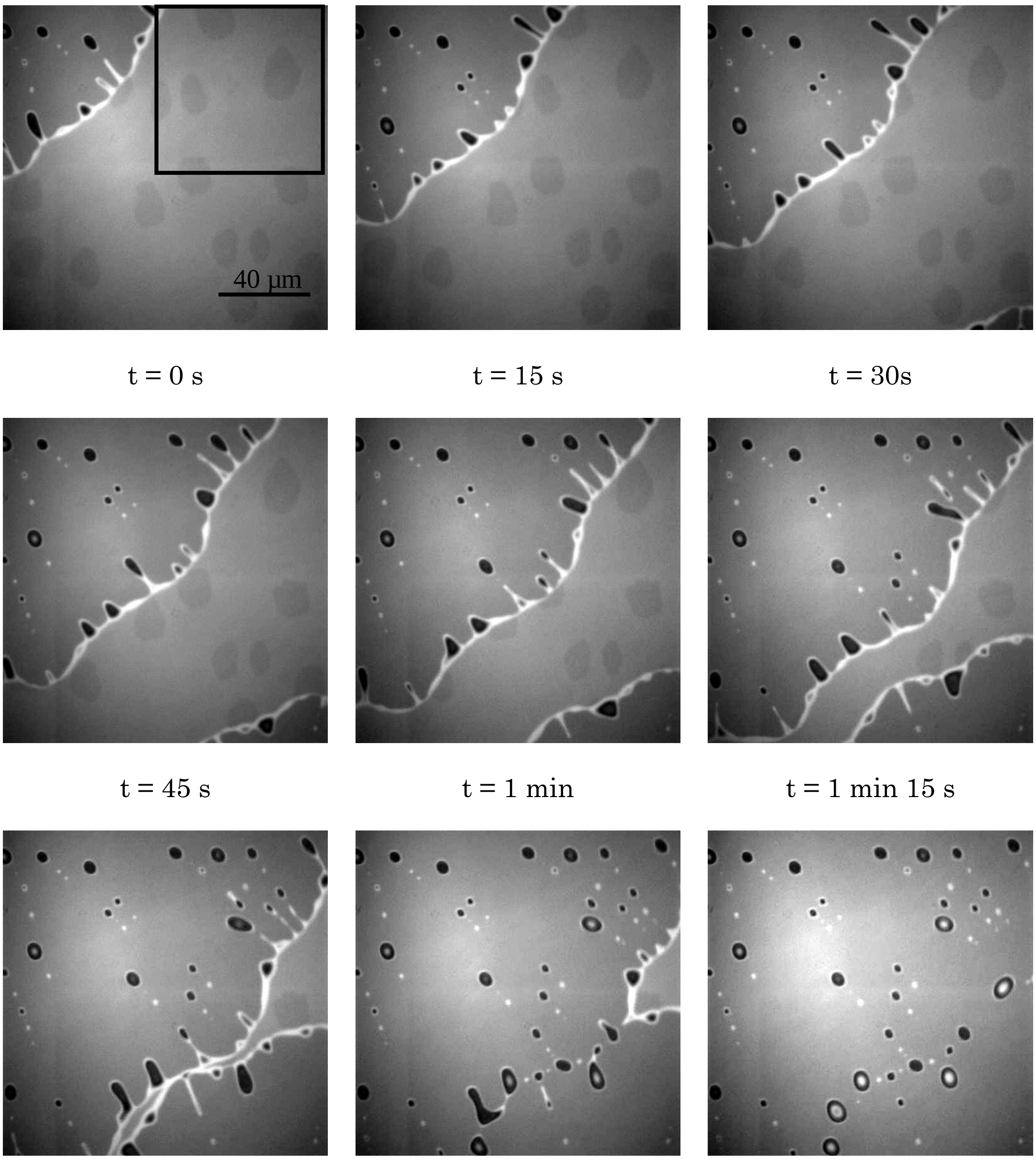

t = 0 s

t = 15 s

t = 30s

t = 45 s

t = 1 min

t = 1 min 15 s

t = 1 min 30 s

t = 1 min 45 s

t = 2 min

Fig. 6.2 VEM images of 7.1 nm thick lubricant on PMR at different times.

- **6.6 nm-thick lubricant film on PMR**

The dewetting images of the 6.6 nm-thick polar lubricant film is shown in Fig. 6.3.

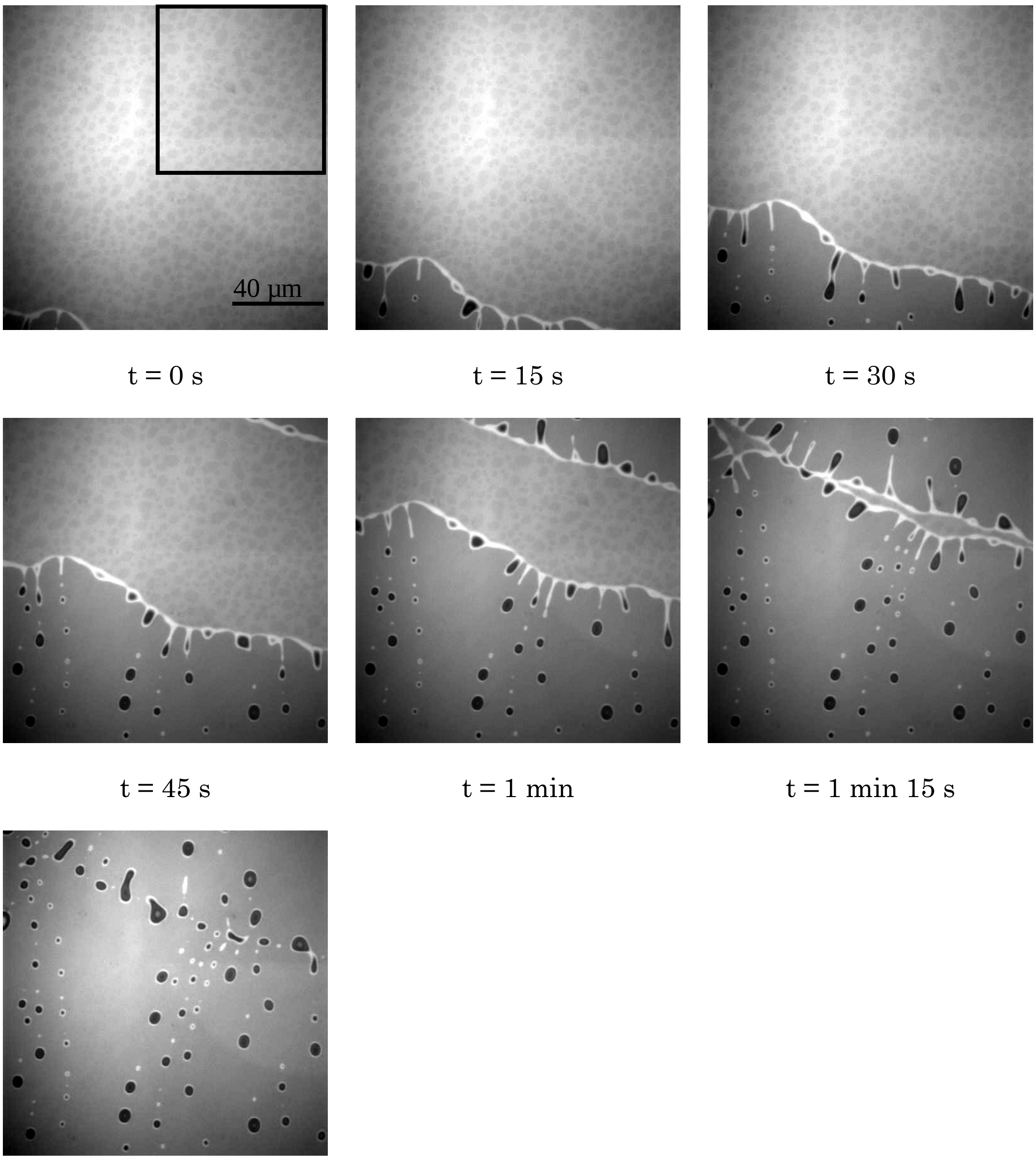

t = 0 s
t = 15 s
t = 30 s
t = 45 s
t = 1 min
t = 1 min 15 s
t = 1 min 30 s

Fig. 6.3 VEM images of 6.6 nm thick lubricant on PMR at different times.

- **5.2 nm-thick lubricant film on PMR**

The dewetting images of the 5.2 nm-thick polar lubricant film is shown in Fig. 6.4.

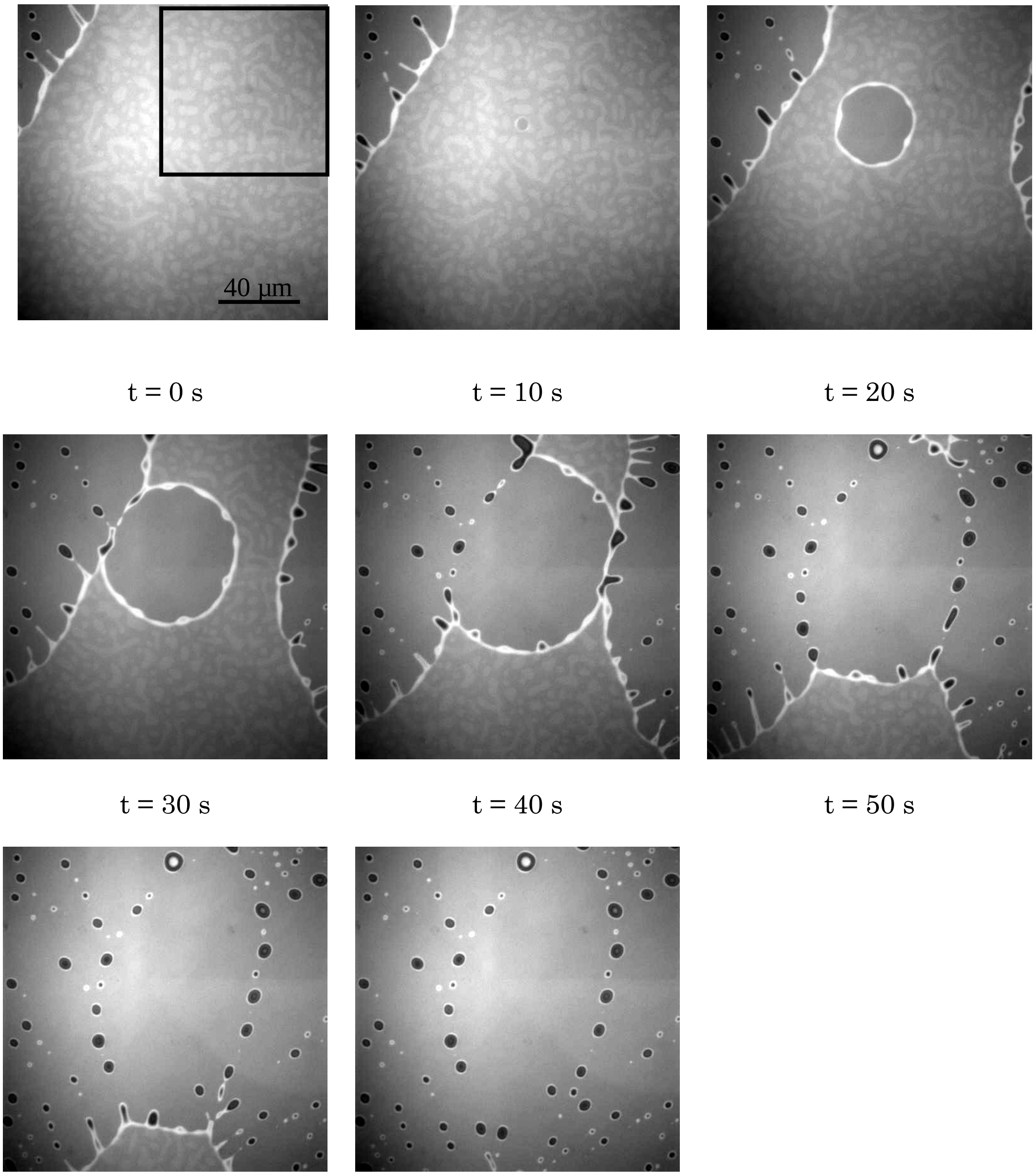

t = 0 s t = 10 s t = 20 s

t = 30 s t = 40 s t = 50 s

t = 1 min t = 1 min 10 s

Fig. 6.4 VEM images of 5.2 nm thick lubricant on PMR at different times.

- **4.0 nm-thick lubricant film on PMR**

The dewetting images of the 4.0 nm-thick polar lubricant film is shown in Fig. 6.5. However, it dewetted when observation for this thickness, so only droplets can be seen.

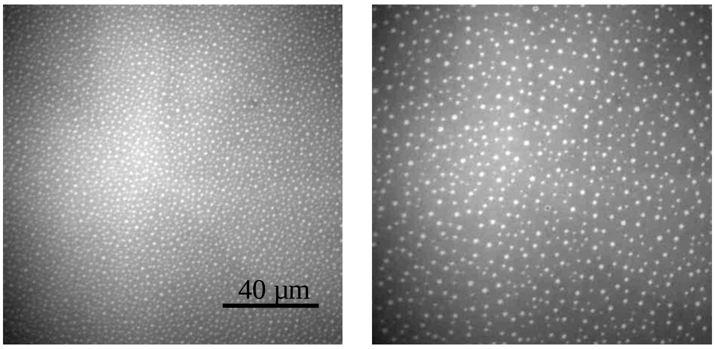

t = 0 s t = 7 min

Fig. 6.5 VEM images of 4.0 nm thick lubricant on PMR at different times.

- **2.4 nm-thick lubricant film on PMR**

In Fig. 6.6, it is the image for initial thickness of 2.4 nm film, it also dewetted due to the high speed of dewetting.

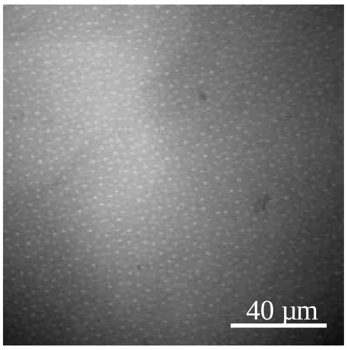

t = 0 s

Fig. 6.6 VEM images of 2.4 nm thick lubricant on PMR at different times.

- **1.5 nm-thick lubricant film on PMR**

In Fig. 6.7, it is the image for initial thickness of 1.5 nm film, it looks uniform without dewetting.

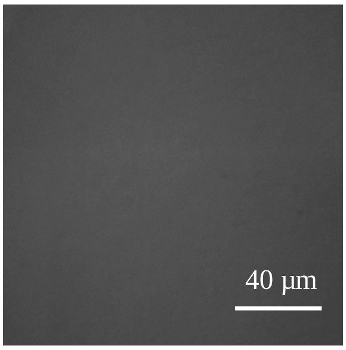

Fig. 6.7 VEM images of 1.5 nm thick lubricant on PMR at different times.

- **6.6 nm-thick lubricant film on LMR**

At last, in Fig. 6.8, it shows the dewetting images of the 6.6 nm-thick polar lubricant film on a longitudinal magnetic recording disk.

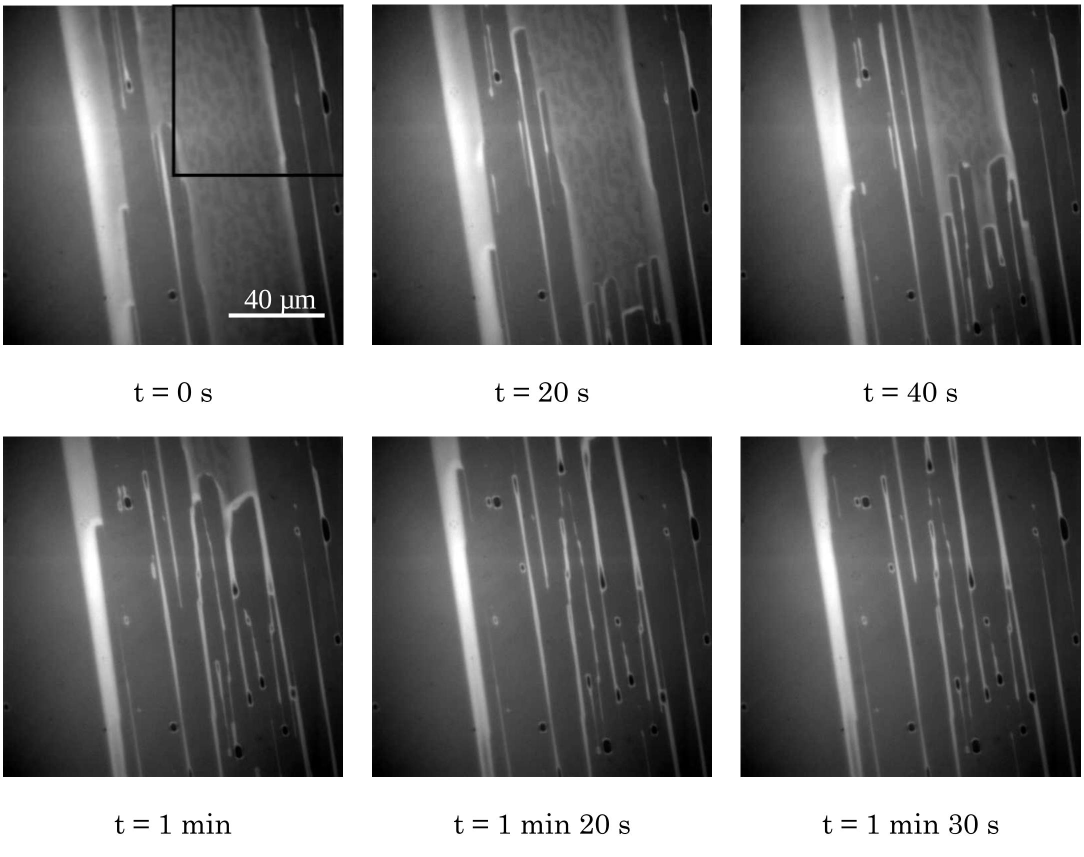

t = 0 s t = 20 s t = 40 s

t = 1 min t = 1 min 20 s t = 1 min 30 s

Fig. 6.8 VEM images of 6.6 nm thick lubricant on LMR at different times.

6.3 Discussion

I tried the observations of lubricant with the thicknesses of from 2 to 8 nm. For the films with the thickness of smaller than 4 nm, the lubricant had dewetted already when the observation started (about 5 min after film application). I succeeded in observing the dewetting for the films with the thicknesses of from 5 to 8 nm. In order to find the linear relationship between light intensity and film thickness, the adjustment of polarization devices were done for each film.

For the film with the thickness of about 1.5 nm, monolayer lubricant forms, and the molecules of lubricant adsorb on the disk well, therefore, dewetting does not occur. For the films with the thickness of less than 4 nm, it dewetted immediately after film application some droplets were observed as shown in Fig. 6.5 and 6.6. The size of the droplets of the thickness of 2.4 nm seems smaller than those of the thickness of 4.0 nm. When the thickness of the film increases, the dewetting process becomes slow. In addition, it shows different patterns for different thickness. The cross-sectional views of magnified images of Fig. 6.1-6.4 are shown from Fig. 6.9 to Fig. 6.12. Many bumps on flat film were observed when the thickness of the film is 5.2 nm (Fig. 6.12). The height of the bumps was about 2 nm from the flat film surface. When it became thicker, large number of bumps connected, it looked like some holes as in Fig. 6.10 and 6.11. The holes with the depth of about 3.5 nm from the flat film can be observed for 7-nm-thick lubricant with the diameter of around 10 μm, and the depth of the holes became smaller (about 3 nm) from the flat film for 6.6-nm-thick lubricant. Also, the holes became smaller but more. Moreover, the dewetted 8.4-nm-thick lubricant film did not include bumps and holes. It kept flat although the entire film shrunk due to dewetting as shown in Fig. 6.9.

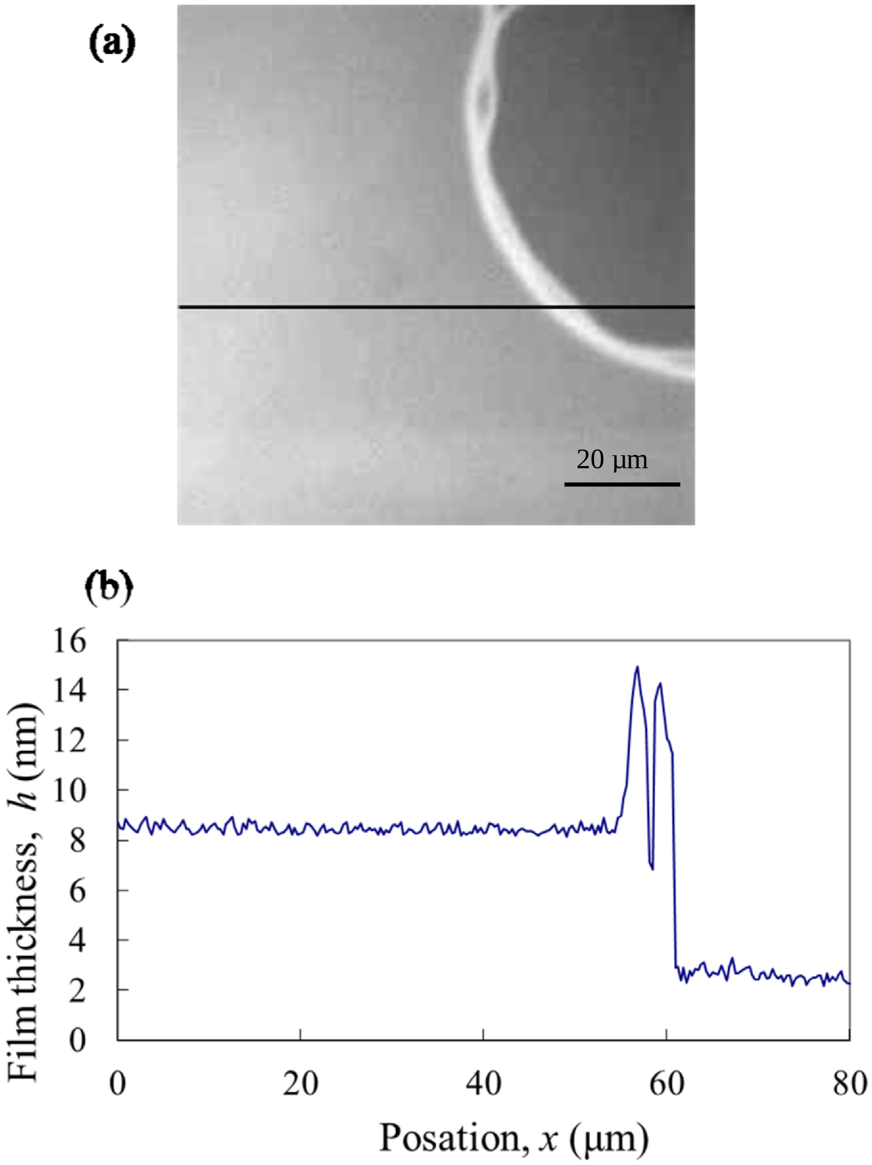

Fig. 6.9 Cross-sectional view of magnified image at t = 0 in Fig. 6.1 (h = 8.4 nm). (a) The magnified image of the upper right rectangle framed in the first image of Fig. 6.1 (t = 0 s). (b) Cross-sectional view on the line in Fig.6.9 (a).

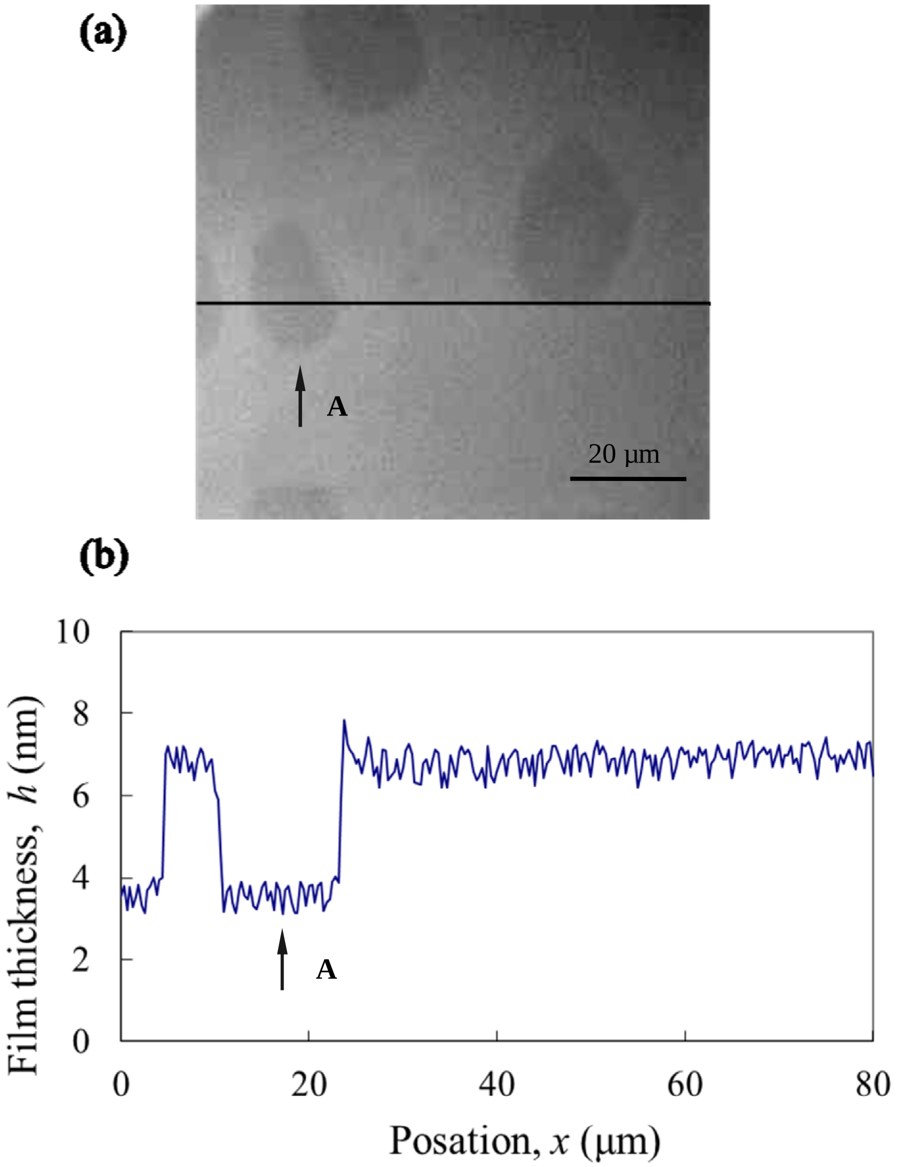

Fig. 6.10 Cross-sectional view of magnified image at t = 0 in Fig. 6.2 (*h* =7.1 nm). (a) The magnified image of the upper right rectangle framed in the first image of Fig. 6.2 (t = 0 s). (b) Cross-sectional view on the line in Fig.6.10 (a).

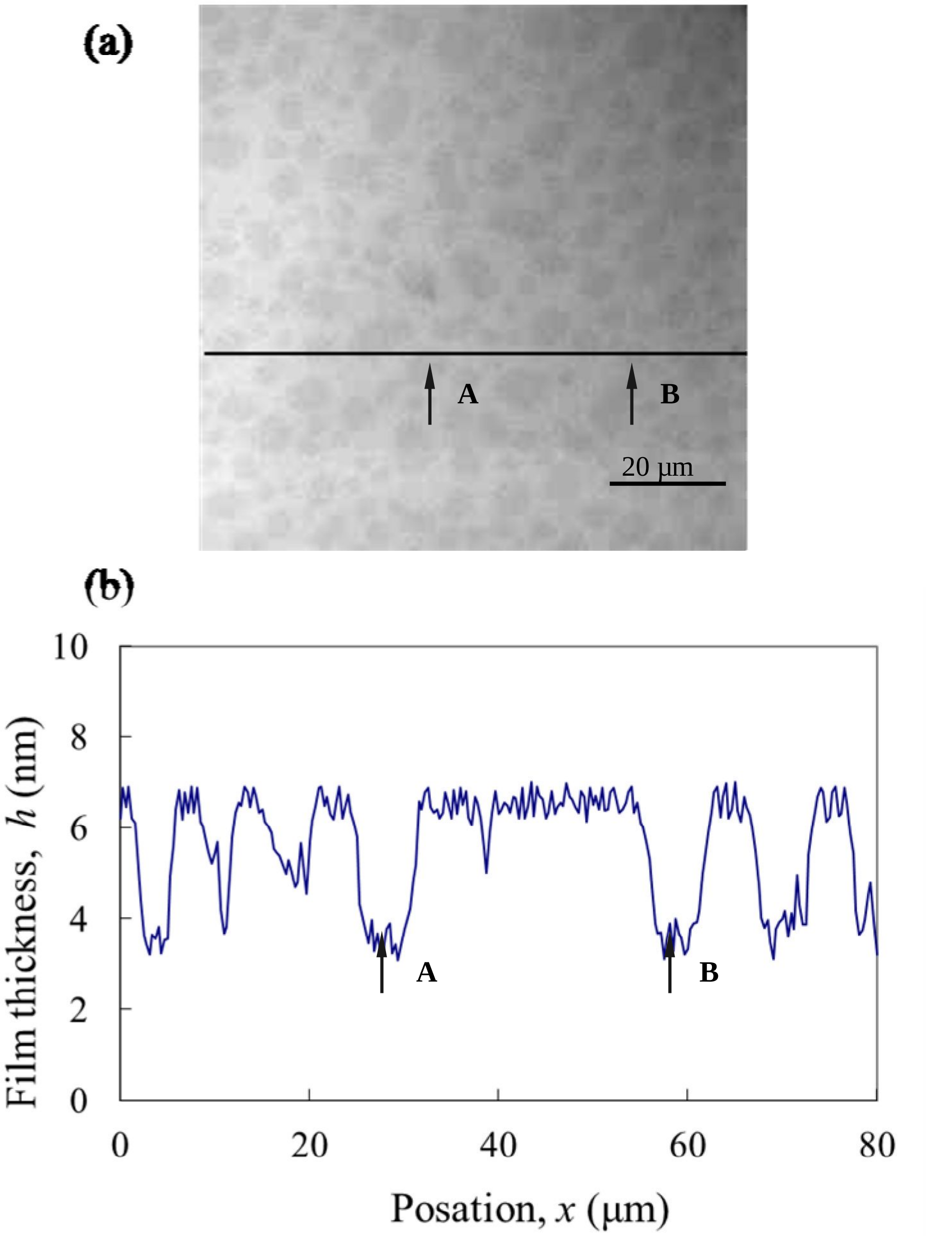

Fig. 6.11 Cross-sectional view of magnified image at t = 0 in Fig. 6.3 (h = 6.6 nm). (a) The magnified image of the upper right rectangle framed in the first image of Fig. 6.3 (t = 0 s). (b) Cross-sectional view on the line in Fig.6.11 (a).

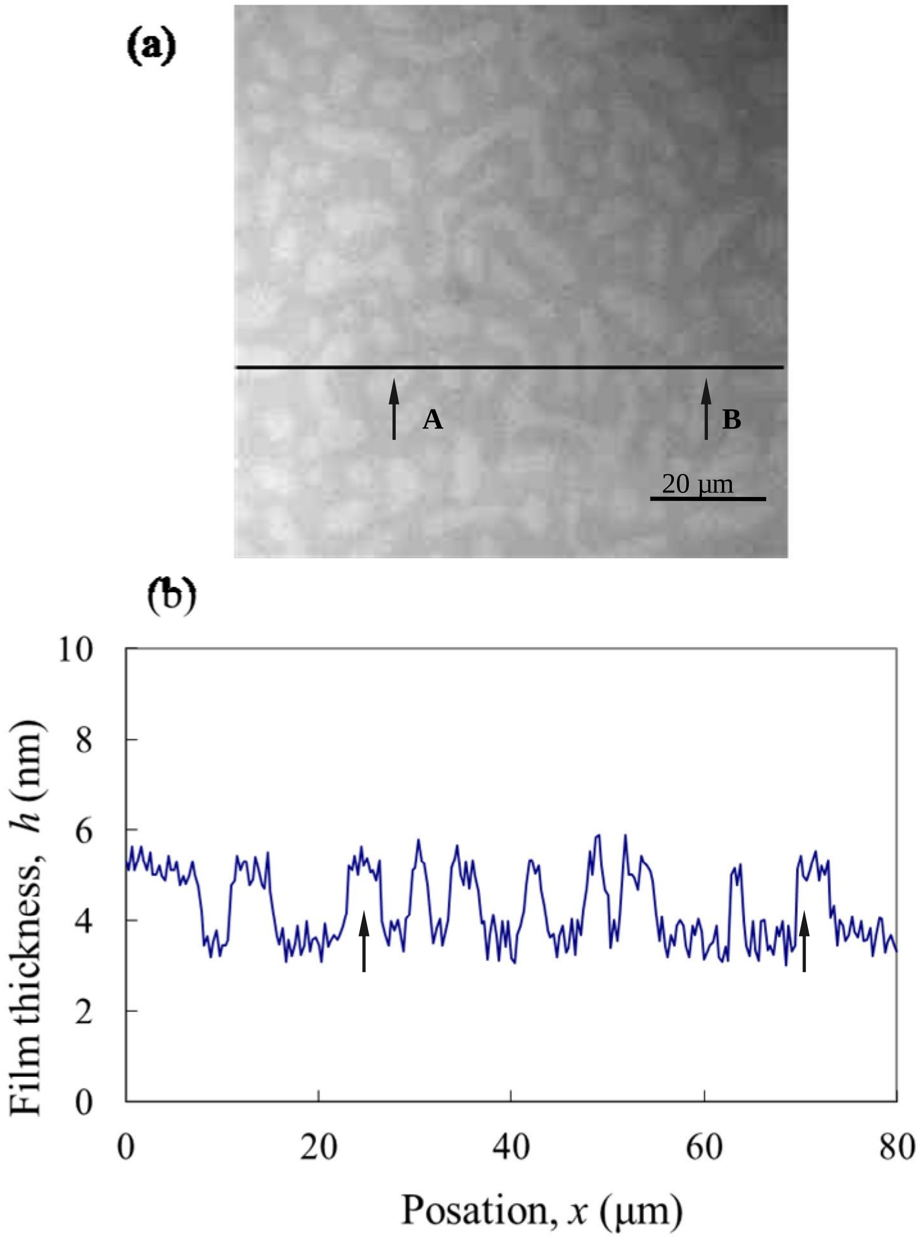

Fig. 6.12 Cross-sectional view of magnified image at t = 0 in Fig. 6.4 (*h* = 5.2 nm). (a) The magnified image of the upper right rectangle framed in the first image of Fig. 6.4 (t = 0 s). (b) Cross-sectional view on the line in Fig.6.12 (a).

To analyze the difference of dewetting depending on film thickness, surface energy was measured for different thicknesses. 1/2 contact angle method was used. The result is show in Fig. 6.13. The contact angle measurement started about 3 minutes after lubricant application, dewetting occurred and the film thickness was changing during the measurement. Therefore, the peak of dispersive component at thickness around 3 nm may be measurement error. However, I could obtain two minima when the thicknesses are about 2 and 4 nm and two maxima when the thicknesses are about 3 and 6 nm. 2 nm-thick was considered to be monolayer lubricant, so it was stable and the surface energy reached the minimum. Fig. 6.9 shows that the thickness of dewetted region was about 2 nm, which correspond to the monolayer thickness. Comparing the dewetting images from 5.2 nm-thick to 7 nm-thick lubricant films in Fig. 6.10 - Fig. 6.12, the lower region in the dewetting films had a similar thickness of about 3.5 - 4 nm, also the surface energy reached the minimum at about 4 nm-thick, since a triple layer was formed, and the polar end groups of the upper layer were bonded to that of the middle layer. The surface energy reached the peaks at 3 and 6 nm-thick of the lubricant, where two and four layeres of molecules were formed, respectively. Since most of the polar end groups of the upper layer were not bonded for the two situations, the films were unstable and dewetting could occur. In my opinion, the different patterns of the dewetting depending on thickness are due to the volume of the lubricant. For 6-8 nm-thick lubricants, the volume is larger, and films can be formed, however, for 5 nm-thick lubricant was not enough to form the film, therefore, the thicker region took a shape like bumps.

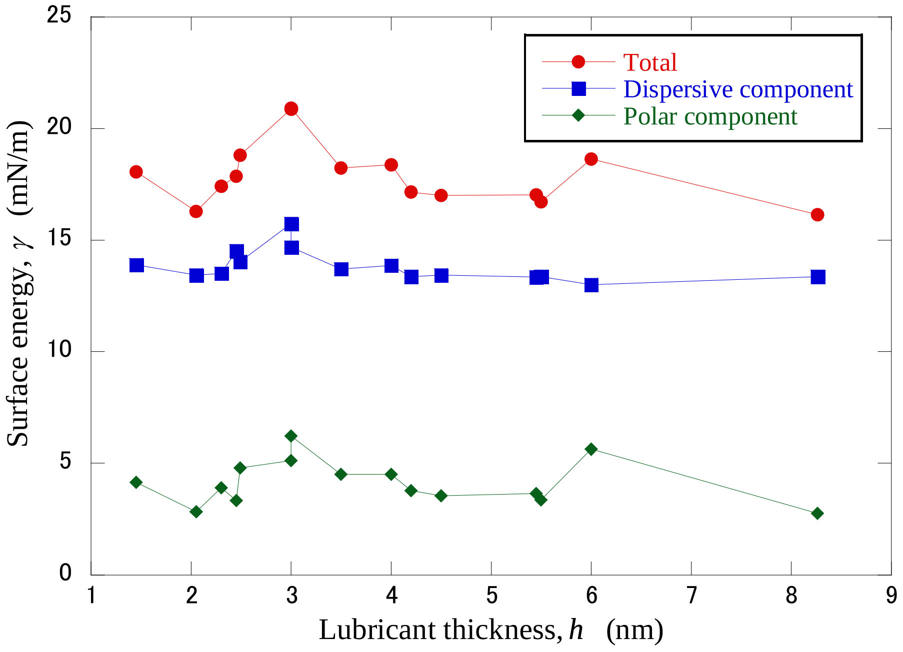

Fig. 6.13 Measured surface energy vs. film thickness.

Then I compared the dewetting processed of 6.6-nm-thick lubricant on the PMR disk with the LMR disk, as shown in Fig. 6.3 and 6.7. Images were taken from 0 s to 1 min 30 s after the start of the observation. The film was unstable at this thickness. From the results, small holes with the depth of about 2 nm from the flat film were observed for both films, however the shapes were different. The holes were almost elliptically shaped along the nano-texture for LMR disk, and they shaped like a circle for PMR one. Also the ways of dewetting were different. In LMR disks, grooves with the thickness of about 3 nm and width of 8-12 μm along the nano-texture were formed, the lubricant excluded from the groove spread perpendicular to the nano-texture. On the other hand, in the PMR disks, the groove was not formed but bumps or holes were formed. The dewetting speed on the both types of disks is compared below. Because dewetting proceeded in any directions in PMR disk, it was difficult to obtain the one- dimensional speed in m/s. I used the shrinking area of the film per second to define the dewetting speed. The dewetting speed was defined as by

$$v = A/t\,. \tag{6.1}$$

where A is the area of the film, and t is the measurement time for. The speed that averaged over the samples was obtained. The dewetting speed was 116.7 μm^2 / s for LMR disk, and 241.5 μm^2 / s for PMR one. These results indicate that the nano-texture on the magnetic disks affects the way and speed of dewetting process.

In addition, by using the dewetting image the thickness resolution of VEM was evaluated. Since the film thickness h is proportional to the light intensity I, I was measured in the experiment and the relationship of $h = aI$ (a = 1/1123 in this experiment) was used to convert light intensity I to thickness h. A big black hole can be found in Fig. 6.14 (a). The film thickness is proportional to the light intensity when the thickness is from 0 to about 30 nm. As for thicker films, the relationship between the film thickness and light intensity is a periodic function due to the optical interference. Therefore the black hole is considered to be a big droplet with much larger thickness. Figure 6.14 (b) shows a cross-sectional view at line L in Fig. 6.8 and arrows A and B indicate the corresponding positions in Fig. 6.14 (a), respectively. From the observation by VEM, small holes (arrow A and B in Fig. 6.14 (a)) were found. As the thickness of the flat region of the lubricant was about 6.6 nm, the depths of the small holes were about 1.5 nm, which was measured from the flat film surface. This demonstrates that the VEM can resolve about 1-nm-thickness difference of the lubricant film. The film on the right side, which is the edge of the illumination field, appeared to be thinner than that on the left side due to the ununiformity of the light source intensity. And this could be reduced by the adjustment of the light source in further experiment.

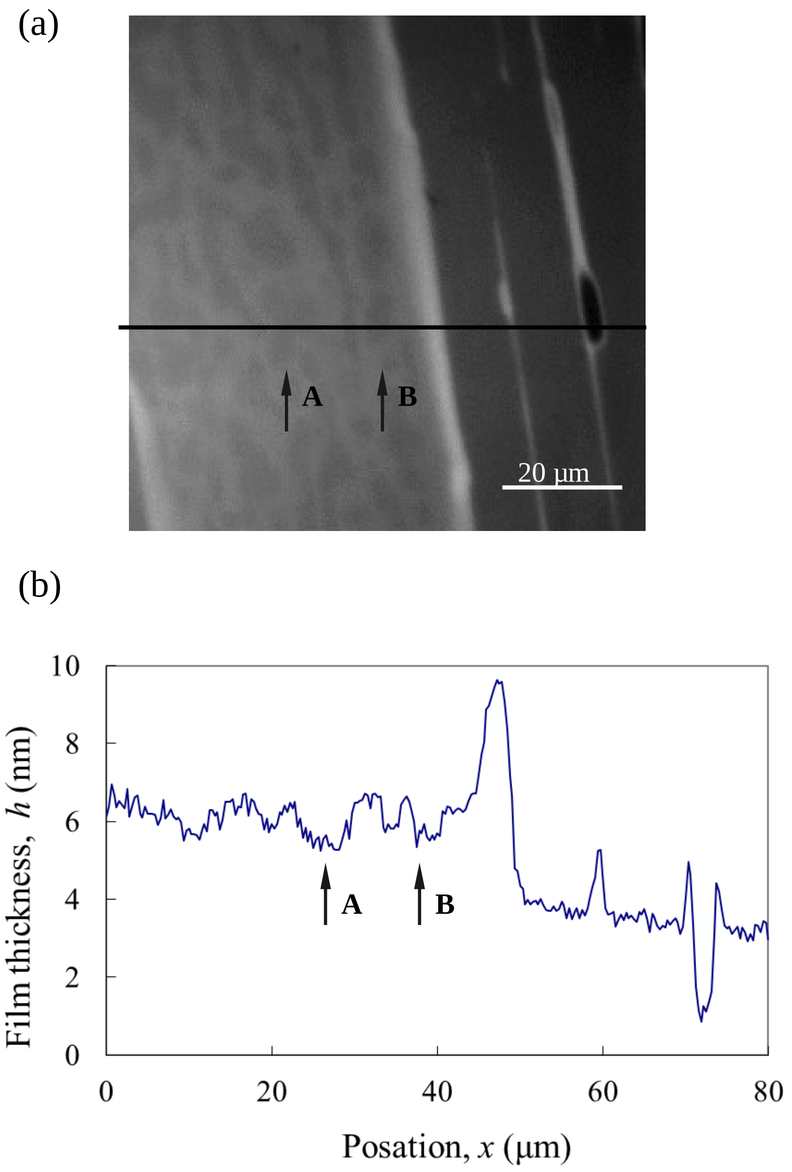

Fig. 6.14 Cross-sectional view of magnified image at t = 0 in Fig. 6.8 (h = 6.6 nm). (a) The magnified image of the upper right rectangle framed in the first image of Fig. 6.8 (t = 0 s). (b) Cross-sectional view on the line in Fig.6.14 (a)

6.4 Summary

Dewetting of lubricant on PMR and LMR disks was observed by the developed VEM. Different patterns were visualized in real-time for different film thicknesses. And comparing with the dewetting on LMR disk and PMR disks shows a difference of the dewetting process due to the surface structure. The nano-texture affects the way and speed of the dewetting. It also demonstrated that the developed VEM can visualize nm-thick thin liquid lubricant films in real-time.

Chapter 7 Backside Illuminated VEM

7.1 Introduction

With the development of HDDs, in the near future, the contact or near-contact HDI will be needed to increase the recording intensity, and meniscus formation or lubricant pick-up will occur in this type of HDI. Therefore, real-time observation of these phenomena becomes the new requirement for the VEM in the future. In order to imitate the heading flying on the magnetic disk, a sliding probe is usually used on the magnetic disk. In the VEM presented in the previous chapters, the illumination light comes from the lubricant film side. We call this type of VEM front-side illuminated VEM, which can provide high lateral resolution; however, it has a disadvantage of insufficient space for setting sliding probes because the working distance (WD) of the high magnification objective lens is small. In this chapter, to solve this problem, we propose a backside illuminated VEM, whose illumination system and objective lenses are set on the opposite of the sliding probe. The design of the backside illuminated VEM is described and the feasibility of the method is discussed.

7.2 Simulation Method

A schematic setup of backside illuminated VEM is shown in Fig. 7.1. In the backside-illumination VEM, the illumination light comes from the transparent substrate side and the off-axis light is focused onto the back focal plane of the objective lens to obtain the oblique illumination. This is similar to the off-axis Kohler illumination in the front-side illuminated VEM.In the backside illuminated VEM, the sliding probe can be set on the substrate because the space above the substrate is clear. However, the light path through the substrate may decrease the EM signal, because reflected light from the sample is detected as the EM signal and transparent substrate of the sample may decrease the intensity of the reflected light. The feasibility of the backside illuminated VEM is theoretically discussed below.

2 × 2 matrix method was used for the simulation as described in Chapter 2. We compared the simulated intensity of ellipsometric signal for backside illuminated VEM with that of the front-side one. For the simulation, a lubricated magnetic disk for HDDs was considered as a sample. The model of lubricated magnetic disks consisted of air, lubricant film magnetic disk. The refractive indices of air, lubricant, and magnetic disk were 1, 1.3, and 2.35-3.93i, respectively. The thicknesses of lubricant and substrate were 1-10 nm and infinite, respectively, for the front-side illumination. Since the magnetic disk might prevent the light pass through, the model consisted of air, glass, DLC and lubricant was used for backside illumination. The refractive indices of air, glass, DLC and lubricant were 1, 1.5, 2.4-0.5i, and 1.3, respectively, and thicknesses of glass, DLC and lubricant were 0.1 mm, 3 nm, and 1-10 nm, respectively. The layer models are shown in Fig. 7.2. The light source with the wavelength λ of 512 nm and the incident angle of 60 deg was used for all the simulation.

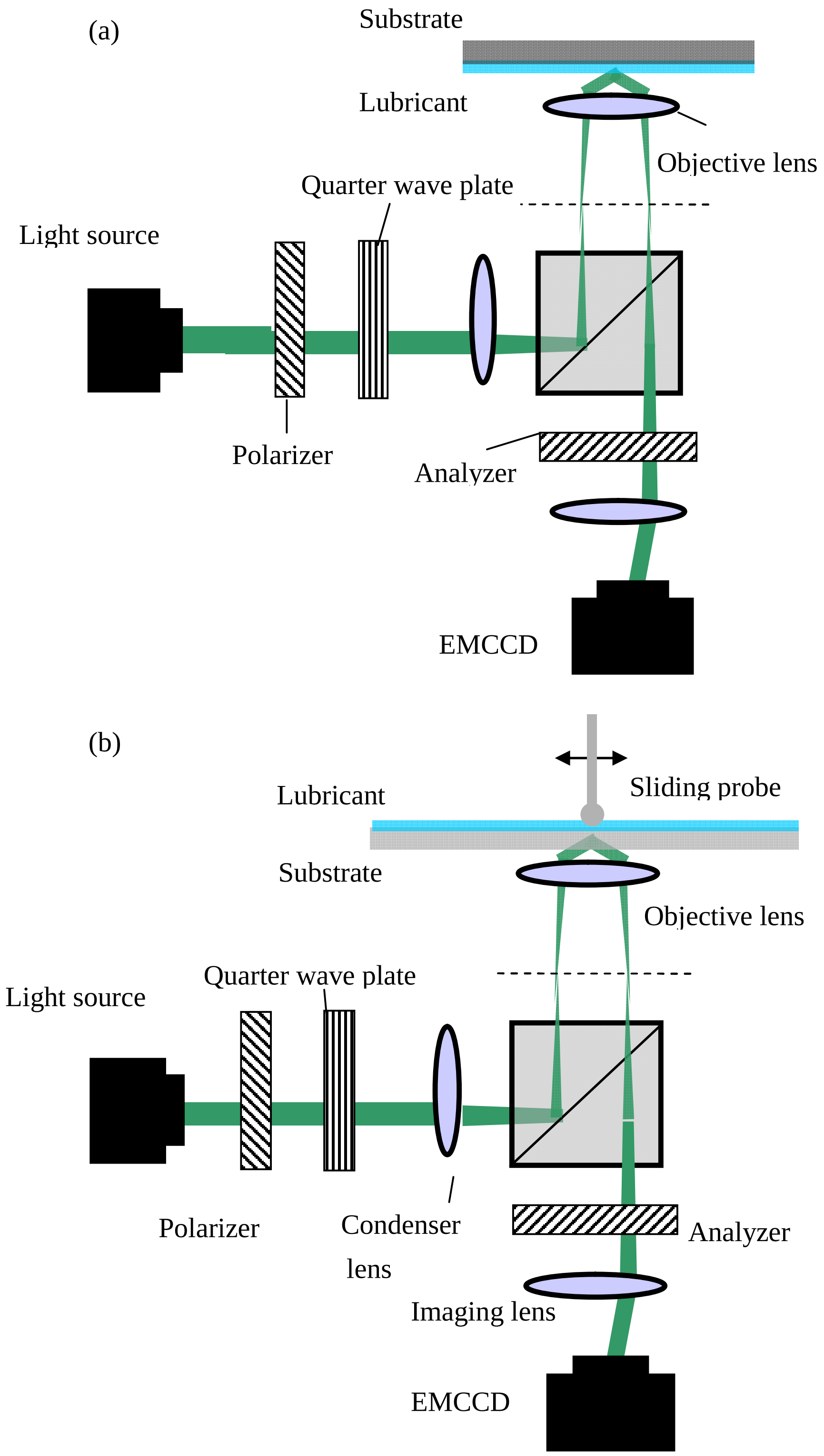

Fig. 7.1 Schematic setup of backside illuminated VEM compared with front-side illuminated VEM. (a) Front-side illuminated VEM. (b) Backside illuminated VEM.

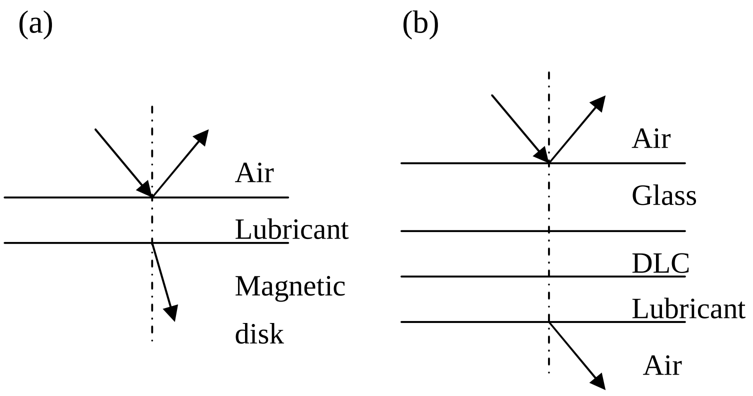

Fig. 7.2 Models of the magnetic disks for both front-side illumination and backside illumination. (a) The model for the front-side illumination. (b) The model for the backside illumination.

7.3 Results and Discussion

If the ellipsometric signal *I* is proportional to the lubricant thickness *h*, the signal can be directly converted to the thickness. This is suitable for real-time observation as described in the previous chapters. For the front-side illumination, this linear relationship can be obtained by adjusting the polarizer angle *P* as proved in Section 4.3. We also tried to find this *I*-*h* dependency on *P* for backside illumination. Figure 7.3 shows the simulated results of the effect of the polarizer angles on the *I*-*h* curve of backside illumination. I-I_d in the figure expresses the normalized intensity difference between the lubricated and unlubricated disks. The analyzer was fixed *A* = 171 deg. At this angle, the unlubricated disk was dark and ellipsometric signal reached the minimum, which means the null condition. The result shown in Fig. 7.3 indicates that at the polarizer angle P = 46 deg, the I-h linear relationship was obtained. This result means that the polarizer angle can be adjusted so that the ellipsometric intensity difference I-I_d is approximately proportional to the thickness h, and the intensity can be also convert to film thickness directly in backside illuminated VEM, which fits real-time observation.

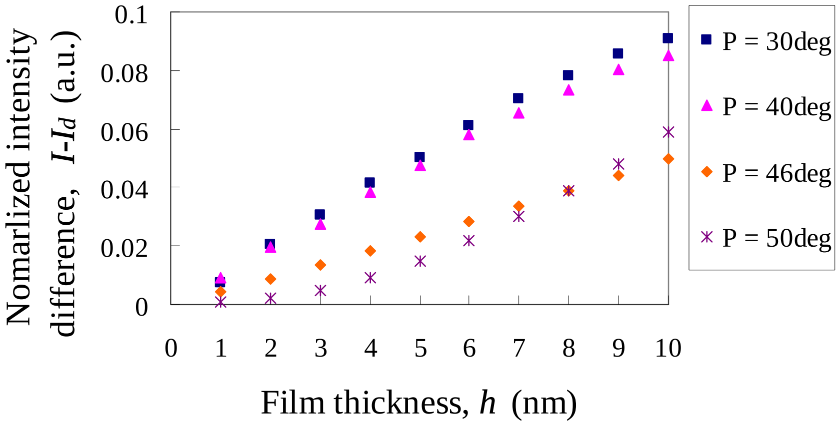

Fig. 7.3 Simulated relationships between ellipsometric signal and thickness at different polarizer angles *P* for the backside illumination.

In Fig.7.4, the simulated relationships between intensity difference I-I_d and thickness h for front side and back side illuminations are shown. The simulations, when the linear relationships between intensity I and thickness h was satisfied were established for both front-side illumination and backside illumination. From the simulation, we know both types of VEM have the same tendency when film thickness is from 1 nm to 10 nm; however the amplitude of I-I_d of backside illumination is about half of that of the front side for the same h. The thickness resolution is determined by SNR. As described in Chapter 5, SNR of the observed image is proportional to the square root of the intensity of the illumination light. It means the backside illumination has a lower thickness resolution than that of front-side illumination, since the value of thickness resolution of backside illumination is estimated at about 1.4 times larger than that of front-side illumination according to Fig. 7.4. For example, if the front-side illumination has the thickness resolution of 0.2 nm, it is about 0.3 nm for backside illumination. This means that the backside illumination VEM is feasible if SNR of *I* is improved. And if incident light intensity *I* is improved by 2 times, it can get the same thickness resolution as front-side one.

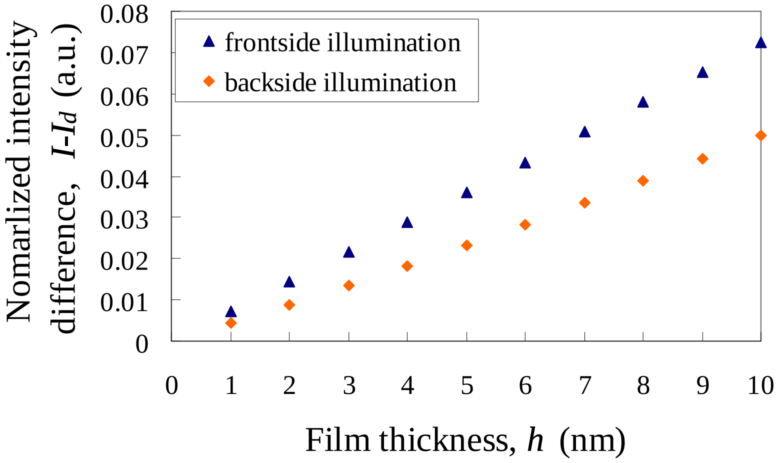

Fig. 7.4 Simulated relationships between ellipsometric signal *I* and thickness *h* for front side and back side illumination.

7.4 Summary

In this chapter, an improved VEM called backside illuminated VEM is presented. As the previous front-side illuminated VEM has the drawback of small WD, it is difficult for this type of VEM to observe the lubricant phenomena while head or probe is flying on the disk. In the backside illuminated VEM design, objective lens and the probe are set the opposite sides of the sample, so it can observe the sample while probe sliding on. However, to observe the lubricant from the substrate side, special samples which have high transmittance are needed, so that the detected signal weakened. Therefore, we proved the feasibility of this type VEM by comparing with the front-side illuminated VEM. The theoretical result indicates that the thickness resolution of backside illumination is about 1.4 times larger than that of front-side illumination.

Chapter 8 Conclusion

In HDD industry, the flying height of magnetic head has to be decreased continuously for the increasing of storage capacity. The contact or near cotact HDIs make the deformation of the lubricant film more important. Therefore, observation of the 1-2 nm thin lubricant film on the magnetic disk in real time is required to evaluate the performance of the lubricant. For the real time observation, EM is a good candidate. So the target of this study is to develop the EM for high resolution and visualization measurement with the lubricant films.

In Chapter 1, the current status of the HDD technologies was introduced as the background, as well as the structure of the magnetic disk and the lubricant. Then methods for measurement of the lubricant film were introduced, and the advantages and disadvantages of each method were described. It was concluded that EM is suitable for real time observation, but other conventional methods are not.

In Chapter 2, principle of EM was explained. Since it is based on the principle of the ellipsometry, the general knowledges of elliposometry such as the types, the principle, and the method for thickness determination were introduced. And the drawback of conventional EM narrow field of view at high lateral resolution was also pointed out. To overcome the drawback, a new type of EM vertical-objective-based EM (VEM) was proposed, the advantage was analyzed theoretically.

Form Chapter 3 to Chapter 6, the experiments for VEM were introduced, which contained the materials, methods, results and discussion, as well as we presented a development of VEM and the feasibility of the VEM for future target was proved in Chapter 7. In Chapter 3, the disks and lubricants were introduced as the sample materials in this study, as well as the method for lubricant application. In Chapter 4, the setup of our VEM was presented and the method to obtain the thickness of the thin films called phase shift method. By using the 2 × 2 matrix method, thickness determination by the phase shift method was investigated. VEM could provide a field of view of 160 × 160 μm^2, which was much larger as compared with the conventional EMs. Finally the lateral resolution was experimentally obtained at about 0.5 μm. In Chapter 5, I presented how to improve the thickness resolution of the VEM, so that it can apply to the measurement of lubricant films with a thickness of the order of 1 nm. In Chapter 6, the dewetting observation was introduced as an application of the developed VEM. Different dewetting processes for different thickness or on different subtrates were observed by the VEM, this also could prove high thickness resolution of the VEM. The conclusions are listed as follows:

1. A VEM for the real-time observation of thin liquid lubricant films was investigated. In VEM, a sample was illuminated with parallel, oblique light with well defined polarization by the off-axis light focusing onto the back focal plane of the objective lens. It provided thickness distribution as a dark-bright contrast image on the CCD. The vertical setup of the objective lens could provide sub-μm lateral resolution of about 0.5 μm which matched the theory well.
2. The angles of the polarization devices affected the relationships between the light intensity and the film thickness. So in the experiment, the analyzer angle was set when the null condition was satisfied, and polarizer angle was changed so that the light intensity is proportional to the film thickness, which means the light intensity can be directly converted into the thickness. Then a phase shift method was presented. It can determine the thickness with an error of about 0.3 nm. This method can make other thickness measurement devices such as an ellipsometer unnecessary.
3. The thickness resolution of VEM is defined as the thickness when SNR = 1. So SNR is required to be increased to improve the thickness resolution, which contains signal improvement and noise suppression. Effect of the power of light source, the incident angle and the width of the incicdent angles on the ellipsometric signal were analyzed for signal

improvement as well as the coherent noises were evaluated for noise suppression in VEM, especially pinhole size and the incident angle. By choosing the optimum design, the thickness resolution was finally achieved to 0.2 nm. The simulation of the relationship between the wavelength λ of the light source and the ellipsometric contrast ratio was done. The result indicates that shorter wavelength can provide a higher ellipsometric contrast ratio, which can be a reference for further experiment for the thickness resolution improvement.

4. Dewettings of lubricant on PMR and LMR disks were observed by the VEM, which revealed the different dewetting processes for the different structures of the disks and different thicknesses. The dewetting observations also supported that the VEM had a sub-nm thickness resolution.
5. An improved VEM called backside illuminated VEM is proposed, whose illumination system and objective lenses are set at the substrate side and can do real-time observation of the lubricant while probe sliding on. The feasibility of this type VEM has been proved.

References

（1） B. Hayes， Terabyte territory, *American Scientist*, 90, (2002), pp. 212-216.

（2） E. Eleftheriou, R. Haas, J. Jelitto, M. Lantz and H. Pozidis, Trends on storage technologies, *Data Engineering*, 33-4(2010), pp. 4-13.

（3） Frank E. Talke, On tribological problems in magnetic disk recording technology, *Wear*, 190, (1995), pp. 232-238.

（4） C. M. Mate, Q. Dai, R. N. Payne, B. E. Knigge, and P. Baumgart, Will the numbers add up for sub-7-nm magnetic spacings? Future metrology issues for disk drive lubricants, overcoats, and topograpies， *IEEE Transactions on Magnetics*, 41-2, (2005), pp. 626-631.

（5） D. A. Thompson and J. S. Best, The future of magnetic data storage technology, *IBM Journal of Research Development*, 44-3, (2000), pp. 311-322.

（6） E. E. Klaus, and B. Bhushan, Lubricants in Magnetic Media: A Review, *Tribology and Mechanics of Magnetic Storage Systems*, STLE SP-19, 2, (1985), pp. 7-15.

（7） H. Tani, Observation of PFPE lubricant film on magnetic disk surface by atomic force microscopy, *IEEE Transactions on Magnetics*, 35-5, (1999), pp. 2397-2399.

（8） T. Kato, M. Kawaguchi, S. Mayeed, J. Choi, Friction and durability characteristics of ultrathin perfluoropolyether lubricant film composed of bonded and mobile molecular layers on diamond-like carbon surfaces, *Wear*, 207, (2004), pp. 909-915.

(9) Z. Zhao, E. R. Karazic, Q. Zhao, M. J. Emvree, P. H. Trinh, and T. Lam, Lubricant bonding, chemical structure, and additive effects on tribological performances at head-disk interfaces, *Microsystem Technologies*, 2009-1-2, (2002), pp. 48-54.

(10) G. Binnig, C. F. Quate, C. Gerber, Atomic Force Microscope. *Phys.Rev.Lett*, 56, (1986), pp.930-933.

(11) Michael F. Toney and Carol Thompson, Xray reflectivity on perfluoropolyether polymer molecules on amorphous carbon, *J.Chem.Phys*, 92-6, (1990), pp. 3781-3793.

(12) C. Mathew Mate, and V. J. Novotny, Molecular conformation and disjoining pressure of polymeric liquid films, *J. Chem. Phys.* 94-12, (1991), pp. 8420-8427.

(13) A.Benninghoven, Surface analysis by secondary ion mass spectrometry (SIMS), *Surface Science*, 299/300, (1994), pp.246-260.

(14) J. G. Newman, K.V. Viswanathan, Purity and thickness analysis of fluoropolymers by static secondary ion mass spectrometry, *J.Vac.Sci.Technol.A*, 8-3, (1990), pp. 2388-2392.

(15) Lei Zhu, Tom Liew, Mobility of Z-Dol Lubricant Thin Film on Carbon Overcoat Surface, *IEEE Transactions on Magnetics*, 37-4, (2001), pp. 1833-1835.

（16） Y. Abe, M. Shibayama and T. Matsuo, Characterization of lubricant films on magnetic recording disks by ToF-SIMS, *Surface and Interface Analysis*, 30, (2000), pp. 632-634.

（17） Alfred Benninghoven, Chemical Analysis of Inorganic and Organic Surfaces and Thin Films by Static Time-of-Flight Secondary Ion Mass Spectrometry (TOF-SIMS), *Angew. Chem. Inl. Ed. Engl*, 33-10, (1994), pp. 1023-1043.

（18） Catherine Combellas, Frederic Kanoufi, Jean Pinson, and Fetah I. Podvorica, Time-of-Flight Secondary Ion Mass Spectroscopy Characterization of the Covalent Bonding between a Carbon Surface and Aryl Groups, Langmuir, 21-1, (2005), pp. 280-286.

（19） P. R. Griffiths, J. A. de Heseth, Fourier TRasfrom Infrared Spectrometry, 1986.

（20） V. J. Novotny, T. E. Karis, N. W. Johnson, Lubricant removal, degradation, and recovery on particulate magnetic recording media, *ASME Trans. J. Tribolog.*, 114, (1992), pp. 61-67.

（21） S. W. Meeks, W. E. Weresin, H. Rosen, Optical surface analysis of the head disk interface of thin film disks, *ASME J. Tribology*, 117, (1995), pp. 112–118.

（22） Andrei Khurshudov, Robert J. Waltman, Tribology challenges of modern magnetic hard disk drives, *Wear*, 251, (2001), pp. 1124-1132.

（23） R. M. A. Azzam and N. M. Bashara, Ellipsometry and Polarized Light, 1986.

（24） Michael Harke, Martin Stelzle, and Hubert R.Motschmann: Microscopic ellipsometry: imaging monolayer on arbitrary reflecting supports, *Thin Solid Films*, 284-285, (1996), pp. 412-416.

（25） Gang Jin, Roger Jansson, and Hans Arwin, Imaging ellipsometry revisited: Developments for visualization of thin transparent layers on silicon substrates, *Rev. Sci. Instrum.*, 67-8, (1996), pp. 2930-2936.

（26） D. G. Godall, G. W. Stevens, D. Beaglehole, and M. L. Gee: Imaging ellipsometry: Reflectometry for profiling the shape of a deformable droplet as it approaches an interface, *Langmuir, American Chemical Society*, 15-13, (1999), pp. 4579-4583.

（27） F. Linke and R. Merkel, Quantitative ellipsometric microscopy at the silicon–air interface,”*Rev. Sci. Instrum*., 76-6, (2005), pp. 3701-1-3701-10.

（28） K. Fukuzawa, T. Yoshida, S. Itoh, and H. Zhang, Motion Picture Imaging of a Nanometer-thick Liquid Film Dewetting by Ellipsometric Microscopy with a Sub-µm Lateral Resolution, *Langmuir*, 24-20, (2008), pp. 11645-11650.

（29） K. Fukuzawa, T. Shimuta, A. Nakada, H. Zhang, and Y. Mitsuya, Measurement of thickness of molecularly thin lubricant film using ellipsometric microscopy, *IEEE Trans.*

Magn., 41-2, (2005), pp. 808-811.

（30） Max Born and Emil Wolf, Principles of Optics, 1980.

（31） Harland G. Tompkins and Eugene A. Irene, Handbook of Ellipsometry, 2005.

（32） Michael Harke, Martin Stelzle, Hubert R.Motschmann, Microscopic ellipsometry: imaging monolayer on arbitrary reflecting supports, *Thin Solid Films*, 284-285, (1996), pp. 412-416.

（33） D. Beaglehole, Performance of a microscopic imaging ellipsometer, *American Institute of Physics*, (1988), pp. 2557-2559.

（34） Ralph F. Cohn, James W. Wanger, Jerome Kruger, Dynamic imaging microellipsometry: theory, system design, and feasibility demonstration, *Applied Optics*, 27-22, (1998), pp. 4664-4671.

（35） Albert Abraham Michelson, Studies in Optics, 1995.

（36） Depth of field, Wikipekia.

（37） 志牟田太一：修士学位論文「エリプソメトリー顕微鏡によるナノ分子膜の不安定現象の解析に関する研究」，(2006).

（38） K. R. Neumaier, G. Elender, E. Sackmann and R. Merkel, Ellipsometric microscopy, *Europhys. Lett.*, 49-1, (2000), pp. 14-19.

（39） S. Iwasaki, Perpendicular magnetic recording, *IEEE Transactions on Magnetics*, 16, (1980), pp. 71-76.

（40） X. Ma, Spreading of Perfluoropolyalkylether Films on Amorphous Carbon Surfaces, Ph. D. Thesis， *Carnegie Mellon University*, 1998.

（41） K. Fukuzawa, S.Itoh, K. Suzuki, Y. Kawai, H. Zhang, and Y. Mitsuya, Conformation and motion of monolayer lubricant molecule on magnetic disks, *IEEE TRANSACTIONS ON MAGNETICS*， 41-10, (2005), pp. 3034-3036.

（42） 吉田智彦：修士学位論文「ナノ厚さ液体膜可視化のための高分解能エリプソメトリ顕微法に関する研究」, (2008).

（43） John W. Coltman, The specifications of imaging properties by response to a sine wave input, *Journal of the Optical Society of America*, 44, (1954), pp. 468-471.

（44） Horowitz, Paul and Winfield Hill, The Art of Electronics, 2nd edition, *Cambridge University Press*, 1989.